GRAVITATIONAL WAVE ASTEROSEISMOLOGY FROM RAPIDLY ROTATING NEUTRON STARS

A Dissertation
Presented to
The Academic Faculty

By

Athanasios Stavropoulos

In Partial Fulfillment
of the Requirements for the Degree
Doctor of Philosophy in the
School of Physics

Georgia Institute of Technology

May 2018

GRAVITATIONAL WAVE ASTEROSEISMOLOGY FROM RAPIDLY ROTATING NEUTRON STARS

Approved by:

Pablo Laguna, Advisor
School of Physics
Georgia Institute of Technology

Deirdre Shoemaker
School of Physics
Georgia Institute of Technology

Tamara Bogdanovic
School of Physics
Georgia Institute of Technology

John Wise, Committee Chair
School of Physics
Georgia Institute of Technology

Erik I. Verriest
School of Electrical and Computer Engineering
Georgia Institute of Technology

Date Approved: December 20, 2017

To my parents,

for their unconditional love and support.

ACKNOWLEDGEMENTS

I would like to thank my two advisers, Pablo Laguna and Kostantinos Kokkotas for their support and guidance throughout my years as a Ph.D. student. Special thanks and admiration goes to Tanja Bode for her help and patience during my training in the field of computational astrophysics and of course to my colleagues Michael Clark, Matt Kinsey, Andreas Boden and Daniela Doneva for their invaluable help whenever I needed it.

The computations behind the work presented here were performed on the Cygnus Cluster at the Georgia Institute of Technology and the clusters provided by the bwGRiD project.

Special thanks to Ian Hinder and Barry Wardell for the Simulations analysis package. http://simulationtools.org/.

TABLE OF CONTENTS

LIST OF TABLES

LIST OF FIGURES

LIST OF SYMBOLS AND ABREVIATIONS

c	Speed of light.
G	Gravitational constant.
$M_\odot$	Solar mass.
p	Pressure.
ρ	Rest mass density.
u^α	Four velocities.
υ^α	Spatial velocities.
h	Enthalpy.
α	Lapse function.
β^α	Shift vector.
$g_{\mu\nu}$	Space-time metric.
$\eta_{\mu\nu}$	Flat space-time metric.
$\gamma_{\mu\nu}$	Spatial metric.
$\bar{\gamma}_{ij}$	Conformal spatial metric.
$R_{\alpha\beta\gamma\delta}$	Riemann curvature tensor.
${}^{(3)}R_{\alpha\beta\mu\nu}$	Intrinsic Riemann tensor for a spatial hyper-surface.
$K_{\mu\nu}$	Extrinsic curvature.
$T_{\mu\nu}$	Stress energy tensor.
$R_{\mu\nu}$	Ricci tensor.

R	Ricci scalar.
h_+	"Plus" polarization of metric perturbation.
$h_\times$	"Cross" polarization of metric perturbation.
Y_{lm}	Spherical harmonics.
D_{lm}	Mass multipole.
Ω_k	Keplerian angular velocity.
Ψ_4	Fourth Weyl scalar.

SUMMARY

The recent direct observations of gravitational waves from a binary black [1] hole system and separately from a binary neutron star system [22] are among the most exciting events in physics history. This is true not only because it provides another experimental proof for Einstein's general theory of relativity, but also because it opens a new window towards future astronomical observations. More specifically it launches the branch of experimental gravitational wave asteroseismology, the objective of which is studying the physical characteristics of astrophysical systems through studying the gravitational radiation emitted by them. In some cases, like neutron stars, studying the gravitational waves emitted by such systems might be the only way to get an insight to the internal structure of such extreme systems. This thesis outlines a study of rapidly rotating neutron stars as sources of gravitational waves, using a three dimensional general relativistic hydrodynamical code.

CHAPTER 1
INTRODUCTION

During the evolution of a neutron star, there exist many scenarios that can lead to the development of violent oscillations inside it. Such scenarios include supernovae collapses (so the intense period right after the birth of a neutron star), core- and crust-quakes, binary mergers, tidal interactions or mass and angular momentum exchanges between a neutron star and a companion star in a binary system. The main reason why we are interested in studying these oscillations is because through them we can extract information about the stellar characteristics and the interior structure of a neutron star. Since it is impossible to reproduce the extreme conditions of the interior of a neutron star in a laboratory, these kind of studies are among the very few ways to investigate matter in such high densities.

Under certain conditions some modes of oscillation can become unstable. One of the factors that can affect the instability of a mode is the possible fast rotation of a neutron star. Theoretical studies show that rapidly rotating oscillating neutron stars are expected to produce large amounts of gravitational wave radiation. Since the characteristics of this radiation will be unique to the mode of oscillation responsible for its production, detecting and studying gravitational waves will give us information about these modes and consequently about the stellar characteristics of the source.

Using numerical simulations to study the evolution of rapidly rotating neutron stars as sources of gravitational radiation can be very useful in providing theoretical information regarding what we can expect about the stellar characteristics and the equation of state of such sources. More specifically the idea is that since it is not possible to study the evolution of such systems analytically we need to develop appropriate computer codes for this task. Then we need to use such codes to study all the theoretically possible equations of state for a neutron star for all the possible scenarios that could cause such an extreme object to emit

gravitational waves. After collecting and analysing the characteristics of such gravitational signals, we will have in our possession a bank of data that we can compare with the actual experimental data that we expect to get from the existing gravitational detectors. Finally this comparison will give us an idea about the nature of our source.

CHAPTER 2
GENERAL RELATIVITY, GRAVITATIONAL WAVES AND STELLAR OSCILLATIONS

This chapter serves as a brief introduction to general relativity, the concept of gravitational waves and their detectability and finally the field of asteroseismology.

2.1 General relativity

General relativity is a theory which explains that what we understand as gravitational forces within the Newtonian theory of gravity, can be thought as a consequence of the curvature of space-time. So within general relativity the motion of a particle is dictated by the geometrical characteristics of space and time around it. The geometry of space-time it self is directly related to the energy-momentum of the matter-radiation that is present in it. When the problems under study involve only weak gravitational fields, then general relativity reduces to special relativity, which in turn reduces to the Newtonian mechanics when the velocities considered are way lower in magnitude than the speed of light.

Space-time can be mathematically described as a four dimensional manifold, the points of which represent events. Every event is labelled with four coordinates $x^{\mu}(\mu = 0, 1, 2, 3)$, three of which describe its position in space and one its position in time. To describe the geometrical characteristics of such manifold we need to have a relation that can describe the distance between two infinitesimally close neighbouring points x^{μ} and $x^{\mu} + dx^{\mu}$. In the case of general relativity this relation has the following form:

$$ds^2 = g_{\mu\nu}(x^0, x^1, x^2, x^3)dx^{\mu}dx^{\nu}, \tag{2.1}$$

where $g_{\mu\nu}(\bar{x})$ is a symmetric tensor called the metric tensor and in general relativity is the

only thing needed for describing the gravitational field.

The relation between the geometry of space-time and the content of matter-radiation in it, is given by Einsteins gravitational field equations:

$$G_{\mu\nu} = R_{\mu\nu} - \frac{1}{2} g_{\mu\nu} R = \frac{8\pi G}{c^4} T_{\mu\nu}, \tag{2.2}$$

$G_{\mu\nu}$ is the Einstein tensor. $R_{\mu\nu}$ is the Ricci tensor which we get as a contraction of the Riemann tensor, which in turn contains all the information needed about the curvature of space-time, since it is a combination of the metric tensor and of its first and second derivatives. R is the Ricci curvature scalar. G and c are the gravitational constant and the speed of light respectively. Finally $T_{\mu\nu}$ is the stress-energy tensor, a tensorial quantity which describes the mass and energy distribution.

2.2 Gravitational waves

As explained above, the geometrical characteristics of space-time depend on the mass-energy distributions inside it. In case such a distribution variates with time, this will result is the geometry of space-time around it, variating with time too. Unlike Newtonian mechanics though, these variations do not propagate with infinite speed, but with the speed of light. These propagating changes in the geometry of space-time is what we understand as gravitational waves. The most serious sources of such propagating fluctuations are usually accelerating systems of very big mass [20].

If we consider a case where the space-time is described by a metric $g_{\mu\nu} = \eta_{\mu\nu} + h_{\mu\nu}$, so as a combination of the flat space-time metric and some appropriately chosen small perturbation, then there exist conditions such that the Riemann tensor reduces to:

$$R_{j0k0} = -\frac{1}{2} \frac{\partial^2 h_{jk}}{\partial t^2} \quad j, k = 1, 2, 3, \tag{2.3}$$

These conditions are the transverse-traceless (TT) gauge conditions and their result is to

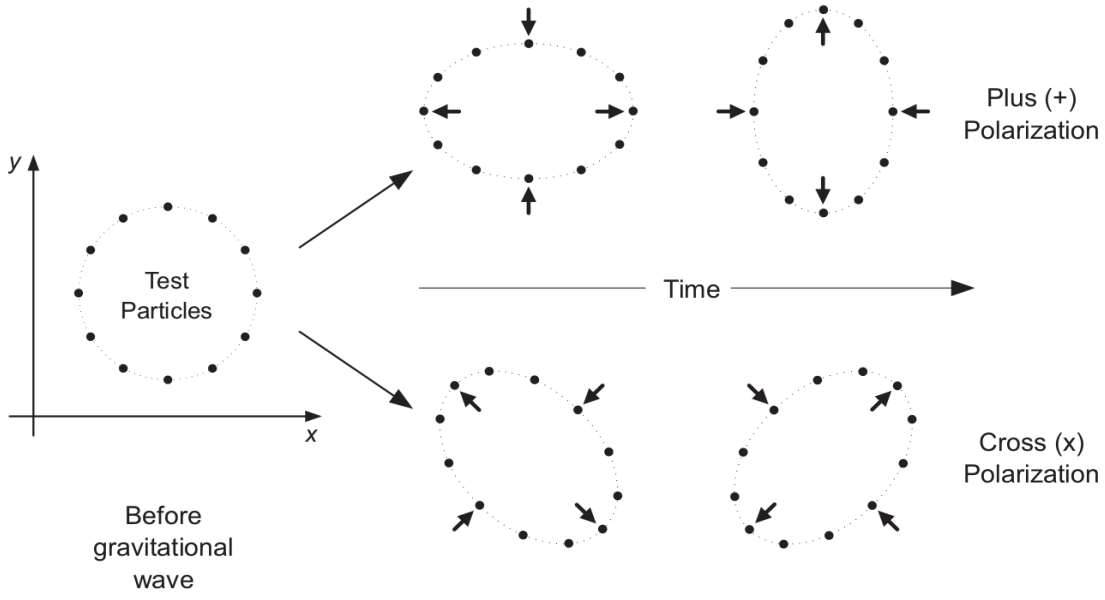

Figure 2.1: Effects of a gravitational wave travelling by a circular ring of test particles. The direction of propagation of the wave is perpendicular to the plane of the ring.

cast Einsteins equation into a wave equation. Another result is to determine eight out the ten independent variables of $h_{\mu\nu}$, leaving two degrees of freedom which correspond to two possible polarizations for the propagating wave. In figure 2.1 we can see the effects of a gravitational wave travelling by a circular ring of test particles.

In case two freely falling test particles with coordinates $x^\mu(\tau)$ and $x^\mu(\tau) + \xi^\mu(\tau)$ find themselves in the way of these propagating fluctuations, then the variation with time of their displacement vector ξ^μ will be given by:

$$\frac{d^2\xi^k}{dt^2} \approx -R^k_{0j0}\xi^j \quad k = 1, 2, 3, \tag{2.4}$$

So these propagating space-time fluctuations can cause motion to particles in space. This is the basic principle behind the gravitational wave detectors that made the first direct observation of gravitational waves. Laser interferometers like LIGO measure the relative distance between two well separated masses. This is done by monitoring a laser beam bouncing continuously back and forth between these two masses. This configuration is one

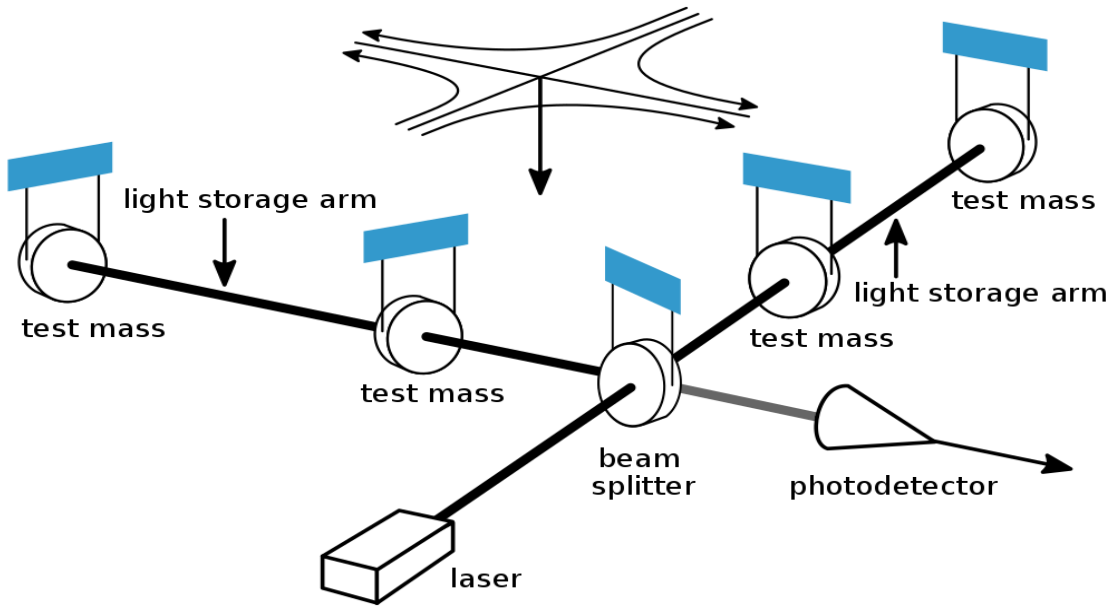

Figure 2.2: Schematic diagram of a laser interferometer.

of the two perpendicular arms that constitute the detector. A schematic diagram of a laser interferometer can be seen in figure 2.2. If a gravitational wave passes by the interferometer in such a way that its plane of propagation is perpendicular to the plane formed by the two arms, then it will increase the length of one of the arms and shorten the length of the other interchangeably and periodically. These changes can be detected with techniques based on Michelson interferometry and in this way we can detect oscillations caused by gravitational waves.

2.3 Relativistic stellar oscillations

As mentioned above the first detection launched the gravitational wave branch of the field of study of asteroseismology. Asteroseismology itself is concerned with the task of gathering astronomical observations, photometric and spectroscopic, to extract frequencies, amplitudes and phases from pulsating stars. Later using these information and basic laws of physics we can reach various conclusions regarding the density, temperature and pressure inside a star and thus its equation of state. So such information can be used to directly

model and probe the stellar interior. Since the frequencies and amplitudes observed from a star are characteristic of the modes of oscillation that produced them, it is useful to have an idea about the types of modes that can be present within a star [7].

Since stars are three-dimensional objects, we can describe their natural oscillation modes using an (r, θ, ϕ) spherical coordinate system. Where r is the distance from the center, θ is the co-latitude measured form the axis of symmetry and ϕ is the longitude. In this case, nodes of oscillation represent shells at constant r, cones of constant θ and planes of constant ϕ. For the case of a non-rotating spherically symmetric stellar object, the solutions to the equations of motion have displacements described in the following way:

$$\xi_r(r, \theta, \phi, t) = a(r) Y_{lm}(\theta, \phi) e^{-i2\pi\nu t}, \tag{2.5}$$

$$\xi_\theta(r, \theta, \phi, t) = b(r) \frac{\partial Y_{lm}(\theta, \phi)}{\partial \theta} e^{-i2\pi\nu t}, \tag{2.6}$$

$$\xi_\phi(r, \theta, \phi, t) = \frac{b(r)}{\sin\theta} \frac{\partial Y_{lm}(\theta, \phi)}{\partial \phi} e^{-i2\pi\nu t}, \tag{2.7}$$

where ξ_r ,ξ_θ and ξ_ϕ represent the displacements, $a(r)$ and $b(r)$ represent amplitudes, ν refers to the oscillation frequency and $Y_{lm}(\theta, \phi)$ are the spherical harmonic functions. Thus to specify a mode of oscillation in a three-dimensional stellar configuration we need three quantum numbers: n which refers to the number of radial nodes, l which refers to the number of surface nodes and m which refers to the number of surface nodes that are lines of longitude.

The simplest approximation for a neutron star would be a model described by a polytropic equation of state with no magnetic field and no rotation. In the classical - non relativistic regime, there exist various types of modes of oscillations which we classify according to the type of the restoring forces that are responsible for them.

1. Pressure modes (p-modes): This is a family of modes for which the primary restoring force is pressure and they basically describe acoustic waves inside the star. For each l these modes have an abundance of overtones. The lower $l = 2$ p-mode has typically a frequency around 4-7 kHz, depending on the equation of state, while their damping times is of the order of a few seconds. Increasing the overtone number increases both the frequency and the dumping time of the mode. The p-modes are sensitive to conditions in the outer part of the star. They are characterized by relatively small amplitudes in regions close to the center of the star and larger amplitudes towards its outer parts.

2. Gravity modes (g-modes): This is a family of modes for which the restoring force is gravity. In this case when a fluid element is pushed out of its equilibrium position, then thermally induced buoyancy works as a restoring force to place it back. These modes are more sensitive to conditions deep in the interior of the star resulting to the amplitude of these modes being larger towards the central part and relatively smaller towards the outer parts. The frequency characterizing g-modes depends on the thermal structure of the star and it increases approximately linearly with the central temperature. In general they have lower frequencies than the p- and f-modes and due to the fact that the density fluctuations that they induce is very small, the damping times due to gravitational wave emission are very long, of the orders of years. The g-modes are also characterized by an abundance of overtones with the frequency decreasing as the overtone increases.

3. Fundamental modes (f-modes): For every $l \geq 2$ there exists a single mode called the fundamental mode with an intermediate character between the g- and the p-modes. Its frequency depends on the equation of state and is typically in the range of 1-3 kHz while its damping time is typically around a few tenths of a second. This mode is a result of the existence of an interface between the star and the surrounding space

and for each l it has no node inside the star. It describes purely non radial oscillations which can emit gravitational radiation efficiently and its amplitude increases as we move towards the outer parts of the star.

When we move to the realm of extreme stellar objects like neutron stars, Newtonian mechanics stops being adequate enough to describe the observed physics and needs to be replaced by General Relativity. Since such stellar configurations can serve as sources of gravitational radiation, we now have to deal with another dissipation mechanism that can remove energy out of the modes within the star. The study of the fluctuations of space-time in the vicinity of extreme stellar objects has revealed the existence of another family of modes.

4. Space-time modes (w-modes): These modes refer to the perturbation of space-time variables in the region outside the star and they do not induce significant fluid motion. Their frequencies depend on the equation of state with typical values in between 6-14 kHz and typical damping times of the order of tens of microseconds.

If we take in account also the possible rotation of a star, then we need to include in our picture the consequences of the centrifugal and the Coriolis force. The centrifugal force results in distorting the shape of a star from spherical to oblate ellipsoidal, symmetric around the axis of rotation. Apart from this distortion though, the existence of the centrifugal force will not result in the appearance of new modes of oscillations. On the other hand the existence of the Coriolis force will result in another class of modes.

5. Rotational modes (r-modes): This is a family of modes for which the restoring force is the Coriolis inertial force and they behave like the Rossby waves do on the Earths ocean. The frequency of these is degenerate for a non rotating star and proportional to its angular frequency in the rotating case.

Finally the spectrum of fluid modes becomes richer when we consider more realistic models of neutron stars modelled as having a liquid core with a solid crust. In general the

f- and p-modes are not significantly affected by the existence of a crust while the g-modes do get affected because the crust can not sustain much thermally induced buoyancy. In addition the existence of a crust results in the appearance of the so called shear s-modes and interfacial i-modes. The s-modes refer to the appearance of shear waves propagating in the solid crust and their frequency depends on the crust thickness while the i-modes refer to the existence of waves propagating on the solid-fluid interface and their frequency depends strongly on the density and temperature of that region.

2.4 The Cowling approximation

The full non linear equations of general relativity are very difficult to deal with for the vast majority of the problems that involve rotating neutron stars. Because of this, most of the existing research around neutron star oscillations has been conducted within certain approximations. One extensively used approximation is the so called Cowling approximation, where the perturbations of the gravitational potential caused by the pressure and density fluctuations within the star are neglected. Within general relativity this translates in neglecting the coupling between the matter perturbations and the space-time. The logic behind this approach is that the fluctuations of the gravitational potential due to density variations, should be small in the outer regions of a star if its mass is mainly concentrated towards the center. In practice this approach is suitable for the qualitative, and is some cases also quantitative, study of fluid modes but clearly not the space-time w-modes.

2.5 The CFS instability

As mentioned above, rotation and the resulting Coriolis force, can induce instabilities in a star. One of these instabilities is the so called Chandrasekhar-Friedman-Schutz (CFS) instability, which is a generic feature of rotating stars [3,4]. The reason why we are particularly interested in this mechanism is the fact that there exists a counter rotating branch which extends to frequencies that could be observed by the gravitational wave interfero-

metric detectors existing today. Lets consider a mode that has the following form as seen by a frame co-rotating with the star:

$$\delta f(t, r, \theta, \phi_c) = A(r, \theta) \cdot e^{im\phi_c} \cdot e^{i\omega_c t} \tag{2.8}$$

where ϕ_c and ω_c are the polar angle and angular velocity in this frame. Lines of constant phase obey $m\phi_c + m\omega_c t = const.$ so $\phi_c = \phi_c(0) - (1/m)\omega_c t$. This shows that in the case of a non rotating star, the frequency of a mode described by (2.8) appears to be degenerate. As the star starts to rotate though, we observe this degeneracy breaking down. Modes characterized by $m > 0$ are counter-rotating with respect to the co-rotating observer, while modes with $m < 0$ follow the co-rotating observer. For an inertial observer at infinity that uses polar coordinates $(r, \theta, \phi_i) = (r, \theta, \phi_c + \Omega t)$, with ϕ_i and Ω being the polar angle and the angular velocity of our star for that observer, the same mode has the form:

$$\delta f(t, r, \theta, \phi_i) = A(r, \theta) \cdot e^{im(\phi_i - \Omega t)} \cdot e^{i\omega_c t} = A(r, \theta) \cdot e^{im\phi_i} \cdot e^{i(\omega_c - m\Omega)t} \tag{2.9}$$

So the angular velocity ω_i measured by the inertial observer at infinity is given by

$$\omega_i = \omega_c - m\Omega \tag{2.10}$$

This means that for every counter-rotating mode there exists some value for the angular velocity Ω for which ω_i becomes equal to zero. For angular velocities bigger than this value, the mode that is counter-rotating in the co-rotating frame, appears to be co-rotating with the star for the observer at infinity. Lets consider now a star rotating around the z-axis that emits gravitational waves which carry away angular momentum J_z. Depending on whether J_z is positive or negative for an observer at infinity, the emitted radiation will carry away positive or negative angular momentum respectively, resulting in decreasing $|J_z|$. For a mode of oscillation that counter-rotates with respect to an observer following the

rotation of the star but is co-rotating with the star, with respect to an observer at infinity, the gravitational waves carry away positive angular momentum. This results in the star slowing down and thus for the mode to appear rotating even faster for the co-rotating observer. This consequently will result in bigger amounts of gravitational radiation being emitted. This is the procedure that is known as the CFS instability.

From equation (2.10) we can see that increasing Ω will, at some point, result in the appearance of the CFS instability, which will result in the emission of big amounts of detectable gravitational radiation. In reality though there exist some limitations. First of all, as we will see below, a star can not rotate faster than the mass shedding limit. Another limitation arises from the fact that the instability can set in only if its growth time is shorter than the dumping time due to viscosity mechanisms.

If we model the star as a self gravitating Newtonian fluid then we can specify its state if we know its mass density ρ, pressure p and the spatial velocities υ^{α} at every point inside the star. If we include affects of viscosity and gravitational radiation then the evolution of these quantities can be described by

$$\partial_t \rho + \nabla_a(\rho \upsilon^a) = 0 \tag{2.11}$$

$$\partial_t \upsilon^a + \upsilon^b \nabla_b \upsilon^a + \nabla^a U = \nabla^a \Phi_{GR} + 2\rho^{-1}\nabla_b(\eta\sigma^{ab}) + \rho^{-1}\nabla^a(\zeta\sigma) \tag{2.12}$$

Where ∂_t is the partial derivative with respect to time and ∇_a is the spatial Cartesian covariant derivative. In equation (2.12) the potential U is defined by

$$U = h(p) - \Phi = \int_0^p \frac{dp'}{\rho(p')} - \Phi \tag{2.13}$$

with Φ being the Newtonian gravitational potential satisfying

$$\nabla^a \nabla_a \Phi = -4\pi G\rho \tag{2.14}$$

The potential Φ_{GR} refers to the coupling of the fluid to the gravitational-radiation reaction defined by

$$\Phi_{GR} = -\sum_{l=2}^{\infty}\sum_{m=-l}^{l}(-1)^l N_l r^l Y_l^m \frac{d^{2l+1}D_l^m}{dt^{2l+1}} \tag{2.15}$$

where D_l^m is the mass multipole defined as

$$D_l^m = \int \rho r^l Y_l^{*m} d^3x \tag{2.16}$$

and N_l is a constant defined as

$$N_l = \frac{4\pi G}{c^{2l+1}} \frac{(l+1)(l+2)}{l(l-1)[(2l+1)!!]^2} \tag{2.17}$$

with c being the speed of light and G the gravitational constant. Finally, η and ζ are the shear-viscosity and bulk-viscosity coefficients which are considered to be given functions of ρ while σ^{ab} and σ are the shear and the expansion define as

$$\sigma^{ab} = \frac{1}{2}(\nabla^a \upsilon^b + \nabla^b \upsilon^a - \frac{2}{3} g^{ab} \nabla_c \upsilon^c) \tag{2.18}$$

and

$$\sigma = \nabla_a \upsilon^a \tag{2.19}$$

If we consider the evolution equations for small perturbations around an equilibrium solution and denote the Eulerian perturbation (perturbation as seen by an inertial observer at infinity) of some quantity q as δq then linearising equations (2.11) to (2.14) results in

$$\partial_t \delta\rho + \upsilon^a \nabla_a \delta\rho + \nabla_a(\rho \delta\upsilon^a) = 0 \tag{2.20}$$

$$\partial_t \delta\upsilon^a + \upsilon^b \nabla_b \delta\upsilon^a + \delta\upsilon^b \nabla_b \upsilon^a + \nabla^a \delta U = \nabla^a \delta\Phi_{GR} + 2\rho^{-1}\nabla_b(\eta\delta\sigma^{ab}) + \rho^{-1}\nabla^a(\zeta\delta\sigma) \tag{2.21}$$

$$\nabla^a \nabla_a \delta\Phi = -4\pi G \delta\rho \tag{2.22}$$

We define the energy of the perturbations in the co-moving as

$$E(t) = \frac{1}{2}\int \Big[\rho \delta\upsilon^a \delta\upsilon_a^* + \frac{1}{2}(\delta\rho\delta U^* + \delta\rho^*\delta U)\Big] d^3x \tag{2.23}$$

where

$$\delta U = \frac{\delta p}{\rho} - \delta\Phi \tag{2.24}$$

Now using the linearised equations (2.20), (2.21) and (2.22) we can calculate the time derivative of the perturbations energy as

$$\begin{gathered}\frac{dE(t)}{dt} = -\int (2\eta\delta\sigma^{ab}\delta\sigma_{ab}^* + \zeta\delta\sigma\delta\sigma^*) d^3x - \frac{1}{2}\sum_{l=2}^{\infty}\sum_{m=-l}^{l}(-1)^l N_l \cdot \\ \left[\frac{d^{2l+1}\delta D_l^m}{dt^{2l+1}}\left(\frac{d\delta D_l^{*m}}{dt} - im\Omega\delta D_l^{*m}\right) + \frac{d^{2l+1}D_l^{*m}}{dt^{2l+1}}\left(\frac{d\delta D_l^m}{dt} + im\Omega\delta D_l^m\right)\right]\end{gathered} \tag{2.25}$$

where

$$\delta\sigma^{ab} = \frac{1}{2}(\nabla^a\delta\upsilon^b + \nabla^b\delta\upsilon^a - \frac{2}{3}g^{ab}\nabla_c\delta\upsilon^c) \tag{2.26}$$

$$\delta\sigma = \nabla_a\delta\upsilon^a \tag{2.27}$$

and

$$\delta D_l^m = \int \delta\rho r^l Y_l^{*m} d^3x \tag{2.28}$$

Furthermore, if we also assume that all the perturbed quantities have a sinusoidal dependence of the form: $\delta q = \delta q(r,\theta)e^{im\phi + i\omega t}$, with ω being the frequency of the mode under study, then we can relate the derivative of the imaginary part of the frequency by:

$$\frac{dE}{dt} = -2E \cdot Im(\omega) = -\frac{2E}{\tau} \tag{2.29}$$

Regarding the contributions of each of the dissipative mechanisms to the imaginary part of the frequency we get:

$$\frac{1}{\tau_\zeta} = \frac{1}{2E}\int \zeta \delta\sigma \delta\sigma^* d^3x \tag{2.30}$$

$$\frac{1}{\tau_\eta} = \frac{1}{E}\int \eta \delta\sigma^{ab} \delta\sigma^*_{ab} d^3x \tag{2.31}$$

and

$$\frac{1}{\tau_{GR}} = \frac{\omega + m\Omega}{2E}\sum_{l=l_{min}}^{\infty} N_l \omega^{2l+1} \delta D_l^m D_l^{*m} \tag{2.32}$$

Finally the imaginary part of the frequency is given by:

$$\frac{1}{\tau} = \frac{1}{\tau_{GR}} + \frac{1}{\tau_\zeta} + \frac{1}{\tau_\eta} \tag{2.33}$$

For the CFS instability to be activated it must be that $|\tau_{GR}|$ is small enough that $\frac{1}{\tau_{GR}} + \frac{1}{\tau_\zeta} + \frac{1}{\tau_\eta} < 0$ which means that $|\tau_{GR}|$ must be smaller than the time scale over which viscosity dumps out the perturbation.

The bulk viscosity ζ is a consequence of the phase lag that occurs between the pressure and density fluctuations in the neutron star matter. This phase lag exists due to the relatively long time scale required for weak interactions to re-establish equilibrium. The shear viscosity η is the result of momentum transport within the fluid due to the scattering of particles. These coefficients depend strongly on the temperature of the star and there exists a window of temperatures where the viscosity is low and the CFS instability can be activated.

In general as the neutron star cools down its rotation slows down too, so an important question is if the star can pass through the temperature instability window when it is still young and rapidly rotating. For the case of the f-modes the rotational frequency needs to be an important fraction of the Keplerian frequency, while the situation is better for r-modes.

2.6 Gravitational wave asteroseismology

As mentioned above there exist numerous scenarios that could lead to the activation of violent non radial oscillations inside compact objects and the subsequent emission of gravitational radiation. The detection of gravitational waves from neutron stars will allow the study of their interior in a similar way helioseismology provides information about the interior of the sun.

The goal of the numerical branch of gravitational wave asteroseismology is to computationally study the frequencies and damping/growth times of the various modes of oscillation that could be present inside a neutron star, for all the theoretically possible equations of state of such compact objects. After collecting such data one can construct empirical formulas relating the characteristics of the modes to the fundamental quantities of the neutron star models under study, like their masses and radii. The final objective is when actual observations from neutron stars become available to have robust relations that will provide us with information about the structure of the sources detected.

Lets consider for example the study of the f-mode of oscillation for some specific equilibrium neutron star model, starting from the non rotating case and reaching up to a rapidly rotating case close to the mass shedding limit. In the non rotating case the f-modes are characterized by specific values of (l, m) corresponding to the spherical harmonics with same indices and are degenerate in m. In the presence of rotation though it is not possible to separate the perturbation equation into an angular and a radial part. Analogous to the Zeeman splitting in quantum mechanics, the existence of a preferred direction in space, in this case the rotation axis of the compact object, leads to the breaking of the degeneracy in m. This results in the appearance of co-rotating and counter-rotating, with respect to the rotation of the star, modes of oscillation. This modes are characterized by the value l of the mode to which they reduce in the non rotating case. As described in [5,6], while in the inertial frame the f-mode splitting depends on the neutron star model under study,

when properly normalised in a frame co-rotating with the star one can actually create model independent relation between the frequency of the mode and the rotation rate of the star. For the $l = |m| = 2$ mode studied under the Cowling approximation, depending on their numerical data, [5] proposes the following relations:

$$\frac{\omega_c^s}{\omega_0} = 1.0 - 0.27(\frac{\Omega}{\Omega_K}) - 0.34(\frac{\Omega}{\Omega_K})^2 \quad for \quad m = -2 \tag{2.34}$$

And

$$\frac{\omega_c^u}{\omega_0} = 1.0 + 0.47(\frac{\Omega}{\Omega_K}) - 0.51(\frac{\Omega}{\Omega_K})^2 \quad for \quad m = 2 \tag{2.35}$$

where ω_c^s and ω_c^u the frequencies of the f-modes in the stable and the unstable branches correspondingly. Also, taking in account the fact that for the f-mode ω_0 scales with $(M/R^3)^{1/2}$, we get the relation:

$$\frac{1}{2\pi}\omega_0 = 0.498 + 2.418(\frac{\bar{M}}{\bar{R}^3})^{1/2} \quad kHz \tag{2.36}$$

where $\bar{M} = M/1.4M_\odot$ and $\bar{R} = R/10km$. Following the same logic when it comes to the study of the corresponding damping times, in [5] they get the following formulas:

$$\frac{\tau_0}{\tau} = sgn(\omega_i^u)0.256(\frac{\omega_i^u}{\omega_0})^4\Big[1 + 0.048(\frac{\omega_i^u}{\omega_0}) + 0.359((\frac{\omega_i^u}{\omega_0}))^2\Big]^4 \quad for \quad m = 2 \tag{2.37}$$

And

$$\frac{\tau}{\tau_0} = -0.656\Big[1 - 7.33(\frac{\omega_s^c}{\omega_0}) + 14.07(\frac{\omega_s^c}{\omega_0})^2 - 9.26(\frac{\omega_s^c}{\omega_0})^3\Big] \quad for \quad m = -2 \tag{2.38}$$

where ω_i^s the frequencies of the f-modes with respect to the an inertial frame. Connecting again the numerical data to fundamental model characteristics they got:

$$\frac{1}{\tau_0(s)} = \frac{\bar{M}^3}{\bar{R}^4}[22.49 - 14.03(\frac{\bar{M}}{\bar{R}})] \quad kHz \tag{2.39}$$

Equations (2.36) and (2.39) refer to the behaviour of neutron stars in the non rotating limit.

After one acquires such relations it is possible to do gravitational wave asteroseismology. More specifically given three independent measurements, two frequencies and one damping time, from the same source, one can make a robust calculation of the radius, the mass and the angular frequency of the source and therefore single out these equations of state that agree with these measurements.

Equivalent relations for the space-time w-modes of oscillation in the non rotating limit for $l = 2$ and overtone number $n = 1$ give:

$$f({}^2w_1) \simeq \frac{1}{\bar{R}}\Big[20.92 - 9.14(\frac{\bar{M}}{\bar{R}})\Big] \quad kHz \tag{2.40}$$

$$\tau({}^2w_1) \simeq \bar{M}\Big[5.742 + 103(\frac{\bar{M}}{\bar{R}}) - 67.45(\frac{\bar{M}}{\bar{R}})^2\Big]^{-1} \quad ms \tag{2.41}$$

Worthy of mentioning is that in general observing a lot of independent and clear values for frequencies and damping times of stable oscillations is a rather optimistic scenario. A more realistic case would be to get fewer data than required for the calculation of (M, R, Ω) of a source. In that case we will have to reside to combinations of these values. For example given the f-mode frequencies of the co- and counter-rotating branch we can get the values for M/R^3 and Ω/Ω_K

CHAPTER 3
NUMERICAL RELATIVITY:USING COMPUTERS TO SOLVE EINSTEIN'S EQUATIONS

Besides relatively simple cases, solving the Einstein equations analytically is a very difficult, or in most of the cases, an impossible task. That is where the use of computers and the field of numerical relativity come in. The goal is to solve the system of equations (2.2). The problem though is that this form of Einstein's equations is not suitable for numerical treatment. Instead of trying to describe the whole space time geometry at once it would be more preferable to study our system as a time succession of consecutive space geometries.

3.1 The 3+1 decomposition of space-time

Einstein's field equation is a system of ten second order partial differential equations of the space-time metric $g_{\alpha\beta}$. The task in hand is to reformulate our system in such a way that given the metric $g_{\alpha\beta}$ and its time derivative $\partial_t g_{\alpha\beta}$ for some initial moment t_0 at some initial space-like 3-dimensional hypersurface Σ_{t_0}, to be possible to calculate the same quantities at a succeeding space-like 3-dimensional hypersurface Σ_{t_1} where $t_1 = t_0 + dt$. Repeating this procedure will eventually allow us to describe the whole space-time.

Since we need to evolve $g_{\alpha\beta}$ and $\partial_t g_{\alpha\beta}$ in time, we need to obtain expressions involving $\partial_t^2 g_{\mu\nu}$. The first logical choice would be to use Einstein's field equations which seem to provide exactly ten such expressions. The problem with this approach though is that we have to take in account Bianchi's identities which state that $\nabla_\beta G^{\alpha\beta} = 0$. This leads to:

$$\partial_0 G^{\alpha 0} = -\partial i G^{\alpha i} - G^{bc}\Gamma^{\alpha}_{bc} - G^{\alpha b}\Gamma^{c}_{bc} \tag{3.1}$$

Since there is no term in the right hand side that contains any third time derivatives, it means that $G^{\alpha 0}$ does not contain any second time derivatives of $g_{\alpha\beta}$, which leads to the conclusion that the equations $G^{\alpha 0} = 8\pi T^{\alpha 0}$ do not contain any information about the dynamic evolution of the system. These expressions are called constraint equations and hold analytically true for all space-time. They supply four constraints for the initial data and in numerical relativity one can use them as a test for the validity of the computational evolution.

This analysis shows that the only dynamical evolution equations are provided by the remaining six relations

$$G^{ij} = 8\pi T^{ij} \tag{3.2}$$

The reason for the four remaining degrees of freedom stems out of the fact that we need to fix a four-coordinate system in space-time. After a coordinate system gets in place, then we have six equations containing $\partial_t^2 g_{ij}$ to evolve g_{ij} and four constraints to relate g_{ij} and $\partial_t g_{ij}$ to the initial hypersurface Σ_{t_0}. So in principle anything needed to evolve our system.

Going back to the desired decomposition, we assume that the space-time $(M, g_{\alpha\beta})$ can be separated into a family of non intersecting 3-dimensional space-like hypersurfaces Σ_t with t being a scalar function which can be interpreted as a global time function. Since every Σ_t is space-like then the gradient $\nabla^\mu t$, which is normal to Σ_t by construction, must be time-like. We have

$$g^{\alpha\beta}\nabla_\alpha t \nabla_\beta t \equiv -\frac{1}{\alpha^2} \tag{3.3}$$

Where α is known as the lapse function and measures how much proper time elapses between two consequent time slices. This allows us to define a unit normal vector field n^μ as

$$n^\mu = -\alpha \nabla^\mu t \tag{3.4}$$

Where $n^\mu n_\mu = -1$. So finally for every space-like hypersurface Σ_t we can construct a

purely spatial metric as

$$\gamma_{\alpha\beta} = g_{\alpha\beta} + n_\alpha n_\beta \tag{3.5}$$

This metric exists entirely within the corresponding space-like hypersurface and provides us with the means to decompose arbitrary vector and tensor quantities into their time-like projection and their space-like projection into Σ_t. It can also be used to calculate distances and raise and lower vectors and tensors existing in Σ_t, so it can give us information about the geometry intrinsic to the corresponding hypersurface.

While the intrinsic geometry of our hypersurfaces can be described by (3.5), their orientation inside the four-dimensional space-time is described by what we define as the extrinsic curvature $K_{\alpha\beta}$. This quantity can be defined as:

$$K_{\alpha\beta} = -\gamma_a^c \gamma_\beta^d \nabla_c n_d \tag{3.6}$$

So by definition the extrinsic curvature is purely spatial and symmetric and measures the gradient of the normal vectors n_a. This means that it provides information about how much the direction of the normal vector changes from point to point while moving inside the spatial hypersurface. In addition the extrinsic curvature is connected to the spatial metric by:

$$K_{\alpha\beta} = -\frac{1}{2}\mathcal{L}_n \gamma_{\alpha\beta} \tag{3.7}$$

Where $\mathcal{L}_n$ is the Lie derivative along n_a. As mentioned in [21] the spatial metric and the extrinsic curvature can be considered as the equivalent of positions and velocities in classical mechanics in the sense that they measure the state of the gravitational field and are two of the quantities that we wish to evolve in time.

The most general case of a time vector is defined by:

$$t^a = \alpha n^a + \beta^a \tag{3.8}$$

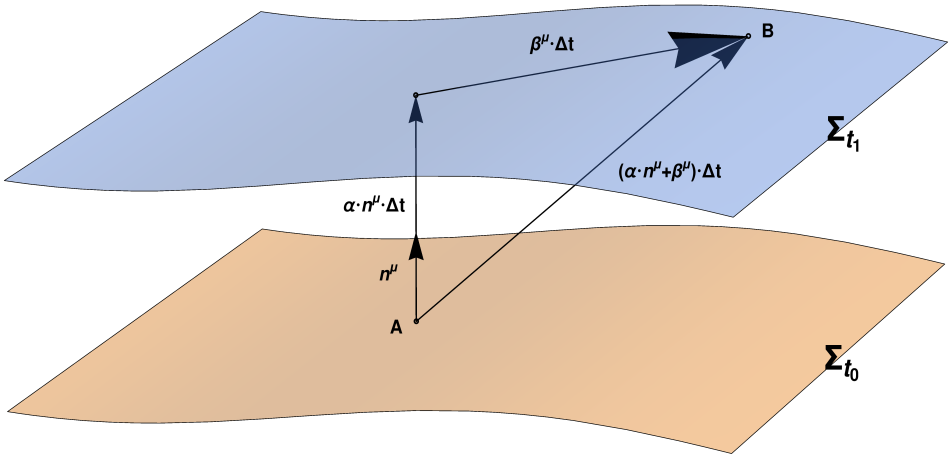

Figure 3.1: Standard 3+1 decomposition of space time. Hypersurfaces Σ_{t_0} and Σ_{t_1} correspond to two infinitesimally close coordinate times t_0, t_1 respectively. Points A and B are characterized by the same spatial coordinates and are connected by the vector t^α expressed in terms of the lapse α, the normal vector n^α and the shift vector β^α.

This quantity satisfies $t^\alpha \nabla_\alpha t = 1$ for any spatial vector β^α. This means that vector (3.8) connects points with the same spatial coordinates in the two infinitesimally close hypersurfaces Σ_{t_0} and Σ_{t_1}. The vector β^α is known as the shift vector and indicates how much the spatial coordinates have shifted in the spatial slide with respect to the normal vector n^α. The lapse and the shift together provide the four dynamical coordinate degrees of freedom needed to specify the evolution of the coordinates of our system in time. The choice of these quantities is very important for the numerical evolution of a general relativistic system and the specific selection chosen is known as the gauge conditions.

The next step in this procedure is to find the relations between the extrinsic curvature $K_{\alpha\beta}$ the four-dimensional Riemann curvature tensor $R_{\alpha\beta\mu\nu}$ and the intrinsic Riemann tensor for a spatial hyper-surface ${}^{(3)}R_{\alpha\beta\mu\nu}$. The complete spatial projection of the Riemann tensor gives us Gauss's equation:

$$\gamma^\delta_\alpha \gamma^\epsilon_\beta \gamma^\zeta_\mu \gamma^\theta_\nu R_{\delta\epsilon\zeta\theta} =^{(3)} R_{\alpha\beta\mu\nu} + K_{\alpha\mu}K_{\beta\nu} - K_{\alpha\nu}K_{\beta\mu} \tag{3.9}$$

Projecting one index in the normal direction gives us Godazzi's equation:

$$\gamma_\alpha^\delta \gamma_\beta^\epsilon \gamma_\mu^\zeta n^\nu R_{\delta\epsilon\zeta\nu} = D_\beta K_{\alpha\mu} - D_\alpha K_{\beta\mu} \tag{3.10}$$

Neither of these two equations involve any time derivatives, which means that they represent constraints that should be obeyed on every hyper-surface. Finally projecting two components gives us Ricci's equation:

$$\gamma_\alpha^\delta \gamma_\beta^\epsilon n^\mu n^\nu R_{\mu\epsilon\nu\delta} = \mathcal{L}_n K_{\alpha\beta} + \frac{1}{\alpha} D_\alpha D_\beta \alpha + K_{\alpha\mu} K_\beta^\mu \tag{3.11}$$

Given the appearance of the Lie derivative in Ricci's equation, we expect that it will serve as the basis out of which the evolution equations will emerge.

Equations (3.9), (3.10), and (3.11) give us a decomposition of the four-dimensional Riemann tensor and express the evolution and constraint equations wholly in terms of the geometry of space-time. The next step would be to use Einstein's equations to couple the above equations with the stress-energy tensor. In other words we need to relate the intrinsic Riemann tensor components to the components of $T^{\alpha\beta}$. Within this context it is useful to define the energy density as:

$$\tau = n_\alpha n_\beta T^{\alpha\beta} \tag{3.12}$$

The momentum density as:

$$S_\alpha = -\gamma_\alpha^\mu n^\nu T_{\mu\nu} \tag{3.13}$$

And finally the stress tensor:

$$S_{\alpha\beta} = \gamma_\alpha^\mu \gamma_\beta^\nu T_{\mu\nu} \tag{3.14}$$

and its trace:

$$S = S_\alpha^\alpha \tag{3.15}$$

Contracting the constraint equations with the purpose of writing them in terms of the Ricci

tensor and taking in account the skew symmetry of the Riemann tensor, Gauss's equation leads us to:

$$R + K^2 - K_{\mu\nu}K^{\mu\nu} = 16\pi n^\mu n^\nu T_{\mu\nu} = 16\pi\tau \tag{3.16}$$

While Godazzi's equation leads to:

$$D_\mu K^\mu_\alpha - D_\mu K - 8\pi S_\mu = 0 \tag{3.17}$$

Where $K = K^\mu_\mu = g_{\mu\nu}K^{\mu\nu}$. Equations (3.16) and (3.17) are respectively the Hamiltonian constraint and the momentum constraints.

Turning our attention to the evolution of the spatial metric $\gamma_{\mu\nu}$, we can combine equation (3.7) which states that the extrinsic curvature can be found as the Lie derivative of the spatial metric along n^μ with equation (3.11) to get:

$$\mathcal{L}_t\gamma_{\mu\nu} = -2\alpha K_{\mu\nu} + \mathcal{L}_\beta\gamma_{\mu\nu} \tag{3.18}$$

Similarly the evolution equation for the extrinsic curvature is given by:

$$\mathcal{L}_t K_{\mu\nu} = -D_\mu D_\nu\alpha + \alpha(R_{\mu\nu} + KK_{\mu\nu} - 2K_{\mu\rho}K^\rho_\nu - 8\pi S_{\mu\nu} + 4\pi\gamma_{\mu\nu}(S-\tau)) + \mathcal{L}_\beta K_{\mu\nu} \tag{3.19}$$

Equations (3.16), (3.17), (3.18) and (3.19) form what is known as the modern Anowitt-Deser-Misner (ADM) system of equations. This set of equations is analytically equivalent to the Einstein field equations and provide the wanted 3 + 1 decomposition. Unfortunately, although this approach has all the desired properties, it has been proven to be a weak basis for the numerical evolution of Einstein's equations.

3.2 Hyperbolicity of PDEs

A system of second order partial differential equations can be classified depending on its form. We consider the following PDE:

$$A\frac{\partial^2\Psi}{\partial x^2} + 2B\frac{\partial^2\Psi}{\partial x\partial y} + C\frac{\partial^2\Psi}{\partial y^2} = D(x, y, \Psi, \frac{\partial\Psi}{\partial x}, \frac{\partial\Psi}{\partial y}) \tag{3.20}$$

where A,B and C are constants while is D some arbitrary function. Depending on the relation in between the constants A, B and C a PDE can be classified as either elliptic, parabolic or hyperbolic. More specifically we have:

1. If $B^2-4AC < 0$ the equation is considered to be elliptic and there exists a coordinate transformation that turns (3.20) to:

$$\frac{\partial^2\Psi}{\partial x^2} + \frac{\partial^2\Psi}{\partial y^2} = D \tag{3.21}$$

   Poison's and Laplace's equations are examples of elliptic PDEs

2. If $B^2 - 4AC = 0$ the equation is considered to be parabolic and there exists a coordinate transformation that turns (3.20) to:

$$\frac{\partial\Psi}{\partial t} - \kappa\frac{\partial^2\Psi}{\partial x^2} = D \tag{3.22}$$

   The diffusion equation with κ being the diffusion constant is an example of a parabolic PDE.

3. If $B^2 - 4AC > 0$ the equation is considered to be hyperbolic and there exists a coordinate transformation that turns (3.20) to:

$$\frac{\partial^2\Psi}{\partial t^2} - c^2\frac{\partial^2\Psi}{\partial x^2} = D \tag{3.23}$$

The wave equation with propagation speed equal to c is an example of a hyperbolic PDE.

Depending on the type of PDE at hand there are different methods that need to be employed for their solution. Due to the fact that we are mostly interested in the study of causal propagation phenomena like the modes of oscillation present in neutron stars and the gravitational waves emitted by them, we concentrate on the hyperbolic type of PDEs. Recasting equation (3.23) into a system of first order partial differential equations we get:

$$\begin{aligned} \frac{\partial \psi}{\partial t} &= -u \\ \frac{\partial u}{\partial t} + c^2 \frac{\partial w}{\partial x} &= -D \\ \frac{\partial w}{\partial t} + \frac{\partial u}{\partial x} &= 0 \end{aligned} \tag{3.24}$$

Or equivalently in a more concise form:

$$\frac{\partial \mathbf{\Psi}}{\partial t} + \mathbf{A} \frac{\partial \mathbf{\Psi}}{\partial x} = \mathbf{S} \tag{3.25}$$

where the solution vector $\mathbf{\Psi}$, the source vector $\mathbf{S}$ and the matrix $\mathbf{A}$ are given by:

$$\mathbf{\Psi} = \begin{bmatrix} \psi \\ u \\ w \end{bmatrix}, \qquad \mathbf{S} = \begin{bmatrix} -u \\ -D \\ 0 \end{bmatrix}, \qquad and \qquad \mathbf{A} = \begin{bmatrix} 0 & 0 & 0 \\ 0 & 0 & c^2 \\ 0 & 1 & 0 \end{bmatrix} \tag{3.26}$$

One feature that we desire our solutions to possess is that they are well-posed. This means that if $\mathbf{\Psi}(t, \bar{r})$ is a solution then $||\mathbf{\Psi}(t, \bar{r})|| \leq Ce^{bt} ||\mathbf{\Psi}(0, \bar{r})||$ where $\mathbf{\Psi}(0, \bar{r})$ are the initial conditions and b and C are positive constants. So in other words the solution does not grow faster in time than exponentially. This turns out to be important for the stability of the numerical evolution.

It is true that whether a solution is well-posed is very much related to how hyperbolic the system under study is. A system like (3.25) can either be strongly hyperbolic, symmetrically hyperbolic which automatically implies strong hyperbolicity, or weakly hyperbolic. It is also true that the modern ADM equations, cast in a first-order formalism, are weakly hyperbolic. This means that they need to be modified to an equivalent set of equations that is well-posed.

3.3 The BSSN formulation

There are several strongly or symmetric hyberbolic formulations of the Einstein equations but the system most widely used in numerical relativity is the Buamgarte-Shapiro-Shibata-Nakamura or BSSN formulation. In the case of the BSSN formulation the spatial metric is decomposed into:

$$\bar{\gamma}_{ij} = e^{-4\phi}\gamma_{ij} \tag{3.27}$$

Where $\bar{\gamma}_{ij}$ is defined as the conformal spatial metric and while ϕ is called the conformal factor and is chosen in such a way that the determinant $\bar{\gamma}$ of the conformal metric is equal to 1.

$$e^{4\phi} = \gamma^{1/3} \tag{3.28}$$

Furthermore the extrinsic curvature is decomposed into into its trace and its traceless part A_{ij}:

$$A_{ij} = K_{ij} - \frac{1}{3}\gamma_{ij}K \tag{3.29}$$

Finally the BSSN formulation uses the derivatives of the conformal spatial metric to define an additional spatial field $\bar{\Gamma}^i$ defined by:

$$\bar{\Gamma}^i = -\partial_j \bar{\gamma}^{ij} \tag{3.30}$$

Using these fundamental variables one can arrive to the following evolution equations:

$$\partial_t \phi = -\frac{1}{6}\alpha K + \beta^i \partial_i \phi + \frac{1}{6}\partial_i \beta^i \tag{3.31}$$

$$\partial_i \bar{\gamma}_{ij} = -2\alpha \bar{A}_{ij} + \beta^k \partial_k \bar{\gamma}_{ij} + \bar{\gamma}_{ik}\partial_j \beta^k + \bar{\gamma}_{kj}\partial_i \beta^k - \frac{2}{3}\bar{\gamma}_{ij}\partial_k \beta^k \tag{3.32}$$

$$\partial_t K = -\gamma^{ij} D_j D_i \alpha + \alpha(\bar{A}_{ij}\bar{A}^{ij} + \frac{1}{3}K^2) + 4\pi\alpha(\tau + S) + \beta^i \partial_i K \tag{3.33}$$

$$\begin{aligned} \partial_t \bar{A}_{ij} = e^{4\phi}(-D_{[i}D_{j]}\alpha + \alpha({}^{(3)}R_{[ij]} - 8\pi S_{[ij]})) + \alpha(K\bar{A}_{ij} - 2\bar{A}_{il}\bar{A}^l_j) + \\ \beta^k \partial_k \bar{A}_{ij} + \bar{A}_{ki}\partial_j \beta^k + \bar{A}_{kj}\partial_i \beta^k - \frac{2}{3}\bar{A}_{ij}\partial_k \beta^k \end{aligned} \tag{3.34}$$

$$\begin{aligned} \partial_t \bar{\Gamma}^i = -2\bar{A}^{ij}\partial_j \alpha + 2\alpha(\bar{\Gamma}^i_{jk}\bar{A}^{kj} - \frac{2}{3}\bar{\gamma}^{ij}\partial_j K - 8\pi\bar{\gamma}^{ij}S_j + 6\bar{A}^{ij}\partial_j \phi) + \\ \beta^j \partial_j \bar{\Gamma}^i - \bar{\Gamma}^j \partial_j \beta^i + \frac{2}{3}\bar{\Gamma}^i \partial_j \beta^i + \frac{1}{3}\bar{\gamma}^{il}\partial_l \partial_j \beta^j + \bar{\gamma}^{lj}\partial_j \partial_l \beta^i \end{aligned} \tag{3.35}$$

Where $X_{[ij]} = \frac{1}{2}(X_{ij} + X_{ji}) - \frac{1}{3}\gamma_{ij}X$ with X being the trace of X_{ij}. Also ${}^{(3)}R_{ij}$ can be expressed in terms of the BSSN variables as:

$${}^{(3)}R_{ij} = {}^{(3)}\ \bar{R}_{ij} - 2(\bar{D}_i \bar{D}_j \phi + \bar{\gamma}_{ij}\bar{\gamma}^{lm}\bar{D}_l \bar{D}_m \phi) + 4(\bar{D}_i \phi \bar{D}_j \phi - \bar{\gamma}_{ij}\bar{\gamma}^{lm}\bar{D}_l \phi \bar{D}_m \phi) \tag{3.36}$$

The BSSN formulation relies on the concept of conformal rescaling and it has been shown to be strongly hyperbolic.

3.4 Numerical computation of spatial derivatives

As it becomes apparent from the above analysis, the BSSN formulation requires the calculation of second-order partial derivatives. We consider a function $f(x)$ and we assume that we only know its value at equally spaced grid points $x_i = x_0 + i\Delta x$. The Taylor expansion of $f(x)$ around some value x_i is given by:

$$f(x_i \pm \Delta x) = f(x_i) \quad \pm \quad \Delta x \frac{df(x)}{dx}\Big)_{x=x_i} + \quad \frac{\Delta x^2}{2}\frac{d^2 f(x)}{dx^2}\Big)_{x=x_i} + \quad O(\Delta x^3) \quad (3.37)$$

From this expansion, the second derivative can be calculated as:

$$\frac{d^2 f(x)}{dx^2}\Big)_{x=x_i} \approx \quad \frac{f(x_i + \Delta x) - 2f(x_i) + f(x_i - \Delta x)}{\Delta x^2} \quad (3.38)$$

Where the error in this approximation is of order Δx^2. Equivalent approach get give us the second derivative as:

$$\frac{d^2 f(x)}{dx^2}\Big)_{x=x_i} \approx \quad \frac{2f(x_i) - 5f(x_i + \Delta x) + 4f(x_i + 2\Delta x) - f(x_i + 3\Delta x)}{\Delta x^2} \quad (3.39)$$

Where the error in this approximation is of order Δx^3. This method of calculation of derivatives is known as finite differencing and in practice we use approximations of fourth-order of accuracy or higher.

It becomes clear that to be possible to use the finite differencing method we need to cover the whole computational domain with grid points and for every one of these points store the values needed for the calculation of our derivatives. In many cases this is expensive from a computational perspective. For example when studying the gravitational radiation emitted from a rotating neutron star at a distance of at least a hundred times its radius, from the center of the star. To solve this problem we employ the use of nested meshes of grid points, its with a higher resolution than the previous one. This is what we

call the mesh refinement method and an example of it can be seen in figure (3.2). In other

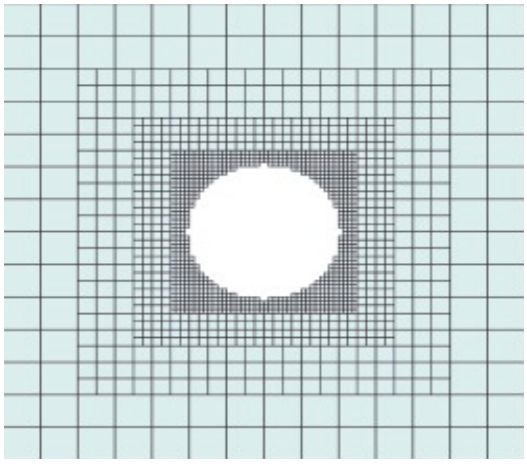

Figure 3.2: Mesh refinement around a spherical configuration.

words we use a denser mesh of grid points in this areas of the computational domain that higher accuracy is crucial if we wish to get good results, and less dense mesh of grid points in areas where high accuracy is not important.

For the projects studied for this thesis we use adaptive mesh refinement which is implemented through CARPET [12]. The adaptive part has to do with the fact that CARPET is able to implement not only static mesh refinement but also mesh refinement that adapts to the motion of our system. An example where this proves to be very useful is for systems of binary compact objects where the areas of interest, the parts of the computational domain where its moving object is, change as the system evolves.

3.5 Numerical time integration with the method of lines

At this point we are in a position to calculate the partial derivatives present in the BSSN formulation, so what we need to focus on is the matter of time integration. This is where the method of lines comes in, which is basically a technique that allows us to treat time and space variables separately.

We consider a partial differential equation of the following form:

$$\frac{\partial \Psi(t,x)}{\partial t} = S(t,x) + D\Psi(t,x) \tag{3.40}$$

where Ψ and S are vectors while D is a differential operator containing only spatial derivatives. As we have already discussed we can use methods of finite differentiation to calculate the spatial derivatives on the right hand side of (3.40), so if in this case the operator D is a second derivative with respect to x, for some random grid point i we would get:

$$\frac{\partial \Psi(t_i,x_i)}{\partial t} = S(t_i,x_i) + \frac{\Psi(t_i,x_i+\Delta x) - 2\Psi(t_i,x_i) + \Psi(t_i,x_i-\Delta x)}{\Delta x^2} \tag{3.41}$$

Given that there is no spatial derivatives on the left hand side we can move on and integrate our system in time dealing with it as an ordinary differential equation. The most commonly used methods for this task are the first order Euler's method, the second and fourth order Runge-Kutta methods and the sixth order Runge-Kutta-Fehlberg method. For the case of an ordinary differential equation of the form $\dot{y} = f(t,y)$, given that we know the state of our system at some time iteration t^m, the fourth order Runge-Kutta method gives us the state of our system at t^{m+1} by:

$$\begin{aligned}
&y^{m+1} = y^m + \frac{m_1}{6} + \frac{m_2}{3} + \frac{m_3}{3} + \frac{m_4}{6} + O(\Delta t^5) \\
&where \\
&m_1 = \Delta t f(t^m, y^m) \\
&m_2 = \Delta t f(t^m + \frac{\Delta t}{2}, y^m + \frac{m_1}{2}) \\
&m_3 = \Delta t f(t^m + \frac{\Delta t}{2}, y^m + \frac{m_2}{2}) \\
&m_4 = \Delta t f(t^m + \Delta t, y^m + m_3)
\end{aligned} \tag{3.42}$$

One last thing that needs to be discussed within this context is again the matter of numerical stability. As mentioned before for a scheme to be considered numerically stable

it needs not to grow faster in time than exponentially. For the Runge-Kutta method to be stable, the Courant-Friedrichs-Lewy condition needs to hold. This criterion states:

$$C = u\frac{\Delta t}{\Delta x} \leq C_{Max} \tag{3.43}$$

where C is the CFL factor, u is the speed of propagation, Δt is the time step, Δx is the spatial grid spacing and C_{Max} is some maximum value depending on the scheme used. The CFL criterion ensures that all the grid cells are causally connected to their neighbouring ones for every time step. So in other words it ensures that the numerical time evolution is not faster than the signal - causal propagation under study. Typically we set C_{Max} to be equal to $1/2$ while the value of the propagation of speed is usually the speed of light c.

3.6 Gauge choices for lapse and shift

One more thing that needs to be discussed within the context of the BSSN scheme is the evolution equations for the lapse α and the shift β^i or in other words the gauge conditions.

The evolution equation for the lapse function α, also known as time-slicing, is what determines the connection between the shapes of two neighbouring hypersurfaces Σ_{t_i} and $\Sigma_{t_{i+1}}$. This has to do with the fact that proper time can flow with a different rate at different points in space. So after a specific amount of coordinate time goes by, the position of a random point on some hypersurface Σ_{t_i} would depend on the value of the lapse at the corresponding point on $\Sigma_{t_{i-1}}$. On the other hand the evolution equations for the shift vector β^i determine how much the coordinates change from one hypersurface to the next.

The BSSN formulation does not prescribe a specific gauge condition so it would be useful to discuss a few possible choices and their issues.

Probably the most simple gauge conditions one can think of would be to set the lapse

function equal to unity an the shift function equal to zero.

$$\alpha = 1 \quad and \quad \beta^i = 0 \tag{3.44}$$

Such choice for α would mean that proper time would flow with the same rate at every point in space which would be equal to the flow rate of the coordinate time. This would also result in the Σ_t hypersurfaces to not change shape as time changes. The choice of zero shift on the other hand would result in the coordinate system not changing as we move from the one time hypersurface to the next. Thus a normal observer would not move with respect to the coordinate system. Choosing the lapse function to be equal to unity also means that the acceleration of a normal observer would be equal to zero, or in other words that normal observes would move along geodesics. This choice is known as the geodesic slicing and although it would simplify considerably most of our equations, it is not an acceptable choice. Just like geodesics converge in the presence of gravitating sources so would the coordinates in that case. This would lead to the formation of coordinate singularities.

Another interesting choice for the gauge conditions is that of maximal slicing for the lapse and minimal distortion for the shift. The maximal slice condition results in maximizing the volume of a hypersurface while the minimal distortion condition results in minimizing the shear deformation of an ideal spheroid with respect to our coordinates, as it evolves with time. Although these would be helpful properties, these conditions result in posing elliptic equations that need to be enforced in time and for that reason they can't be used with a hyperbolic evolution through the method of lines.

The standard choice for lapse is the so called 1+log slicing condition:

$$(\partial_t - \beta^i \partial_i)\alpha = -2\alpha K \tag{3.45}$$

If we set the shift equal to zero we get:

$$\partial_t \alpha = -2\alpha K = \gamma^{ij} \partial_t ln(\gamma_{ij}) = \partial_t ln(\gamma) \tag{3.46}$$

Integrating (3.45) and setting the integration constant equal to 1, we get $a = 1 + ln(\gamma)$.

On the other hand the most common choice for the shift is a gamma-driver:

$$\begin{aligned} \partial_t \beta^i &= \frac{3}{4} B^i \\ \partial_t B^i &= \partial_t \bar{\Gamma}^i - \eta B^i \end{aligned} \tag{3.47}$$

Where B is a variable used to get a first order system while η a parameter usually connected to the total mass of the system under study.

These choices for the lapse and the shift have been studied along the BSSN scheme and it turned out that such a system is strongly hyperbolic.

3.7 General relativistic hydrodynamics

As we have discussed before, the behaviour of space-time depends on the behaviour of the energy and momentum that is contained within it. The content of energy-momentum is described by the the stress energy tensor $T^{\mu\nu}$. Given that we are not working empty space as in the case of black hole simulations, in our case $T^{\mu\nu}$ is not equal to zero.

For our simulations we consider the simplest case of an ideal fluid without any other possible contributions like magnetic fields or imperfect gasses. In such case the stress energy tensor is given by:

$$T^{\mu\nu} = \rho h u^\mu u^\nu + p g^{\mu\nu} \tag{3.48}$$

where ρ is the rest mass density, u^μ is the fluid 4-velocity, p is the pressure and h is the specific enthalpy given by $h = 1 + \epsilon + \frac{p}{\rho}$ with ϵ being the specific energy density in the rest frame of the fluid.

Since the fluid is not remaining still during the evolution we need to put in place certain evolution equations that will govern the behaviour of the fluid variables. These are the continuity equation:

$$\nabla_\mu \rho u^\mu = 0 \tag{3.49}$$

which ensures the conservation of rest mass, and the Bianchi identities

$$\nabla_\mu T^{\mu\nu} = 0 \tag{3.50}$$

which ensure the local conservation of energy-momentum.

In reality we don't evolve the so called primitive variables ρ, h and p. It is more preferable to use the Valencia formulation [13] and evolve the so called conservative variables:

$$\begin{aligned} D &= \rho W \\ S_i &= \rho h W^2 \\ E &= \rho h W^2 - p - D \end{aligned} \tag{3.51}$$

where D is the rest mass density with respect to the simulation frame, S_i is the momentum density and E is the energy. The evolution equations in this case are:

$$\begin{aligned} \mathcal{L}_n D &= KD - \frac{1}{\alpha} D_k(\alpha D v^k) \\ \mathcal{L}_n S^i &= -\frac{1}{\alpha}(E+D)D^i\alpha + KS^i - \frac{1}{\alpha} D_k[\alpha(S^i v^k + \gamma^{ik} p)] \\ \mathcal{L}_n E &= (E+p+D)[v^i v^j K_{ij} - \frac{1}{\alpha} v^i \partial_i \alpha] + K(E+p) - \frac{1}{\alpha} D_k[\alpha v^k (E+p)] \end{aligned} \tag{3.52}$$

Where D^k is the covariant derivative in the spatial hypersurface.

The last thing that we need at this point to close the system, is an equation of state. This is an equation that relates the basic thermodynamic quantities within the star and is usually in the form of $p = p(\rho, \epsilon)$. Given that the interior of a relativistic star is a

complicated system, a realistic equation of state can get very complicated and there exists a large number of possible candidates. Figuring out accurate equations of state for relativistic stars is one of the main objectives in the field of gravitational wave asteroseismology. The simplest cases are that of the ideal fluid equation of state:

$$p = (\Gamma - 1)\rho\epsilon \tag{3.53}$$

and the polytropic equation of state:

$$p = K\rho^{\Gamma} \tag{3.54}$$

Having an equation of state allows us to convert from the primitive to the conservative variables at will.

3.8 The Einstein Toolkit

The Einstein toolkit [12] is a community driven, freely accessible computational infrastructure intended for use in numerical relativity and relativistic astrophysics. It implements space-time evolution via the BSSN evolution system and general relativistic hydrodynamics in a finite volume-discretization. The modules of the Einstein Toolkit center around a set of core modules that provide basic functionality to create and manage a numerical simulation starting from the code generation all the way to the simulation results. This core consists of: (a) The Cactus framework which is an open source, modular environment that consists of general modules, called thorns, that provide parallel drivers, coordinates, boundary conditions, interpolators and efficient input/output in different data formats. Although Cactus is completely modular it contains a small core called $flesh$ which provides the interface between modules both at compile and run-time. (b) The Carpet driver, which is built on top of Cactus, and provides problem independent mesh refinement support. (c) The Simulation Factory which provides a uniform, high-level interface to common opera-

tions. (d) Krank, which generates code in computer language from a high-level description in Mathematica.

Although a simulation can make use of just one module, in practise the vast majority of the simulations used for numerical General Relativity purposes consist of hundreds of components. In general a simulation consists of base modules that declare commonly used variables and define their meaning and units, initial data modes that depend on the properties of the astrophysical objects under study, modes that provide different evolution methods for vacuum and matter configurations, modes that deal with the thermodynamic properties of our systems and finally analysis modules.

In our group at Georgia Tech, besides the Einstein Toolkit thorns, we also develop and maintain our own space-time, hydrodynamics and analysis thorns which are called Maya.

3.9 RNS Code

All the initial models used for our simulations are generated using the RNS code [14]. In this case a model is specified by its central density ρ_c, the ratio of polar to equatorial coordinate radii and the polytropic constants K and Γ. The models we use are assumed to be stationary, axisymmetric, uniformly rotating perfect fluid solutions of the Einstein field equations. The metric in this case is given by:

$$ds^2 = -e^{\gamma+\rho}dt^2 + e^{\gamma-\rho}\bar{r}^2 sin^2\theta(d\phi - \omega dt)^2 + e^{2\alpha}(d\bar{r}^2 + \bar{r}^2 d\theta^2) \tag{3.55}$$

where ρ, γ, α and ω are metric potentials that depend only on $\bar{r}$ and θ. As we can see the metric does not depend on the coordinates ϕ and t due to the axisymmetry and time independence of the models under study. Quantity $\frac{1}{2}(\gamma + \rho)$ is the general relativistic generalization of the Newtonian gravitational potential, quantity α specifies of the two-surfaces of constant t and θ and quantity ω is the angular velocity around the symmetry axis.

CHAPTER 4

RESULTS 1: CODE TESTING

After reaching a point where our code is in order and seems to be able to evolve single rotating neutron star configurations, both in full general relativity and under the Cowling approximation, without presenting any noticeable issues, our next task is to test its stability and validate its results against already published work.

4.1 Code tests

We decided to first test our code on the equilibrium BU series models, the characteristics of which can be seen in table 4.1. Here we use the system of geometrical units of measurement. The logic behind this system is explained in appendix A. The Keplerian angular velocity Ω_k of a rotating equilibrium model refers to the maximum angular velocity that this model can reach before the centrifugal force due to rotation overcomes the gravitational force and starts tearing the outer parts of the star apart.

Table 4.1: Equilibrium properties of the initial models as described by a polytropic EOS $p = K\rho_0^{\Gamma}$ where $\Gamma = 2$, $K = 100$. The entries in the table are ρ_c the central rest mass density, M the gravitational rest mass, r_e the equatorial radius, r_p/r_e the ratio of the equatorial to the polar radius, $T/|W|$ the ratio of rotational to gravitational binding energy and Ω/Ω_k the ratio of the angular velocity over the Keplerian angular velocity.

Models	$\rho_c \times 10^3$	$M(M_\odot)$	$r_e(M_\odot)$	r_p/r_e	$T/\|W\|$	Ω/Ω_k
BU0	1.28	1.400	9.59	1.00	0.000	0.0000000
BU1	1.28	1.432	9.83	0.95	0.012	0.29700272
BU2	1.28	1.466	10.11	0.90	0.024	0.43117977
BU3	1.28	1.503	10.42	0.85	0.037	0.5384615
BU4	1.28	1.543	10.78	0.80	0.050	0.6323012
BU5	1.28	1.585	11.20	0.75	0.062	0.7228346
BU6	1.28	1.627	11.69	0.70	0.074	0.8076285
BU7	1.28	1.666	12.30	0.65	0.084	0.8500000

The initial neutron star configurations are constructed by the well established RNS code which has been incorporated into the MAYA code through the RNSID thorn. Figure 4.1 shows the initial data for the rest mass density profile of the two extreme cases of the BU series. For each case the whole initial configuration is contained within a uniform three-dimensional grid the outer boundary of which is roughly 1.6 times the stellar equatorial radius of the model under study. The coordinate system that is being used is oriented in such a way that the z-axis coincides with the axis of rotation of the star. In this figure

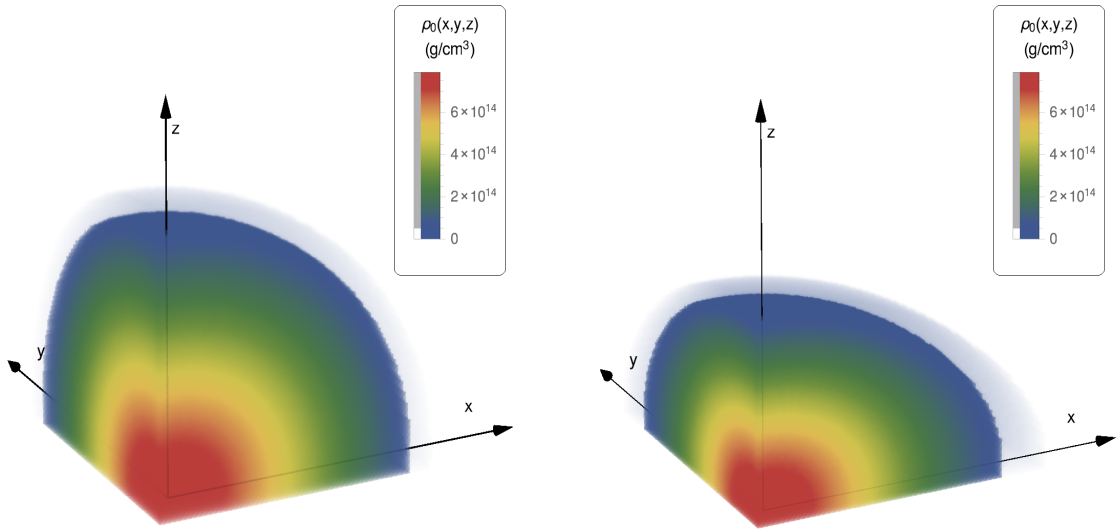

(a) BU0 equilibrium model

(b) BU7 equilibrium model

Figure 4.1: Initial rest mass density profiles of the two extreme cases of the BU series models.

one can also observe how rotation affects the shape of a neutron star. As the angular velocity Ω increases the centrifugal forces break the spherical symmetry that characterizes the non rotating configuration, causing the star to assume the shape of an oblate spheroid the ellipticity of which increases with the rotational frequency. Finally, to avoid problems at the interface at the surface of the star we have employed the use an artificial atmosphere the density of which is roughly ten orders of magnitude less than the central rest mass density. A reasonable approximation for the Keplerian angular velocity is given by $\Omega_K \approx \frac{2}{3}\sqrt{\pi G \rho_0}$.

4.1.1 Code stability: long term evolution

For the most part this thesis is dedicated to the study of modes of oscillation that could be present in neutron stars and whether such modes could lead to detectable gravitational radiation. The frequencies of the modes that we are interested in are of the order of kHz. Thus for a clear detection and identification of such modes we have chosen to evolve most of our simulations for about 10 - 15 milliseconds. This allows for modes of such frequencies to complete enough cycles that would make their detectability possible.

It is customary as a first stability test to check whether a code can evolve steadily for at least ten times the amount of the average evolution time that is going to be used in the simulations of interest. We applied this test to the BU0 non rotating equilibrium model which for this case was studied in the Cowling approximation. This model was allowed to evolve for a period of 150 milliseconds and no initial external perturbation was applied. Figure 4.2 shows the time evolution of the rest mass density of all the grid points on the xy-plane inside the star the distance of which from the center is roughly half that of the stars' radius. Figure 4.3 shows the time evolution of the rest mass and logarithmic rest mass density along the x coordinate axis of the star. As can be seen in both these figures there is no visible concerning issue.

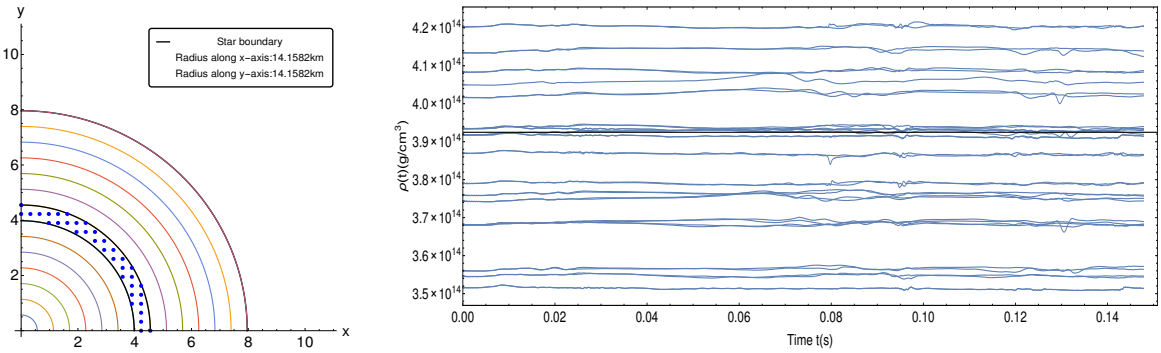

Figure 4.2: Time evolution of the rest mass density for the long-term evolution of the unperturbed equilibrium BU0 model. The left side shows the grid points inside the star that the rest mass density time series were extracted from while the right part shows the time evolution of these time series.

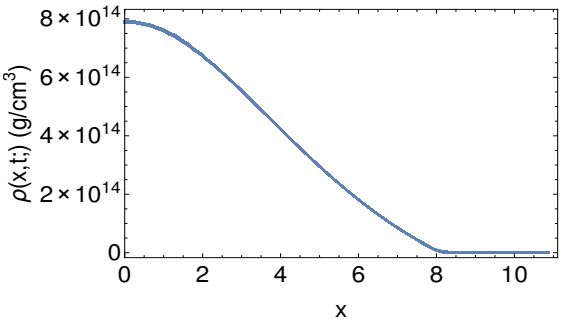

(a) Rest mass density.

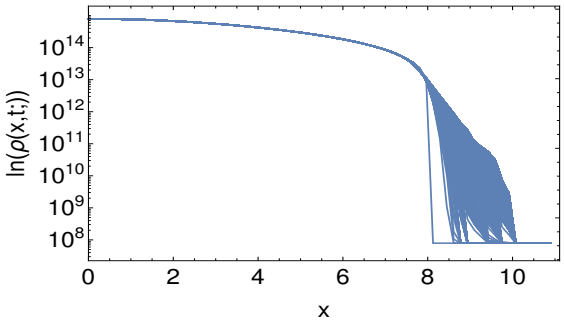

(b) Logarithmic rest mass density.

Figure 4.3: Time evolution of the rest mass and logarithmic rest mass density profiles along the x coordinate axis for the unperturbed equilibrium BU0 model evolved in the Cowling approximation.

Although we apply no initial external perturbation on the star, so in principle one would expect no density, pressure or velocity time fluctuations to be present, numerical inaccuracies do result in such fluctuations. By applying fast Fourier transforms on the time series shown in figure 4.3 we get the results presented in figure 4.4.

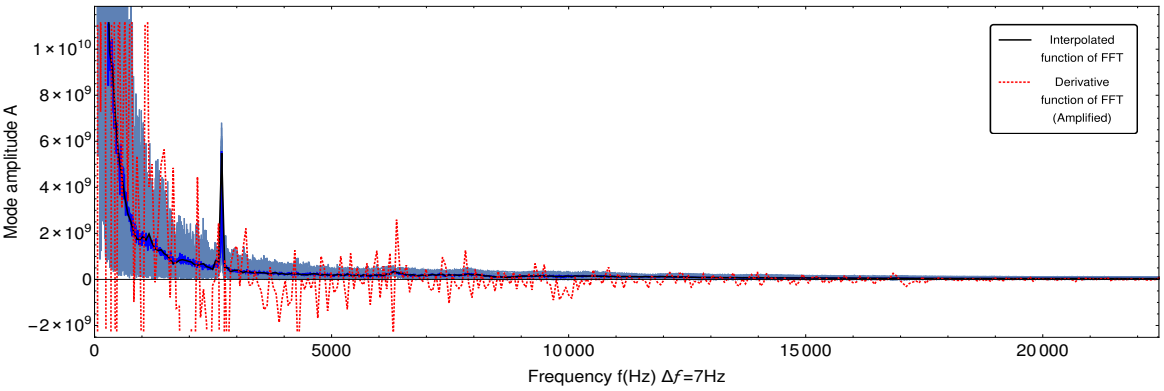

Figure 4.4: Fast Fourier transforms of the rest mass density time series shown in figure 4.2.

The fast Fourier transforms in this region of the star reveal the existence of one mode of oscillation characterized by a frequency of 2705.69 Hz. According to [8] this is the exact frequency observed for the fundamental radial mode of oscillation for the BU0 model. Similar study of the time evolution of the rest mass density at the center of the star, the region which traditionally is studied when looking for radial modes, gives accurate results for the higher order radial modes that have been observed for this model.

As part of the stability test we also studied three more cases. The BU0 equilibrium model in full GR and the rapidly rotating BU7 equilibrium model both in full GR and in the Cowling approximation. This time we allowed our unperturbed configurations to evolve for approximatively 30 milliseconds. Figures 4.5 through 4.7 show the time evolution of the rest mass and logarithmic rest mass density along the x coordinate axis for these cases. From these results we can see that shifting from the Cowling approximation to a full general relativistic case for the same models, has no affect on the stability of the simulations. The same can be said when shifting from a non-rotating case to a rapidly rotating one. Depending on these results we can confidently say that our code is reliable when it comes to steadily evolving rotating neutron star configurations.

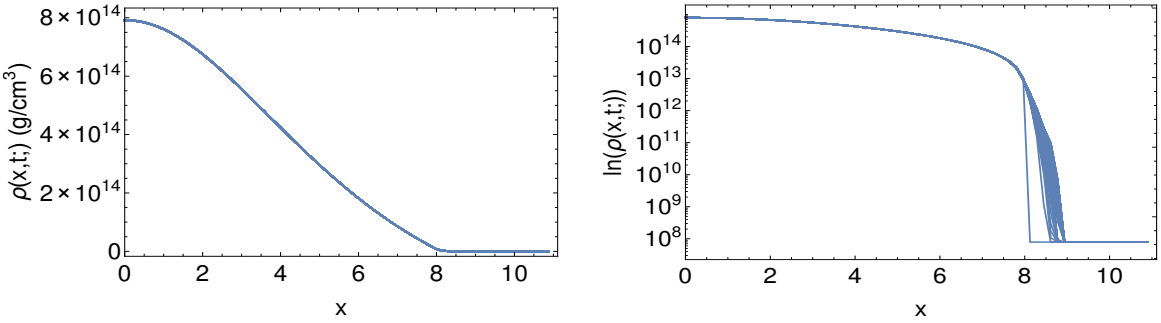

(a) Rest mass density. (b) Logarithmic rest mass density.

Figure 4.5: Time evolution of the rest mass and logarithmic rest mass density profiles along the x coordinate axis for the unperturbed equilibrium BU0 model evolved in full GR.

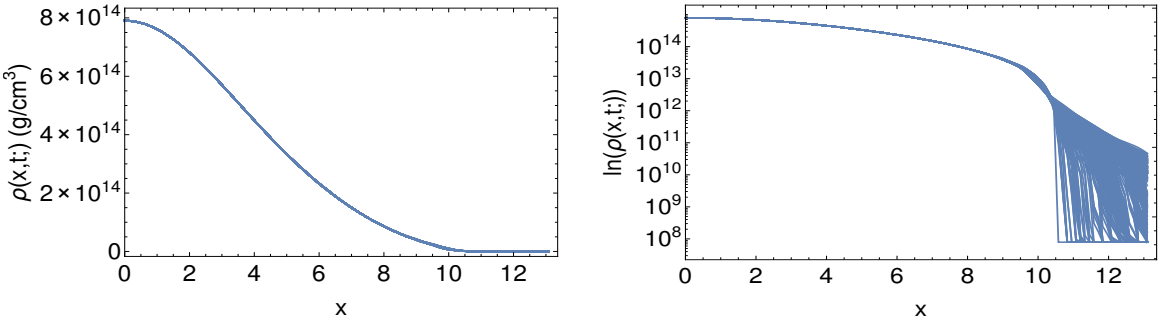

(a) Rest mass density. (b) Logarithmic rest mass density.

Figure 4.6: Time evolution of the rest mass and logarithmic rest mass density profiles along the x coordinate axis for the unperturbed equilibrium BU7 model evolved in the Cowling approximation.

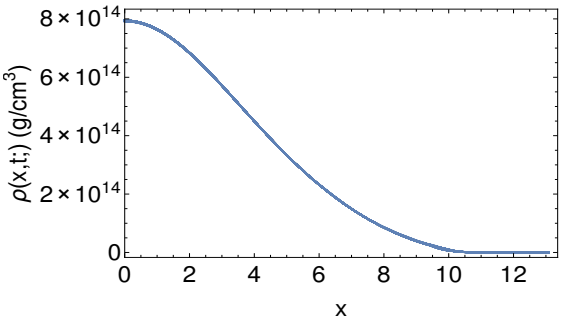

(a) Rest mass density.

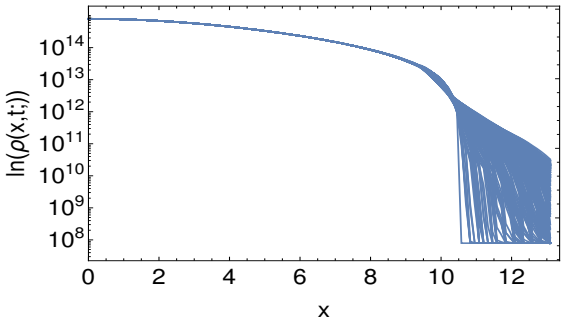

(b) Logarithmic rest mass density.

Figure 4.7: Time evolution of the rest mass and logarithmic rest mass density profiles along the x coordinate axis for the unperturbed equilibrium BU7 model evolved in full GR.

4.1.2 Convergence test

The main goal of the study of some physical system is to acquire these physical values that will accurately describe the state of the system under study. For example, when studying the motion of a charged particle inside a magnetic field we need for every moment to know the velocity and position of that particle and the value of the magnetic field at every point in the region under study. In the case of the numerical study of some physical quantity we assume that there exists an exact value u which we approximate with a value $\tilde{u}(h)$, with h being a small parameter like the numerical grid size or time step. For a sufficiently small h we say that the numerical method used is of order p if there exists a number C, independent of h, such that

$$|\tilde{u}(h) - u| \leq Ch^p, \tag{4.1}$$

The constant C typically depends on the exact solution and the error $\tilde{u}(h) - u$ depends smoothly on h. In this case we have

$$\tilde{u}(h) - u = Ch^p + O(h^{p+1}), \tag{4.2}$$

For this test we want to examine the order of convergence p of our numerical method. Since we don't know the theoretically correct values needed to describe the state of the

systems we wish to study, there exist two main methods that can be followed. The first and most expensive one is to compute the numerical solution $\tilde{u}(h)$ using a very small h and consider this to be the known u. The second method is to examine the ratios of differences between $\tilde{u}(h)$ for different values of h. For this method it is common to compare solutions with h being divided in half successively. In this case we have

$$\frac{\tilde{u}(h) - \tilde{u}(h/2)}{\tilde{u}(h/2) - \tilde{u}(h/4)} = \frac{1 - 2^{-p} + O(h)}{2^{-p} - 2^{-2p} + O(h)} = 2^p + O(h), \tag{4.3}$$

In our case we considered a neutron star model with a specific diameter d uniformly discretized by k grid points of size h. For three different resolutions, thus three different numbers of grid points across the star $\{k, \dot{k}, \ddot{k}\}$ and grid sizes $\{h, \dot{h}, \ddot{h}\}$, we get

$$\begin{cases} d = k \cdot h \\ d = \dot{k} \cdot \dot{h} \\ d = \ddot{k} \cdot \ddot{h} \end{cases} \Rightarrow \begin{cases} \dot{h} = (k/\dot{k}) \cdot h \\ \ddot{h} = (k/\ddot{k}) \cdot h \end{cases} \Rightarrow \frac{\tilde{u}(h) - \tilde{u}(\dot{h})}{\tilde{u}(\dot{h}) - \tilde{u}(\ddot{h})} = \frac{1 - (k/\dot{k})^p}{(k/\dot{k})^p - (k/\ddot{k})^p}, \tag{4.4}$$

The model we studied for this test is the BU0 model. The study was done in full general relativity for three different resolutions and the quantity u under study was the rest mass density ρ_c at the center of the star.

For every different case the system was initially perturbed on the rest mass density with a radial perturbation and was let to evolve for around 14 milliseconds. Figure 4.8 shows the time evolution of the rest mass density at the center of the star for a discretization of 80, 120 and 160 grid points across the diameter of the star while figure 4.9 shows the corresponding convergence plot.

From these figures we can see that our code seems to converge. Regarding the order of convergence though it is not possible to get clear results. The limited amount of the time evolution of this test only allows us to conclude that the p ranges between 1 and 4 which does not help much.

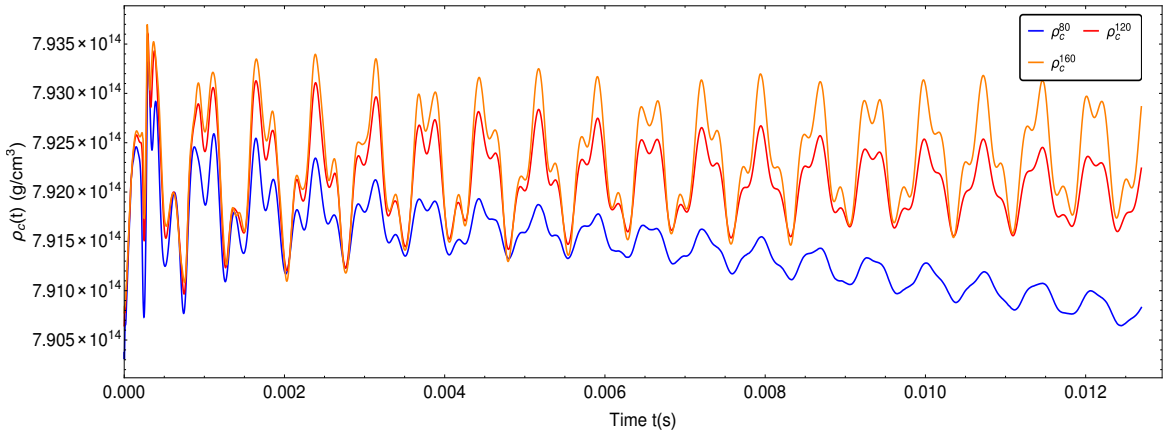

Figure 4.8: Time evolution of the central density of the BU0 model evolved in full general relativity for three different grid resolutions.

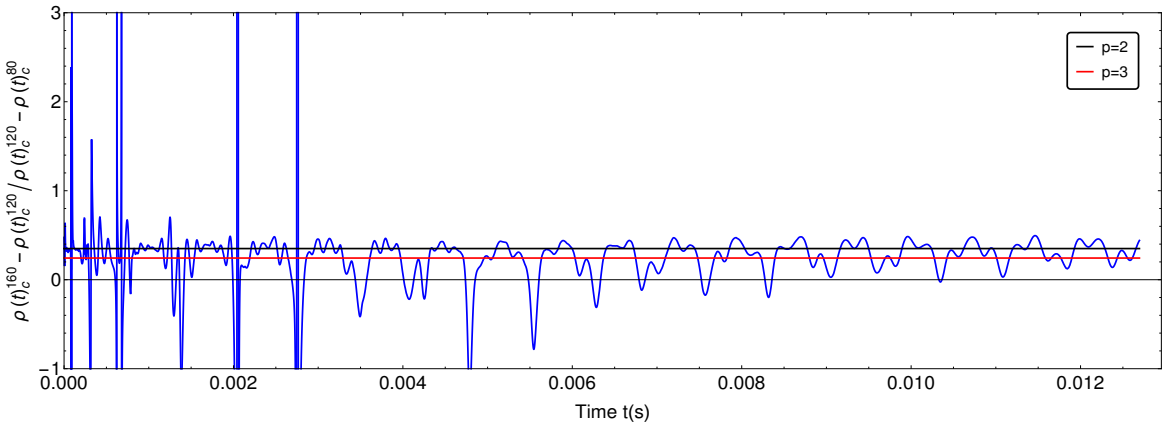

Figure 4.9: Convergence plot corresponding to the central density time series shown in figure 4.8.

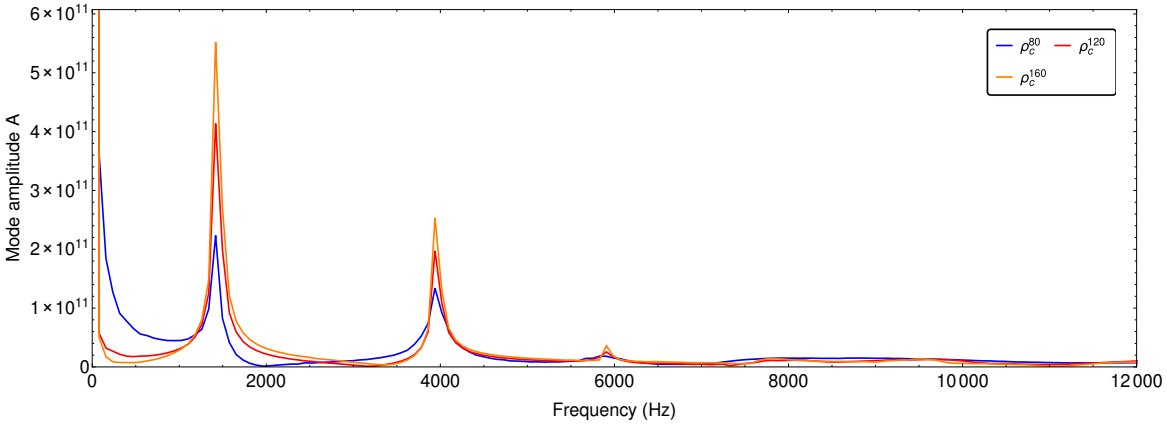

Figure 4.10: Fast Fourier transforms corresponding to the central density time series shown in figure 4.8.

Finally figure 4.10 shows the fast Fourier transforms of these central density time series. In all three cases we observe three main modes of oscillation, a fundamental radial mode at 1419 Hz and two higher order radial modes at 3920 Hz and 5880 Hz. These results are virtually identical independent of the resolution used and from [10] we can see that they are the accepted results for this specific model and approximation.

4.1.3 Accuracy test

As mentioned above the main purpose of the projects described in this thesis is to use our code to perform gravitational wave asteroseismology from neutron stars. It is natural that for our final test we need to check how reliable our code is regarding producing acceptable mode frequency results. The best way to do so is by trying to reproduce already established results that can be found in the literature.

A. Oscillations of a non rotating neutron star

Following the logic of [11] we first studied the spherically symmetric $l = 0$ fundamental (F) mode and the axisymmetric non radial $l = 2$ f-modes (which are degenerate in m for a spherically symmetric background) on the non rotating model of the BU series. To achieve observing this modes we need to perturb our initial steady configuration in such a way as to guide energy mainly towards the modes that we are interested in. So for the spherically symmetric fundamental mode we impose an initial perturbation on the rest mass density of our star described by (4.5) and for the axisymmetric non radial f-modes an initial perturbation described by (4.6).

$$\delta\rho = A \cdot \rho_c \cdot cos(\frac{\pi \cdot r}{2 \cdot r_s}) \tag{4.5}$$

$$\delta\rho = A \cdot \rho_c \cdot sin(\frac{\pi \cdot r}{r_s}) \cdot (3 \cdot (\frac{z}{r})^2 - 1) \tag{4.6}$$

where A is an arbitrary small amplitude which we set to 10^{-3} times the central density, r is the radial coordinate and r_s is the coordinate radius at the surface of the star. The initial perturbation on the rest mass density can be seen in figures 4.11 and 4.12.

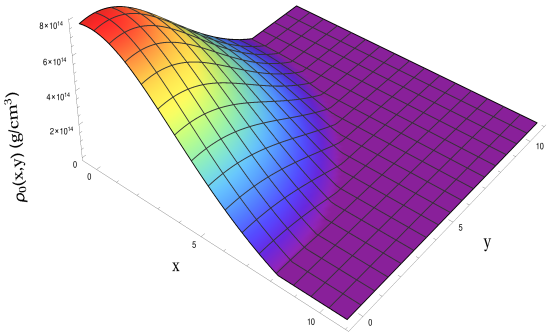

(a) xy - plane

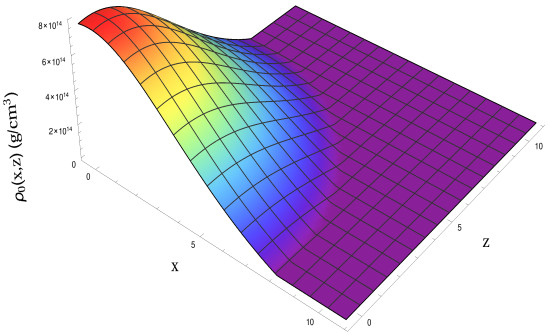

(b) xz - plane

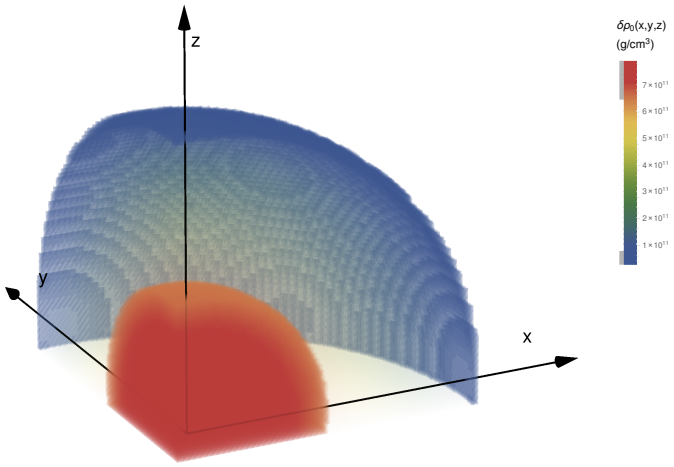

(c) Full configuration.

Figure 4.11: Initial perturbation profiles on the rest mass density of the spherically symmetric BU0 equilibrium model for the $l = 0$, $m = 0$ radial perturbation.

After applying these perturbations, we allow our configurations to evolve for around 15 milliseconds. This is enough time for the modes that we are interested in to complete enough cycles, which will allow for an accurate extraction of their frequencies and corre-

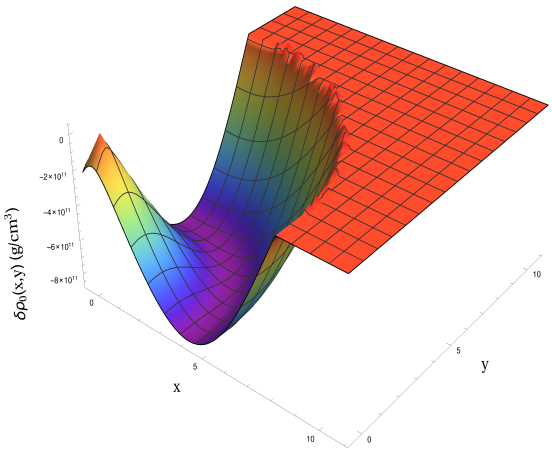

(a) xy - plane

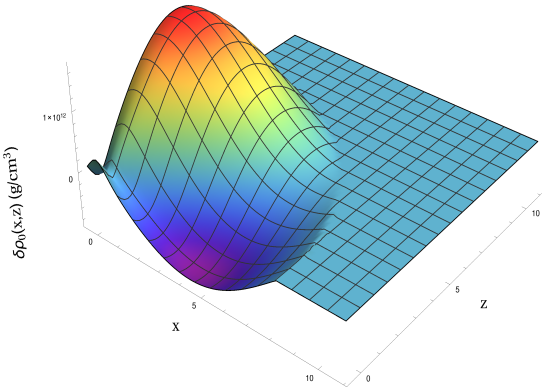

(b) xz - plane

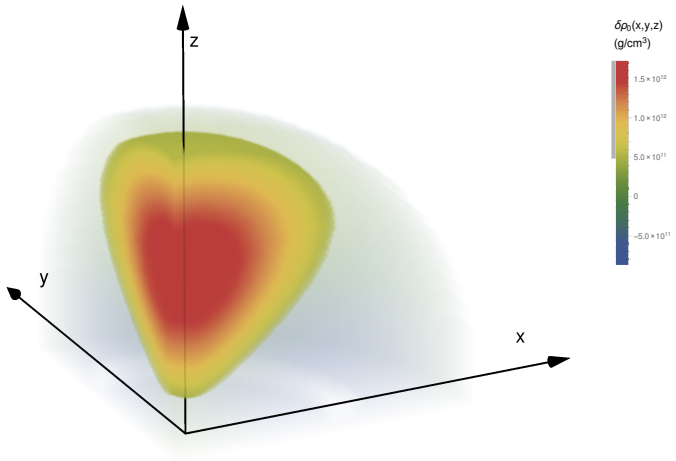

(c) Full configuration.

Figure 4.12: Initial perturbation profiles on the rest mass density of the spherically symmetric BU0 equilibrium model for the $l = 2$, $m = 0$ axisymmetric non radial perturbation.

sponding oscillation patterns.

To identify the modes of oscillation that interest us and calculate their frequency, we need to collect for every grid point within our star the time series that represent how the hydrodynamical quantities (namely the rest mass density ρ, the pressure p and the spatial velocities v^i) evolve with time. Later on, in post processing, we perform fast Fourier transforms on all these time series, and calculate the dominant frequencies. Finally for every

one of the observed frequencies we study how their corresponding amplitudes variate with respect to the position of the grid point within the star. In other words for every mode of oscillation we study its amplitude as a function of the spatial coordinates thus forming what is known as the eigenfunction of this mode. For this purpose we separate the grid space inside the star in various regions (which we call fft regions) and for every region separately we study how the hydrodynamical quantities evolve for their interior points. Examples of this procedure can be seen in figures 4.13 and 4.14.

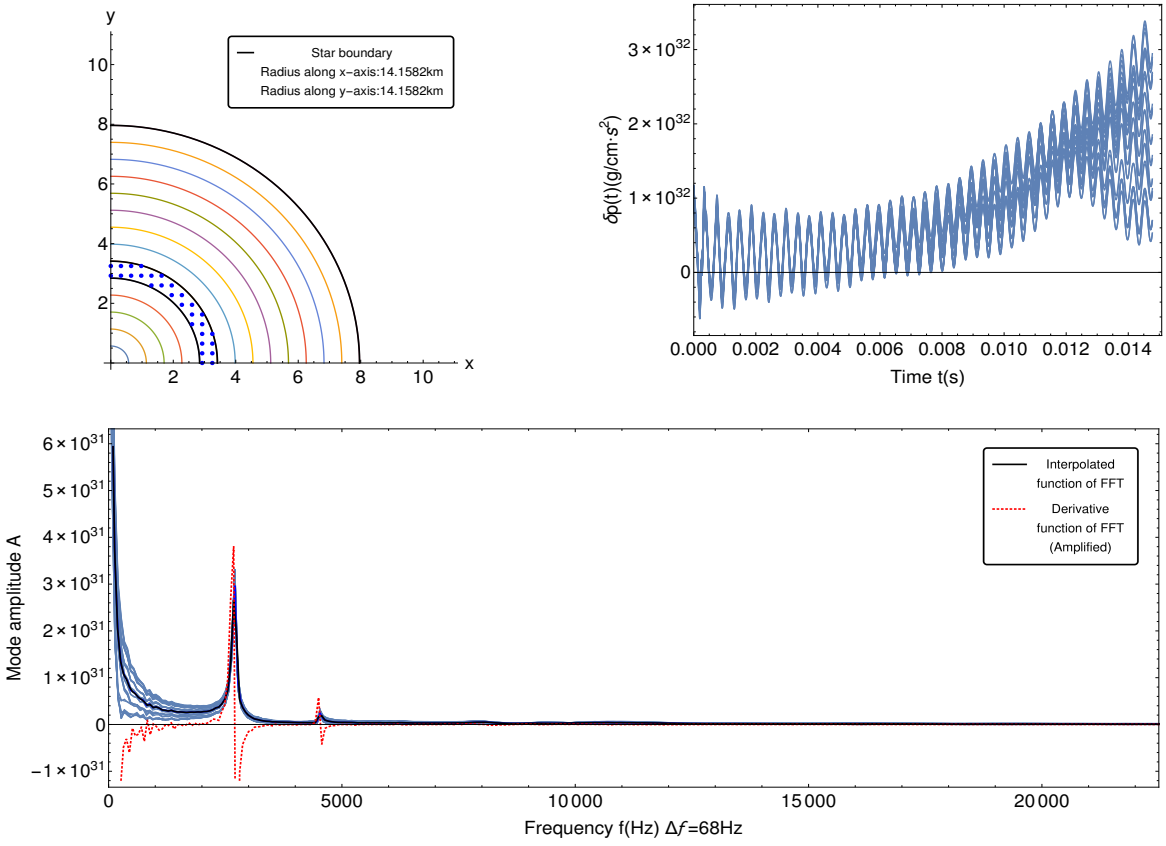

Figure 4.13: Time evolution of the pressure on the xy-plane for the BU0 equilibrium model. The evolution took place under the Cowling approximation with an $l = 0$, $m = 0$ radial initial perturbation.

In these two examples, for every one of the grid points inside the marked regions, seen at the upper left corner of these figures, we plot the time series $\{\delta q_i(t)\} = \{q_i(t) - q_i^{0,u}\}$. Where $q_i(t)$ referrers to one of the hydrodynamical quantities of the perturbed configuration at some grid point with an index i and $q_i^{0,u}$ to the initial value of this quantity at the same

point but for the unperturbed configuration. These plots can be seen on the upper right corner of our figures. Finally we perform a fast Fourier transform on every one of these time series. These fft plots can be seen at the bottom of these figures. The thick black line is in a way the average fft of this region and the red dotted line refers to the derivative of the average fft (amplified).

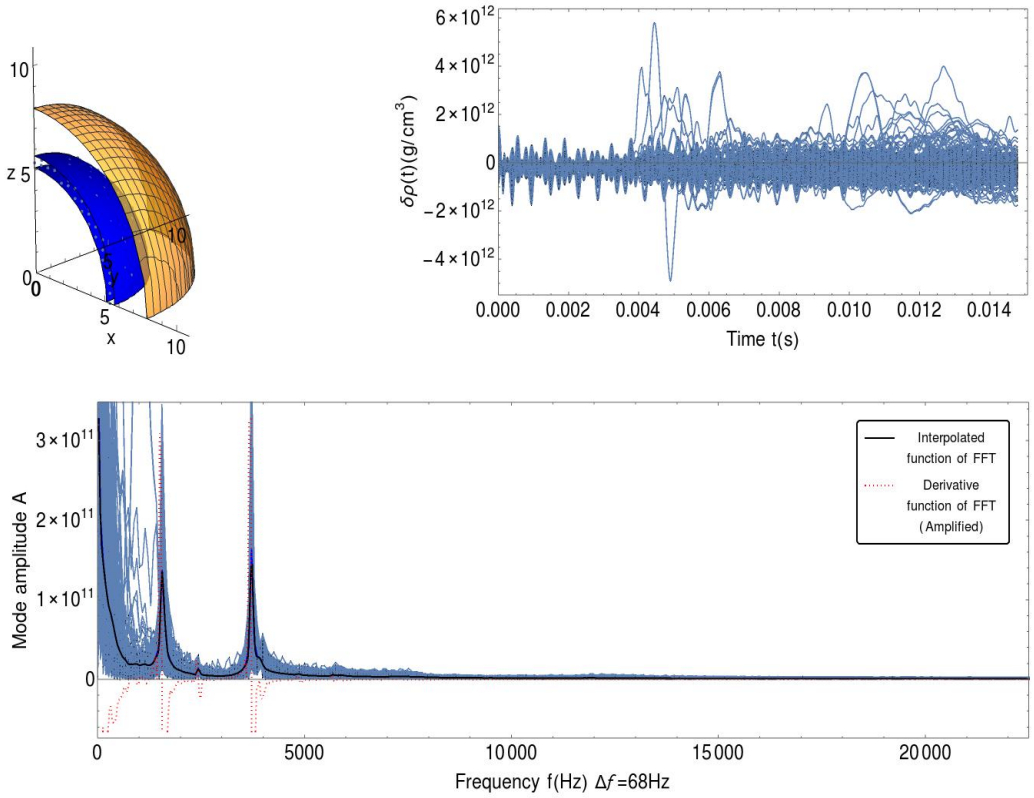

Figure 4.14: Time evolution of the rest mass density for the BU0 equilibrium model. The evolution took place in full general relativity with an $l = 2$, $m = 0$ axisymmetric non radial initial perturbation.

This procedure serves two main purposes. The first one has to do with the fact that depending on the initial perturbation that we apply to our star, we direct energy to different modes of oscillation and consequently cause points in different parts of the star to oscillate with different amplitudes. For example with an initial perturbation of the form of 4.5, we expect points closer to the center of the star to oscillate with larger amplitudes than points closer to the atmosphere, while with an initial perturbation like 4.6, we expect the opposite.

The second purpose is that as part of our future work we may want to study differentially rotating neutron stars, namely stars that dont rotate uniformly.

Finally for every one of the dominant peaks observed, we plot their fft amplitude as a function of the coordinates of the grid point out of which we extracted the corresponding time series. The fft algorithm used for this procedure is described by (4.7) where n is the number of points of the discrete time series under study.

$$Y(k) = \frac{1}{n} \sum_{j=1}^{n} q(j) e^{-\frac{2\pi i}{n}(j-1)(k-1)} \tag{4.7}$$

The result of this procedure is for every frequency k to get the corresponding amplitude of oscillation. The functions created following this procedure is what we define as the eigenfunction of the corresponding mode of oscillation, for this specific frequency. Examples can be seen in figures 4.15 to 4.18.

Studying the eigenfunctions of the modes that are observed is important when it comes to obtaining information about the nature of these modes of oscillation. For example in figures 4.15 and 4.16 we can observe the eigenfunctions corresponding to the fundamental (F) and the first higher order (H1) radial modes of oscillation, while figures 4.17 and 4.18 show the eigenfunctions that correspond to the axisymmetric non radial f- and p-modes of oscillation. These eigenfunctions appear during the study of the BU0 equilibrium model in the Cowling approximation. What is apparent from these graphs is that the eigenfunctions observed resemble very closely the profile of the initial perturbation that caused their existence. This resemblance is what leads to the identification of the nature of these modes.

After studying the evolution of the non rotating equilibrium BU0 model both in the Cowling approximation and in full General Relativity and both for an $l = 0, m = 0$ radial initial perturbation and an $l = 2, m = 0$ axisymmetric non radial initial perturbation all the results that we got are very close to the ones that exist in the literature for the same model [8,9,10].

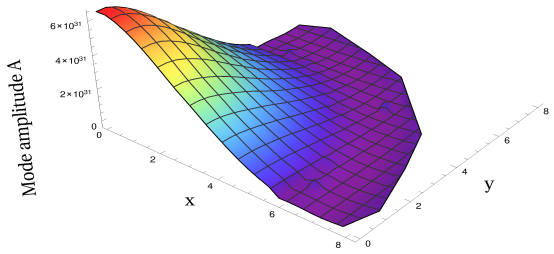

(a) F-mode, Frequency: 2706 Hz, xy-plane

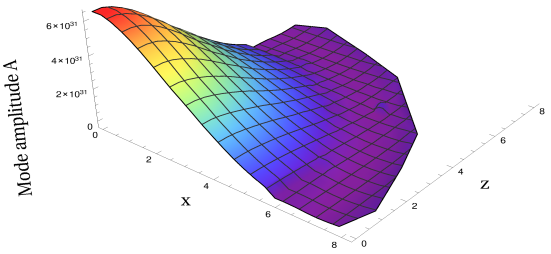

(b) F-mode, Frequency: 2706 Hz, xz-plane

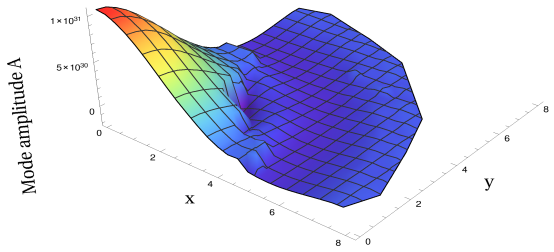

(c) H1-mode, Frequency: 4532 Hz, xy-plane

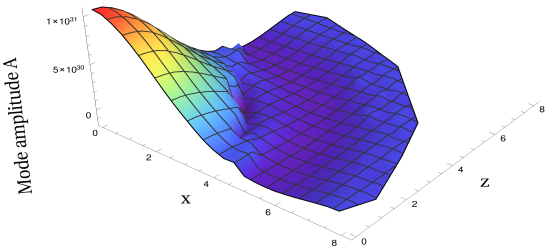

(d) H1-mode, Frequency: 4532 Hz, xz-plane

Figure 4.15: Pressure eigenfunctions of the dominant modes of oscillation that appear during the study of the BU0 equilibrium model. The evolution took place under the Cowling approximation with an $l = 0$, $m = 0$ radial initial perturbation.

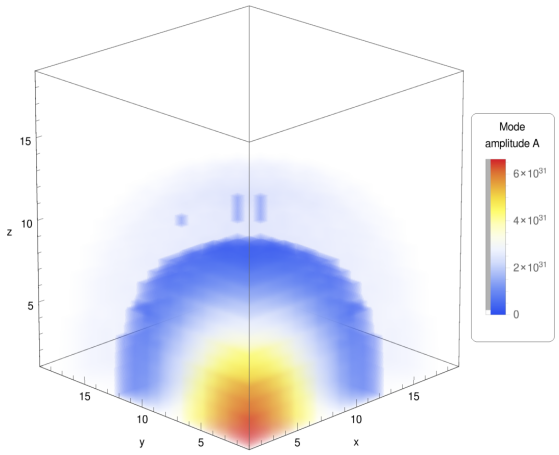

(a) F-mode, Frequency: 2706 Hz

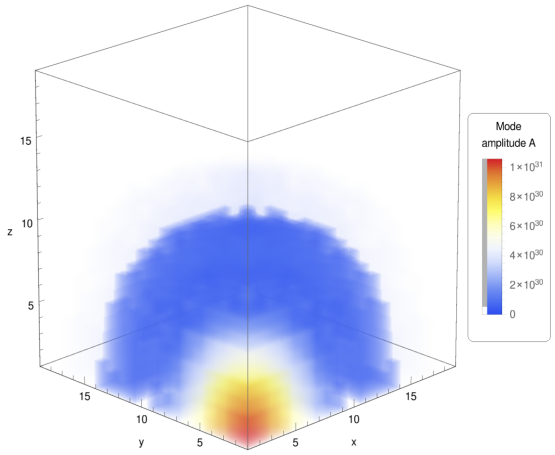

(b) H1-mode, Frequency: 4532 Hz

Figure 4.16: Pressure eigenfunctions of the dominant modes of oscillation that appear during the study of the BU0 equilibrium model. The evolution took place under the Cowling approximation with an $l = 0$, $m = 0$ radial initial perturbation.

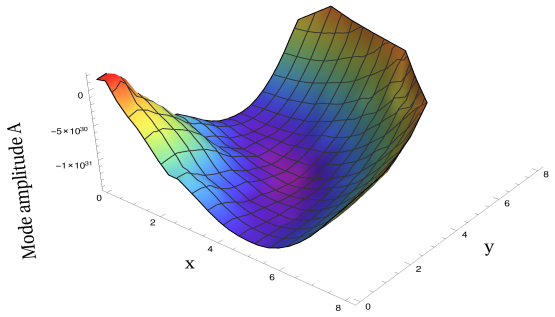

(a) f-mode, Frequency: 1894 Hz, xy-plane

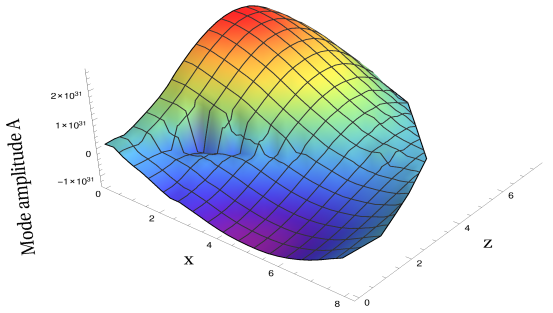

(b) f-mode, Frequency: 1894 Hz, xz-plane

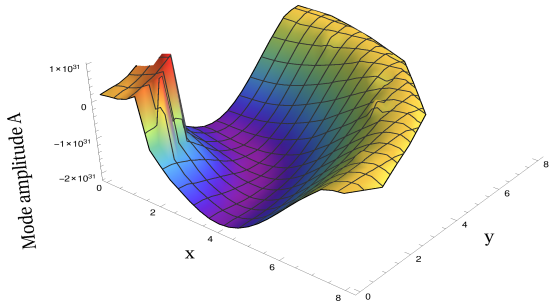

(c) p-mode, Frequency: 4110 Hz, xy-plane

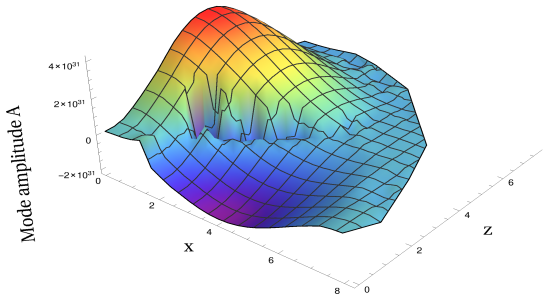

(d) p-mode, Frequency: 4110 Hz, xz-plane

Figure 4.17: Pressure eigenfunctions of the dominant modes of oscillation that appear during the study of the BU0 equilibrium model. The evolution took place under the Cowling approximation with an $l = 2$, $m = 0$ axisymmetric non radial initial perturbation.

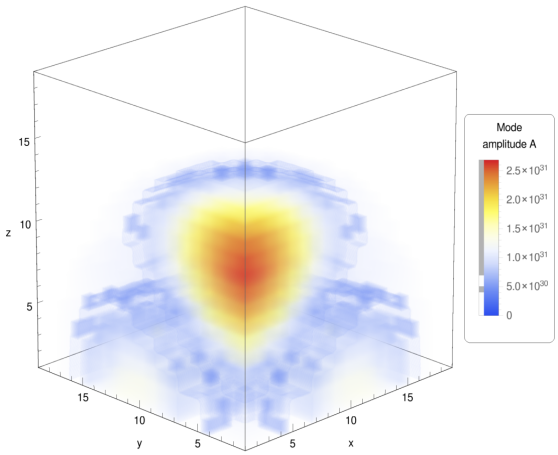

(a) f-mode, Frequency: 1894 Hz

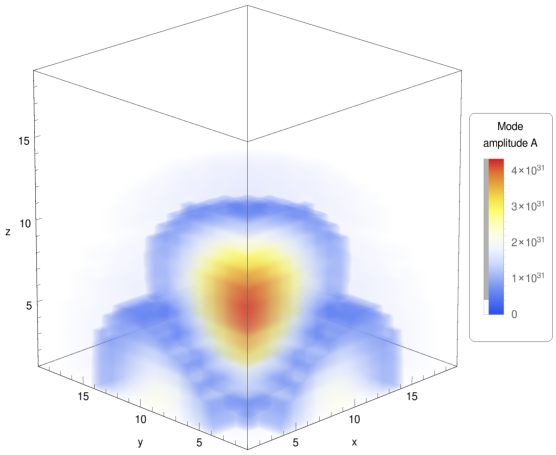

(b) p-mode, Frequency: 4110 Hz

Figure 4.18: Pressure eigenfunctions of the dominant modes of oscillation that appear during the study of the BU0 equilibrium model. The evolution took place under the Cowling approximation with an $l = 2$, $m = 0$ radial initial perturbation.

B. Oscillations of a rapidly rotating neutron star

Following again the logic of [10] for a second accuracy test we turned our attention to the study of an equilibrium model rotating close to the Kepler limit. For this task we studied the rapidly rotating BU7 model. The tests applied and the post processing analysis are identical thus there is no reason to go through the same explanation again. The most visible differences can be seen during the study of the eigenfunctions of the modes under study. As one can see in figures 4.19 and 4.20 the plots with the same procedure as before are not as clear as the equivalent ones for the non rotating case.

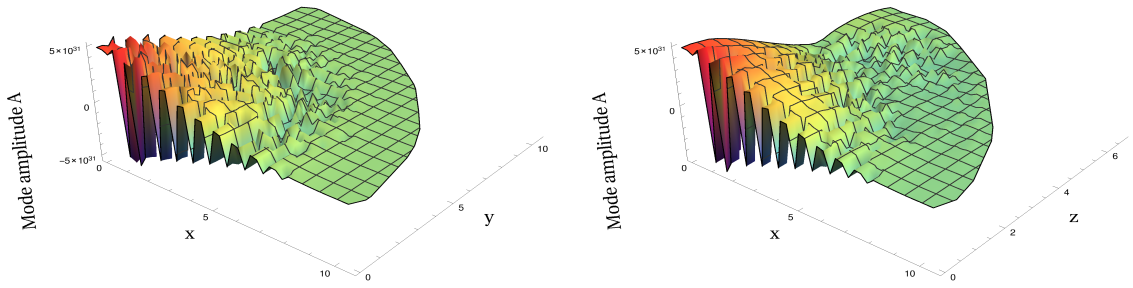

(a) f-mode, Frequency: 2435 Hz, xy-plane (b) p-mode, Frequency: 2435 Hz, xz-plane

Figure 4.19: Pressure eigenfunctions of the dominant modes of oscillation that appear during the study of the BU7 equilibrium model. The evolution took place under the Cowling approximation with an $l = 0$, $m = 0$ radial initial perturbation.

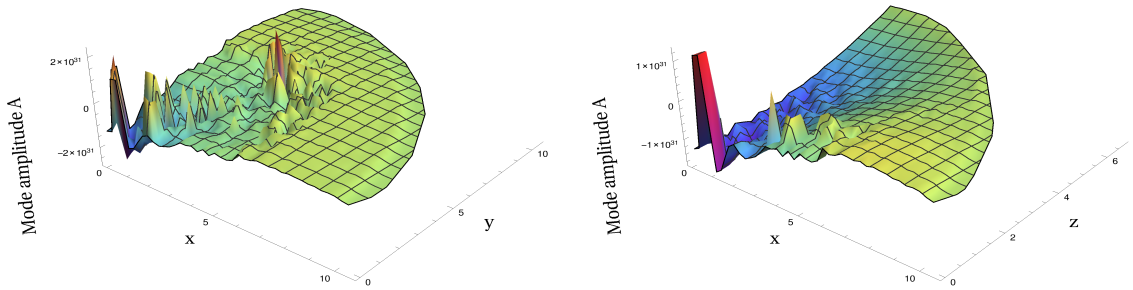

(a) f-mode, Frequency: 1690 Hz, xy-plane (b) p-mode, Frequency: 1690 Hz, xz-plane

Figure 4.20: Pressure eigenfunctions of the dominant modes of oscillation that appear during the study of the BU7 equilibrium model. The evolution took place under the Cowling approximation with an $l = 2$, $m = 0$ axisymmetric non radial initial perturbation.

In this context worthy of mentioning is that the our code is set up to export data in the Eulerian and not the Lagrangian frame of reference, but given that the modes of oscillation under study in this test are symmetric around the axis of rotation this cannot be the problem. Most probably the issue is the additional numerical complexity when rotation is present on top of the fact that we study axisymmetric configurations in a Cartesian grid.

Again, after studying the evolution of the rapidly rotating equilibrium BU7 model both for an $l = 0$, $m = 0$ radial initial perturbation and an $l = 2$, $m = 0$ axisymmetric non radial initial perturbation all the results that we got are very close to the ones that exist in the literature for the same models [8,9,10]. All the results from the first two tests are summarized in table 4.2.

Table 4.2: Collective results for tests A and B.

Model - Approximation-Mode	Literature results (Hz)	Maya code results (Hz)
BU0 - Cowling - Radial	$2694 - 2706$	2706
BU0 - Cowling - Non radial	$1884 - 1890$	1896
BU0 - Full GR - Radial	$1458 - 1465$	1434
BU0 - Full GR - Non radial	$1586 - 1601$	1563
BU7 - Cowling - Radial	$2456 - 2491$	2440
BU7 - Cowling - Non radial	$1703 - 1708$	1694
BU7 - Full GR - Radial	$1204 - 1207$	1191
BU7 - Full GR - Non radial	$1694 - 1720$	1690

C. Non axisymmetric oscillations of rapidly rotating neutron stars

Since our main objective is the investigation of the CFS instability in rapidly rotating neutron stars, we decided as our last accuracy test, to try and reproduce the main results of [10]. For this study we are going to consider the S and C series of equilibrium models. The characteristics of these models can be seen in tables 4.3 and 4.4. The higher or lower the value of the polytropic constant K in the polytropic equation describing a model, the stiffer or softer respectively we consider the model to be.

For the purpose of studying scenarios that could lead to the CFS instability, the initial

perturbation that we apply is a non radial, non axisymmetric perturbation described by (4.8)

$$\delta\rho = A \cdot \rho_c \cdot sin(\frac{\pi \cdot r}{r_s}) \cdot (1 - (\frac{z}{r})^2) \cdot cos(2 \cdot cos^{-1}(\frac{x}{\sqrt{x^2+y^2}})) \tag{4.8}$$

The perturbed rest mass density profiles for this case can be seen in figure 4.21 below.

Table 4.3: Equilibrium properties of the initial models as described by a polytropic EOS $p = K\rho_0^\Gamma$ where $\Gamma = 2$, $K = 100$. The entries are the same as in table 4.1.

Models	$\rho_c \times 10^3$	$M(M_\odot)$	$r_e(M_\odot)$	r_p/r_e	$T/\|W\|$	Ω/Ω_k
S0	2.628	1.6287	8.01291	1.0000	0.00	0.000
S1	2.628	1.6801	8.33261	0.9160	0.02	0.380
S2	2.628	1.7367	8.72215	0.8356	0.04	0.552
S3	2.628	1.7995	9.24599	0.7487	0.06	0.704
S4	2.628	1.8700	10.2131	0.6393	0.08	0.8.94

Table 4.4: Equilibrium properties of the initial models as described by a polytropic EOS $p = K\rho_0^\Gamma$ where $\Gamma = 2.5$, $K = 1000$. The entries are the same as in table 4.1.

Models	$\rho_c \times 10^3$	$M(M_\odot)$	$r_e(M_\odot)$	r_p/r_e	$T/\|W\|$	Ω/Ω_k
C0	5.0	1.2849	5.18143	1.0000	0.00	0.000
C1	5.0	1.3598	5.48084	0.8699	0.04	0.472
C2	5.0	1.4499	5.87314	0.7467	0.08	0.686

As we mentioned already, since we are evolving our configurations in the Eulerian frame, figuring out the nature of the non axisymmetric modes that we observe is very difficult through studying their eigenfunctions. Unless of course we study non rotating configurations. Luckily the modes that we are interested in have some characteristics that can help us. First of all, as we mentioned already, we assume that all the perturbed quantities have a sinusoidal dependence in the coordinates t and ϕ (azimuthal angle)

$$\delta\rho = \delta\rho(r,\theta) \cdot e^{i\cdot\omega\cdot t} \cdot e^{i\cdot m\cdot\phi} \tag{4.9}$$

Also we know that the $l = |m| = 2$ f-mode frequencies are degenerate in the non rotating configurations, but for the rotating cases they encounter rotational splitting. So what we can

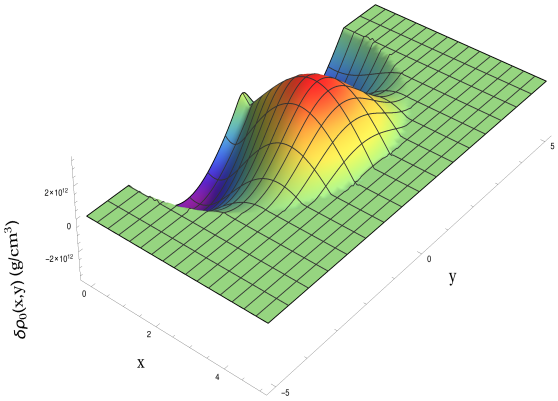

(a) xy - plane

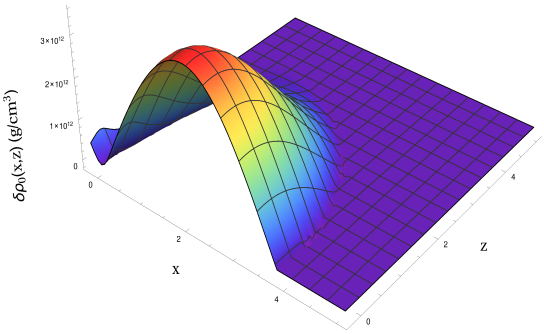

(b) xz - plane

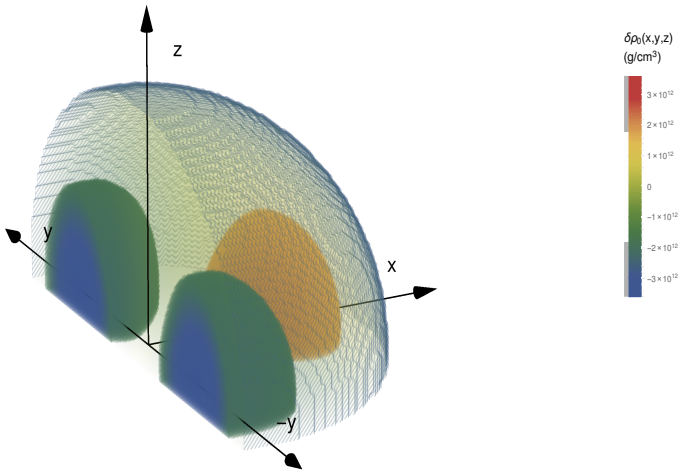

(c) Full configuration.

Figure 4.21: Initial perturbation profiles on the rest mass density of the spherically symmetric C0 equilibrium model for the $l = 2$, $m = 2$ non axisymmetric non radial perturbation.

do is for each one of the series that we want to study, to locate the initial degenerate mode through studying the eigenfunctions of the dominant frequencies in the non rotating cases and then move on to the rotating stars, utilizing the techniques described in [10]. More specifically, for every time iteration that we export data, we interpolate the hydrodynamical

quantities on the xy equatorial plane and then calculate the integral:

$$\delta Q_{c,t_i} = \frac{1}{2 \cdot \pi} \int_0^{2 \cdot \pi} \delta q(t_i) \cdot e^{i \cdot m \cdot \phi} d\phi \qquad m = \pm 2 \tag{4.10}$$

where c refers to a circle of some pre-decided radius. Finally we export the frequencies that we need by fast Fourier transforming the time series $\left\{\delta Q_c\right\}_t$. So basically what we do is using the Y_2^m spherical harmonics to decompose our hydrodynamical quantities on the equatorial plane. Finally for the counter-rotating modes of oscillation that appear to have negative frequencies, and thus we are not able to detect them with the above method, we form the following integral:

$$\delta Q_{c,t_i} = \frac{1}{2 \cdot \pi} \int_0^{2 \cdot \pi} \delta q(t_i) \cdot e^{i \cdot m \cdot (\phi + \phi_0)} d\phi \qquad m = \pm 2 \tag{4.11}$$

Where Ω is the angular frequency of the rotation of our configuration. This allows us to shift the Fourier transform by the frequency Ω towards the positive or negative frequencies. Examples of this kind of analysis can be seen in figures 4.22, 4.23 and 4.24. Also the final results of our tests can be seen in table 5.

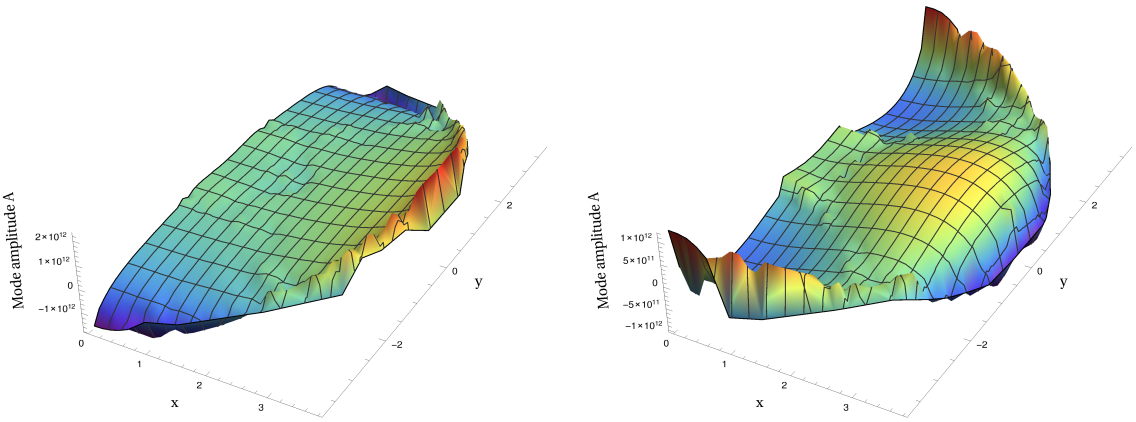

(a) f-mode, Frequency: 3787 Hz (b) p-mode, Frequency: 9257 Hz

Figure 4.22: Projection on the xy-plane of the eigenfunctions of the rest mass density of the two dominant frequencies that appear during the study of the C0 equilibrium model. The evolution took place under the Cowling approximation with an l=2, m=2 non axisymmetric non radial initial perturbation.

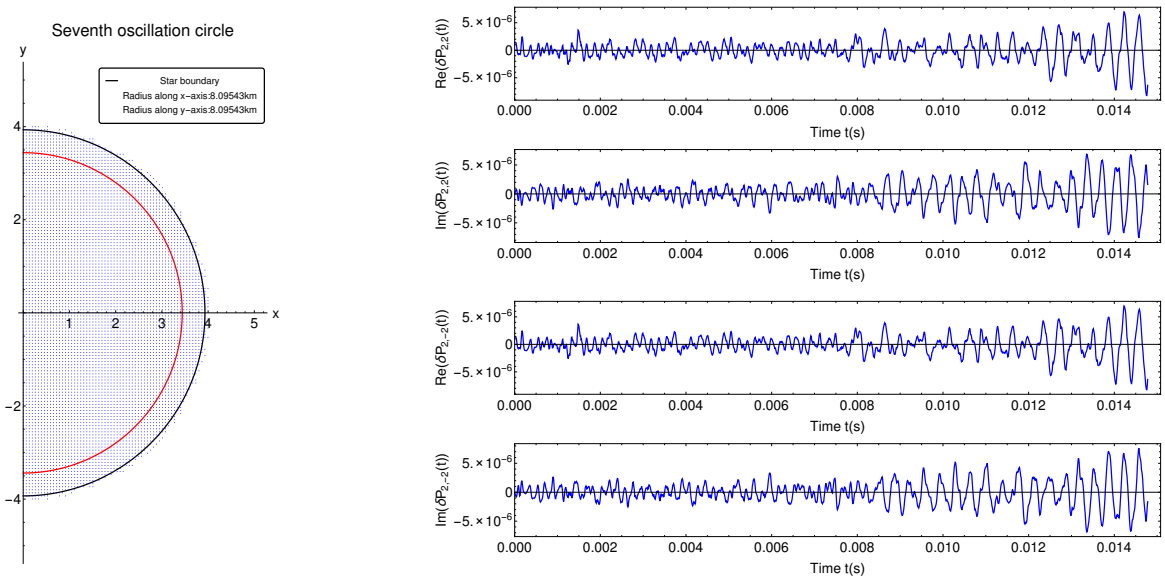

Figure 4.23: Time evolution of δQ_c for rest mass density for the C1 equilibrium model. The evolution took place under the Cowling approximation with an $l = 2, |m| = 2$ non radial initial perturbation.

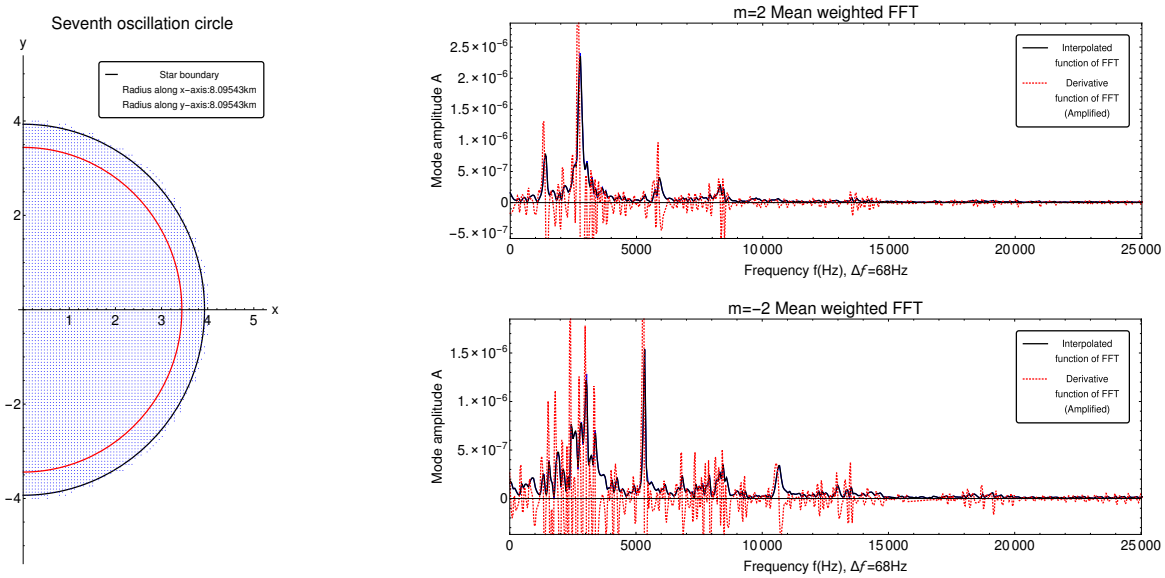

Figure 4.24: Fast Fourier transforms corresponding to the time series depicted in figure 4.23.

Figure 4.23 shows the time evolution of the imaginary and real parts of the quantity δQ_c for the case of the rest mass density for the C1 equilibrium model. The non rotating member of the C-series presents an f-mode characterised by a frequency equal to 3787 Hz. Moving to the rotating C1 member we can now observe, as we can see in figure 4.24, the

splitting of this mode to two different modes. An $l = 2, m = 2$ f-mode with frequency 1388 Hz and an $l = 2, m = -2$ f-mode with frequency 5330 Hz.

Table 4.5: Collective results for test C.

Model - Approximation	Literature results (Hz)	Maya code results (Hz)
S0 - Cowling	$m = 2 : 2484 \;\; m = -2 : 2484$	$m = 2 : 2510 \;\; m = -2 : 2510$
S0 - Full GR	$m = 2 : 2162 \;\; m = -2 : 2162$	$m = 2 : 2200 \;\; m = -2 : 2200$
S1 - Cowling	$m = 2 : 1414 \;\; m = -2 : 3221$	$m = 2 : 1419 \;\; m = -2 : 3205$
S1 - Full GR	$m = 2 : 1130 \;\; m = -2 : 2888$	$m = 2 : 1150 \;\; m = -2 : 2935$
S2 - Cowling	$m = 2 : 872 \;\; m = -2 : 3398$	$m = 2 : 880 \;\; m = -2 : 3390$
S2 - Full GR	$m = 2 : 630 \;\; m = -2 : 3056$	$m = 2 : 630 \;\; m = -2 : 3120$
S3 - Cowling	$m = 2 : 408 \;\; m = -2 : 3458$	$m = 2 : 406 \;\; m = -2 : 3459$
S3 - Full GR	$m = 2 : 215 \;\; m = -2 : 3134$	$m = 2 : 212 \;\; m = -2 : 3255$
S4 - Cowling	$m = 2 : -117 \;\; m = -2 : 3426$	$m = 2 : -120 \;\; m = -2 : 3463$
S4 - Full GR	$m = 2 : -240 \;\; m = -2 : 3154$	$m = 2 : -238 \;\; m = -2 : 3230$
C0 - Cowling	$m = 2 : 3800 \;\; m = -2 : 3800$	$m = 2 : 3781 \;\; m = -2 : 3781$
C0 - Full GR	$m = 2 : 2527 \;\; m = -2 : 2527$	$m = 2 : 3313 \;\; m = -2 : 3313$
C1 - Cowling	$m = 2 : 1359 \;\; m = -2 : 5314$	$m = 2 : 1388 \;\; m = -2 : 5330$
C1 - Full GR	$m = 2 : 698 \;\; m = -2 : 3668$	$m = 2 : 926 \;\; m = -2 : 4868$
C2 - Cowling	$m = 2 : 144 \;\; m = -2 : 5598$	$m = 2 : 137 \;\; m = -2 : 5620$
C2 - Full GR	$m = 2 : -170 \;\; m = -2 : 3894$	$m = 2 : -248 \;\; m = -2 : 5209$

As can be seen, our results are very close to the ones found in [10], for the tests applied on the S series, but that is not true for the C series in the full GR case. For this case we managed to reproduce the available results only in the Cowling approximation. Since the only results out of a three-dimensional code for the C-Series in the full GR case come from [10] and since the results that we compared with for the C-Series in the cowling approximation come from an independent code we can not really be sure about which code is the problematic one.

All the results form the simulations described above can be found analytically at [23].

CHAPTER 5

RESULTS 2: GRAVITATIONAL WAVE ASTEROSEISMOLOGY FROM ROTATING NEUTRON STARS

After reaching a point where our code seems to be able to pass all the necessary tests to be considered stable and accurate, we are in a position to move towards the creation of empirical relations that can later be used for asteroseismology on rapidly rotating neutron stars. The last piece of puzzle needed at this point is to find a reliable way to calculate the damping times of the modes of oscillations that we are interested in.

5.1 Calculation of damping times for non rotating neutron stars

5.1.1 Application of the time independent quadrupole formula

As we mentioned in chapter 2.5 the damping time, due to gravitational wave emission, of a fluid mode of oscillation that obeys conditions (2.8) and (2.29) can be calculated by:

$$\frac{1}{\tau_{GR}} = \frac{(\omega + m\Omega)}{2E} \sum_{l=l_{min}}^{\infty} N_l \omega^{2l+1} \delta D_l^m \delta D_l^{*m} \tag{5.1}$$

Quantity E is described by:

$$E = K + V = \frac{1}{2}\int \Big[\rho_{init}\delta u^a \delta u_a^*\Big] d^3x + \frac{1}{2}\int \Big[\frac{1}{2}(\delta\rho(\frac{\delta p}{\rho_{init}} - \delta\Phi)^* + \delta\rho^*(\frac{\delta p}{\rho_{init}} - \delta\Phi))\Big] d^3x \tag{5.2}$$

Where ρ_{init} refers to the rest mass density of the unperturbed neutron star model, while K and V refer to the excess kinetic and potential energy in the star due to the deviation from the equilibrium state. Since this deviation is caused by the mode of oscillation under study we can consider E to be the energy characterizing this mode. Also quantity D_l^m is

described by:

$$D_l^m = \int \delta\rho r^l Y_l^{*m} dx^3 \tag{5.3}$$

Using the same logic as before we can consider it to be the mass multipole of the mode under study. Finally as mentioned before N_l is a constant described by:

$$N_l = \frac{4\pi G}{c^{2l+1}} \frac{(l+1)(l+2)}{l(l-1)[(2l+1)!!]^2} \tag{5.4}$$

As described in [4], this approach refers to Newtonian stellar models. Given that we are working with neutron stars we need to take in account the fact that the space-time geometry is not flat. In other words, while calculating the above quantities, we need to take in account how the spatial metric components vary within the neutron star. This approach, using a Newtonian model but calculating its constituent parts in General Relativity, is what is known as working in the post-Newtonian regime. In this case we have that:

$$\begin{aligned} \delta u^a \delta u_a^* = \sum_i \sum_j \gamma_{ij} \delta u^i \delta u^{j*} = \gamma_{xx}|\delta u^x|^2 + \gamma_{yy}|\delta u^y|^2 + \gamma_{zz}|\delta u^z|^2 \\ +2\gamma_{xy} Re(\delta u^x (\delta u^y)^*) + 2\gamma_{xz} Re(\delta u^x (\delta u^z)^*) + 2\gamma_{yz} Re(\delta u^y (\delta u^z)^*) \end{aligned} \tag{5.5}$$

Where we used the fact that for every complex number z it is true that $z + z^* = 2Re(z)$ and $z \cdot z^* = |z|^2$. Also the volume element used for the integrals in (5.2) and (5.3) is given by:

$$d^3x = \sqrt{\gamma} dx dy dz \tag{5.6}$$

with γ being the determinant of the spatial metric. Finally when it comes to the mass multipole, the distance r is calculated by:

$$r = \int_{t=0}^{t=1} \sqrt{\gamma_{ij}(x(t), y(t), z(t)) \frac{dx^i(t)}{dt} \frac{dx^j(t)}{dt}} dt \tag{5.7}$$

with $\bar{r}(t) = x(t)\hat{i} + y(t)\hat{j} + z(t)\hat{k}$ being the parametrized straight line from the center

of the star to the point under study. The first thing that strikes as strange with equations (5.2) and (5.3) is the inclusion of complex numbers in them. As it has become clear at this point the calculation of the energy of a mode of oscillation requires from us to know the deviation from equilibrium of the rest mass density, pressure and spatial velocities for every constituent element of our star, that is caused by this specific mode. In other words, for every grid point inside the star we need the amplitude of oscillation of the quantities δp_ω, $\delta \rho_\omega$, and δu^i_ω, where ω is the oscillation frequency of this mode. To calculate the amplitude of this oscillations and form the eigenfunction of this mode we apply again a fast Fourier transform on all the time series $\left\{\delta p(t)\right\}_k$, $\left\{\delta \rho(t)\right\}_k$ and $\left\{\delta u(t)^i\right\}_k$ extracted from every grid point k inside the star. For this procedure we use again the algorithm (4.7). So in the end, for every gird point k we have in our possession a set of complex numbers $\left\{\delta p_\omega, \delta \rho_\omega, \delta u^x_\omega, u^y_\omega, u^z_\omega\right\}_k$ that include the information of both the amplitude and the phase of oscillation of these specific quantities that the mode of interest causes to this specific point. Figure (5.1) shows two different versions of the pressure eigenfunction of the non radial non axisymmetric $f-mode$ of oscillation of the BU0 model evolved in the Cowling approximation. The lower part portrays the absolute value of the amplitude of oscillation at every point while the upper part portrays the same amplitude multiplied by the sign of the corresponding phase of oscillation. In other words, including the complex eigenfunctions in the calculation of the energy and the mass multipole of every mode, is necessary if we wish to take in account the fact that different parts inside the star possess negative or positive energy due to this mode.

One last approximation that we are going to use is to set the gravitational potential perturbation $\delta\Phi$ equal to zero. This is accurate only for the case of the Cowling approximation. For the full general relativity cases this approximation makes sense only when we expect the biggest contribution to be provided by the perturbation of the fluid inside the star. Following the process we described above we studied the non axisymmetric and non radial $l = |m| = 2$ $f-mode$ of oscillation for the non rotating BU0 model both in the

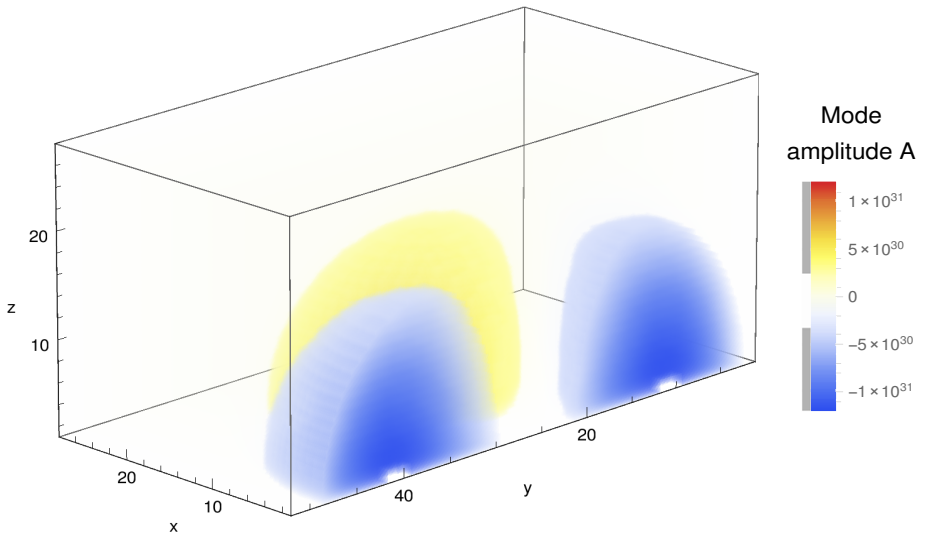

(a) Magnitude of oscillations multiplied by their phase sign.

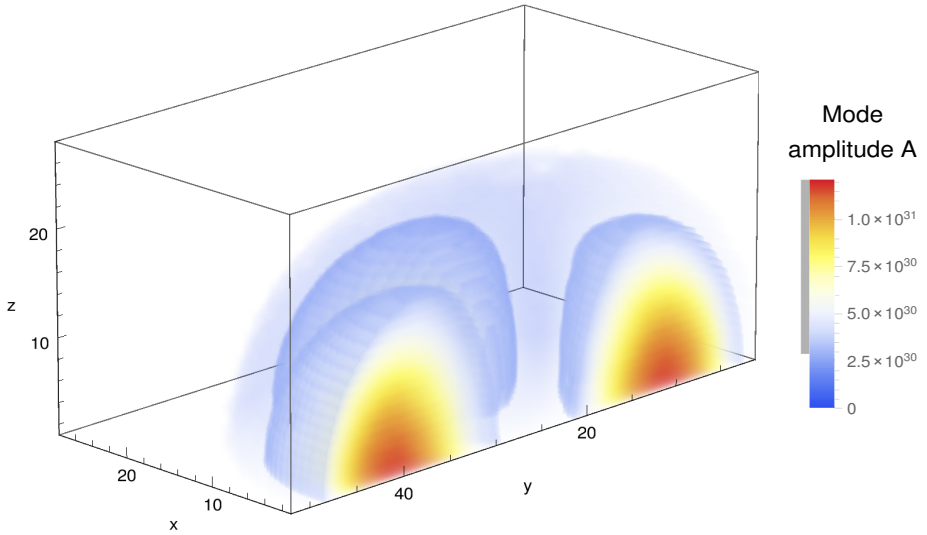

(b) Magnitude of oscillations.

Figure 5.1: Pressure eigenfunctions of the dominant f-mode of oscillation that appear during the study of the BU0 equilibrium model. The evolution took place under the Cowling assumption with an $l = 2$, $m = 2$ non axisymmetric non radial initial perturbation.

Cowling and the Full general relativistic case. In the Cowling approximation we found the $f - mode$ to be characterized by a frequency equal to $1893.71Hz$ with a damping time equal to $\tau = 0.0889316$ seconds. The equivalent values for the general relativistic case are for the frequency $1589.7Hz$ and the damping time 0.279084 seconds. These values are accurate according to the existing literature.

5.1.2 Application of the time dependent quadrupole formula

A rather interesting insight to the use of the quadrupole formula for the calculation of damping times is given by studying the quantity τ_{GR} it self as a function of time. The procedure for this approach is the following. Again for every grid point k inside the star we extract the discrete time series of the perturbed hydrodynamical quantities $\left\{\delta p(t_j)\right\}_k$, $\left\{\delta \rho(t_j)\right\}_k$ and $\left\{\delta u^i(t_j)\right\}_k$ with j in this case referring to the time iteration. The next step is to apply a band pass filter on every single one of these time series that eliminates every other frequency besides the ones belonging in an appropriate set $\Delta f = (\omega - \Delta\omega, \omega + \Delta\omega)$ where ω is again the frequency of the mode under study. The result of this procedure can be seen in figure 5.2. The upper part shows the time evolution of the perturbation of pressure of one of the regions of the xy-plane of BU0 model while the lower part shows how the same time series behave after being filtered around the frequency of the $f-mode$. Ideally, after applying the band pass filtered, the resulting time series now only include information about this specific $f-mode$.

After obtaining the filtered time series $\left\{\delta p(t_j)\right\}_{k,\omega}$, $\left\{\delta \rho(t_j)\right\}_{k,\omega}$ and $\left\{\delta u(t_j)^i\right\}_{k,\omega}$ we are in a position to calculate for every time iteration t_j and every grid point the integrands seen in formulas (5.2), (5.3). Finally by summing up these quantities over all the grid points inside the star at every time iteration, we can obtain the discrete time series $\left\{E(t_j)\right\}_\omega$ and $\left\{D_l^m(t_j)\right\}_\omega$ which we can ultimately insert in formula (5.1) to get the time series of the damping time of the $f-mode$ under study:

$$\left\{\tau_{GR}(t_j)\right\}_\omega = \frac{1}{\frac{(\omega+m\Omega)}{2\left\{E(t_j)\right\}_\omega}\sum_{l=l_{min}}^{\infty} N_l \omega^{2l+1}\left\{|\delta D_l^m(t_j)|^2\right\}_\omega} \tag{5.8}$$

The result of this approach can be seen in figure (5.3).

The yellow and red lines present in this figure serve as reference for the correct value of the damping time of the $f-mode$ and twice that same value correspondingly. What becomes immediately apparent is that τ seems to periodically touch a lower limit between

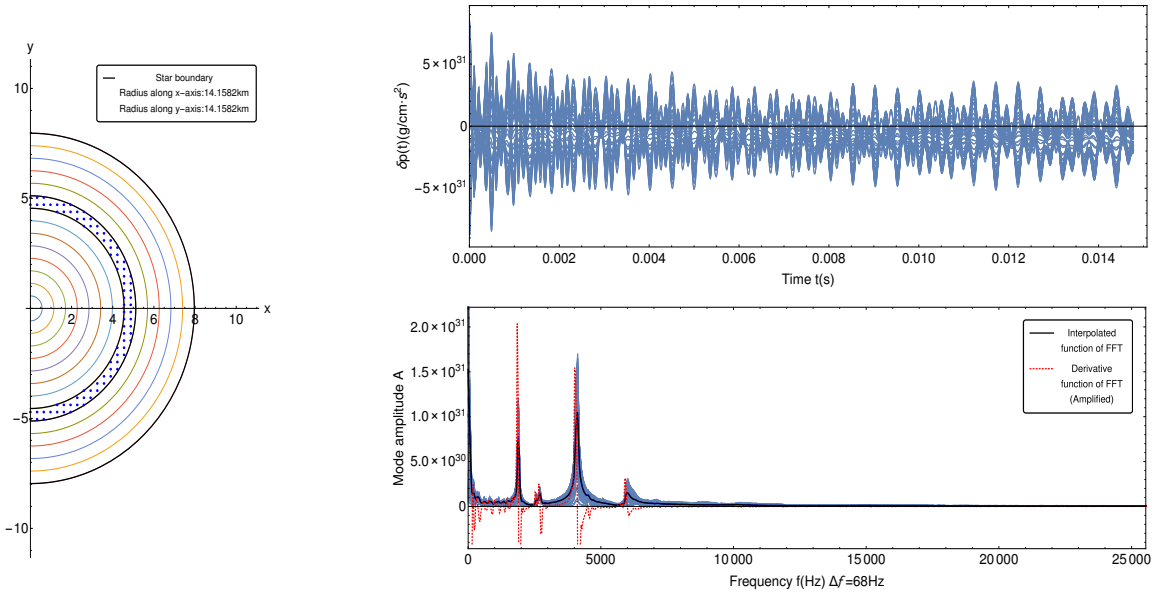

(a) Unfiltered time series.

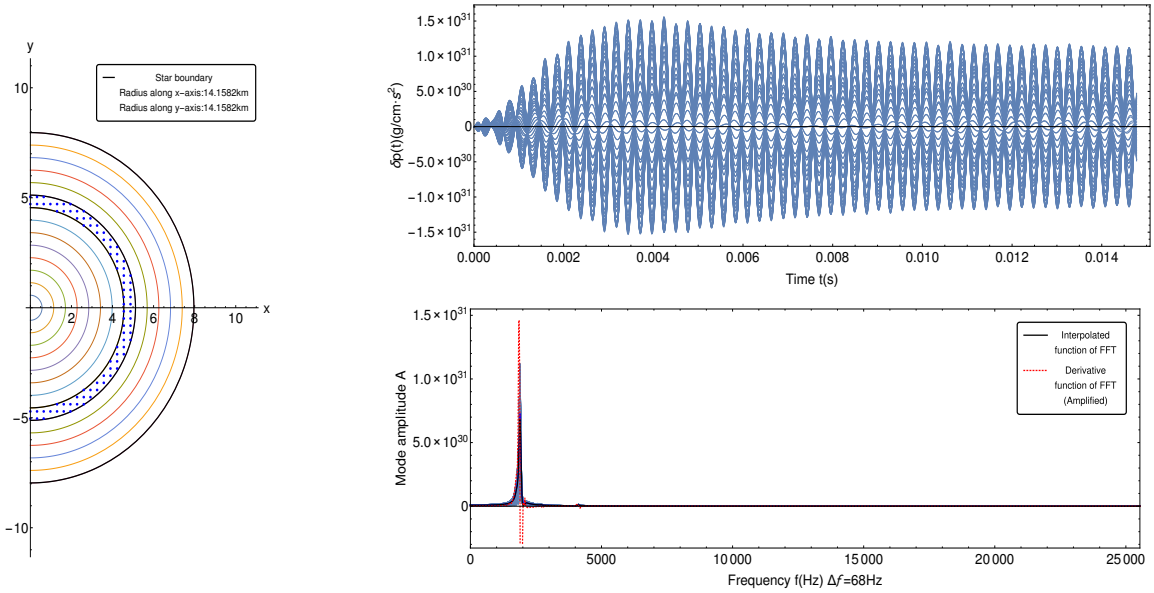

(b) Time series filtered around $\omega = 1893.71Hz$.

Figure 5.2: Time evolution of pressure perturbation on the xy-plane for the BU0 equilibrium model. The evolution took place under the Cowling approximation with an $l = 2$, $m = 2$ non axisymmetric non radial initial perturbation on the rest mass density.

the values of $\tau = 0.0889$ seconds and $\tau = 2 \cdot 0.0889$ seconds in between really sharp periodic jumps. These periodic jumps are characterized by values that vary between $\tau = 1000$ seconds and $\tau = 100000$ seconds. To understand this behaviour it is useful to study the filtered pressure perturbation profiles during the extreme cases of τ moving from a min-

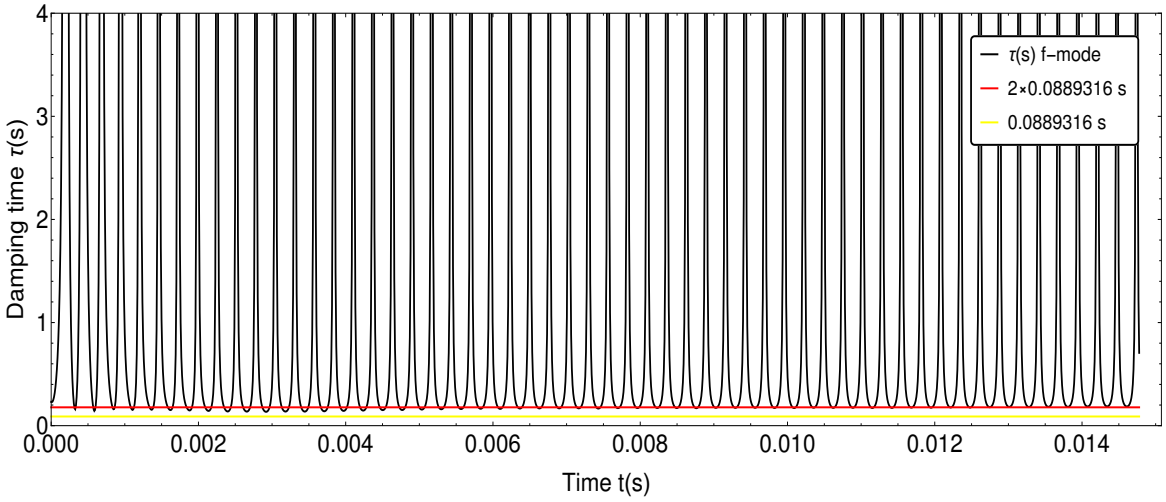

Figure 5.3: Time evolution of the damping of the f-mode of oscillation of the BU0 equilibrium model. The evolution took place in the Cowling approximation with an $l = 2$, $m = 2$ non axisymmetric non radial initial perturbation on the rest mass density.

imum point to a sharp jump to a minimum point again. These snapshots can be seen in figure (5.4). Sub-figures (5.4)-(a),-(b),-(e),-(f) correspond to the case where τ gets minimized while sub-figures (5.4)-(c),-(d), correspond to the case where τ gets maximized. These figures show that when the filtered pressure perturbations, and correspondingly the filtered rest mass density perturbations calculated through $\rho = (\frac{p}{K})^{\frac{1}{\Gamma}}$, reach a high amplitude point, then τ approaches it's correct value. On the other hand when these same quantities go through the equilibrium point of oscillation, τ moves towards infinity. The explanation of this behaviour resides in formula (5.8) and the fact that the biggest contribution, by at least a couple of orders of magnitude, to the energy $E(t)$ is given the by the potential energy part and thus the rest mass density and pressure perturbations. So when the filtered perturbations go through the equilibrium point, the squared mass multipole of the $f - mode$ goes to zero faster than its' energy and thus τ goes to infinity. Finally the reason why τ never acquires the value calculated by the time independent use of the quadrupole formula probably has to do with the fact that our band pass filter does not totally eliminate all other frequencies from the perturbed time series.

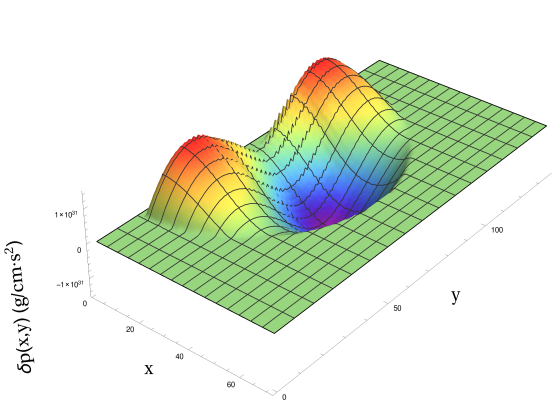

(a) xy - plane, t = 3.75813 ms

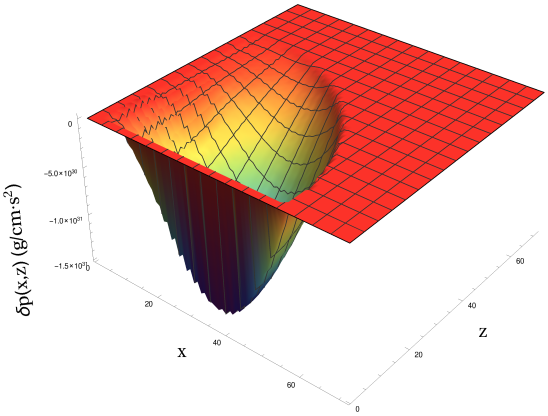

(b) xz - plane, t = 3.75813 ms

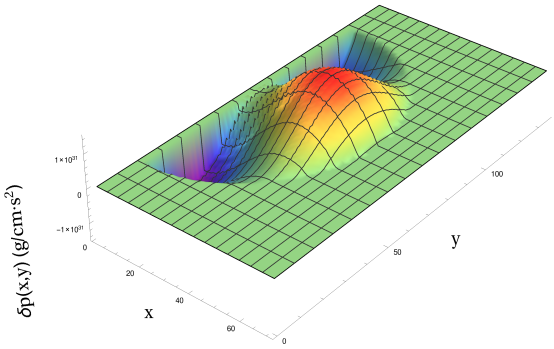

(c) xy - plane, t = 3.91884 ms

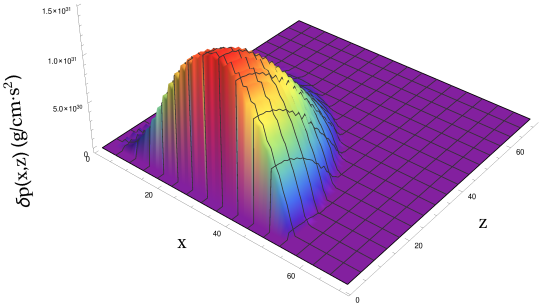

(d) xz - plane, t = 3.91884 ms

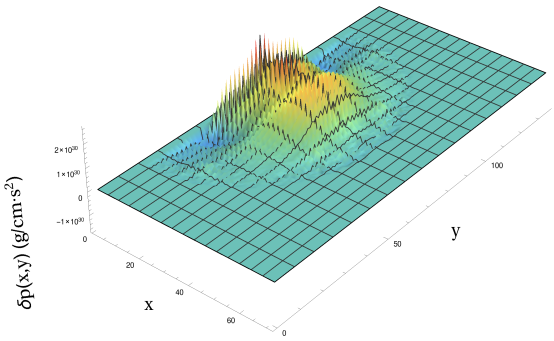

(e) xy - plane, t = 4.09191 ms

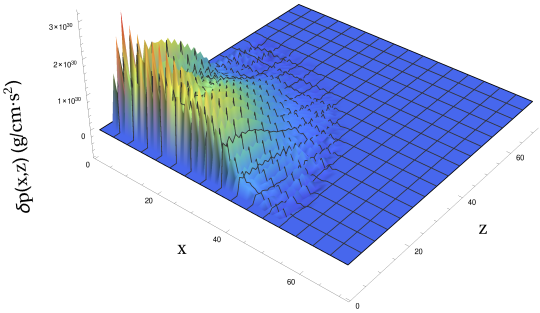

(f) xz - plane, t = 4.09191 ms

Figure 5.4: Snapshots of the time evolution of the filtered pressure from the BU0 model evolved in the Cowling approximation with an $l = 2$, $m = 2$ non axisymmetric non radial initial perturbation on the rest mass density. The pressure is filtered around the frequency of the f-mode of oscillation.

5.1.3 Calculation of damping times directly from the gravitational wave signal

As mentioned in chapter 2.2 small metric perturbations can cause motion of particles in space-time. This fact is the basis behind the gravitational wave detection achieved by detectors like LIGO. More specifically the laser interferometers of such detectors are able to detect the momentary stretching and compression of spatial distances when gravitational radiation passes through them. When a gravitational wave passes through earth the result is to cause distortions of the order of 10^{-21} meters. Although this is clearly extremely small, it can cause a big enough distortion to the 4 kilo-meter arms of a detector like LIGO that is able to trigger a clear detection.

If we consider the case of a localized source like a binary system of black holes or a single rotating neutron star then it is convenient to use spherical coordinates. Considering r to be the radial distance, ϕ the azimuthal angle and θ the polar angle then regarding the h_+ polarization we have that $h_+ = h_{\hat{\theta}\hat{\theta}} = -h_{\hat{\phi}\hat{\phi}}$ and regarding the $h_\times$ polarization we have $h_\times = h_{\hat{\theta}\hat{\phi}} = h_{\hat{\phi}\hat{\theta}}$, where $\hat{\theta}$ and $\hat{\phi}$ refer to components with respect to a local orthonormal system.

Going back to chapter two and more specifically to equation (2.3), we saw that it is possible to use the Riemann tensor for the purpose of measuring the second time derivative of h_+ and $h_\times$ thus the quantities $\ddot{h}_+$ and $\ddot{h}_\times$. This means that by studying the Riemann tensor in our simulations, we can acquire information about the second time derivatives of the strain polarizations. This is ideally done as far away from the source as it is computationally feasible so we can get as clean of a signal as it is possible. Finally in the field of computational relativity it is common to combine $\ddot{h}_+$ and $\ddot{h}_\times$ into a single complex quantity defined as $\Psi_4 = \ddot{h}_+ - i\ddot{h}_\times$.

Going back to the topic of calculating the damping times of the modes of oscillation that interest us, it would be extremely convenient to achieve this goal by directly studying the Ψ_4 quantity. Obviously such a procedure can only be possible for the full general relativistic simulations, since in the case of the Cowling approximation we keep the metric

components frozen. An example of such a study can be seen in figure 5.5 where we present the decomposition into the $l = 2, m = 2$ spin-weighted spherical harmonics with spin weight $s = 2$ of the Ψ_4 quantity. This is extracted from a distance of roughly 130 $M_\odot$ from the center of the BU0 model.

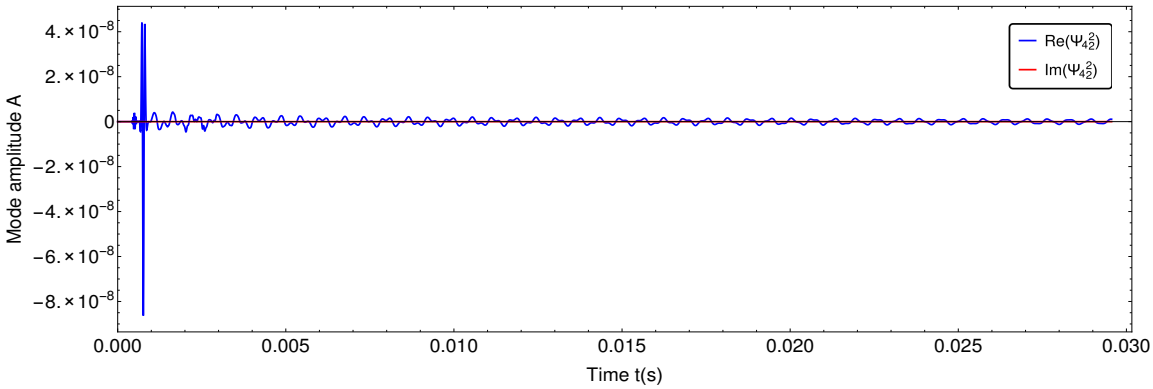

(a) Gravitational wave signal.

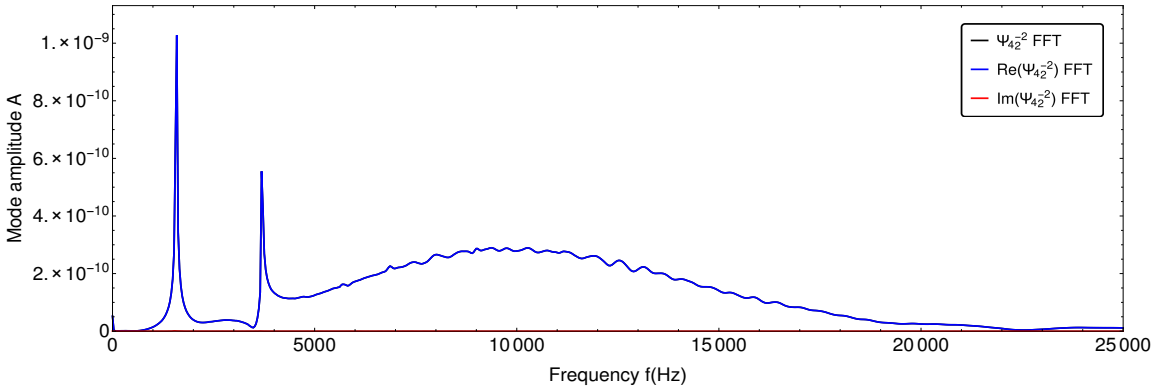

(b) Corresponding fast Fourier transform.

Figure 5.5: Decomposition into the $l = 2, m = 2$ spin-weighted spherical harmonics with spin weight $s = 2$ of the Ψ_4 quantity extracted from a distance of roughly 130 $M_\odot$ from the center of the star. The star under study is the BU0 model. The evolution took place in full general relativity with an $l = 2$, $m = 2$ non axisymmetric non radial initial perturbation on the rest mass density.

What becomes immediately apparent from figure 5.5 is the existence of a large amplitude oscillation observed at the beginning of the Ψ_4 decomposition time series which is characterized by a frequency of around 10 kHz. This is an example of a space-time w-mode. We also observe a smaller amplitude perturbation appearing earlier in the time series. We will discuss these modes in more detail later. For the time being we are interested in the

two other modes of oscillation observed. The first is characterized by a frequency equal to 1590 Hz and corresponds to the $l = 2, m = 2$ f-mode and the second by a frequency of 3699 Hz and corresponds to the $l = 2, m = 2$ p-mode of the BU0 model. The same exact frequencies were observed during the study of time evolution of the hydrodynamical perturbations inside the star. Wishing to achieve a direct calculation of the damping time of the f-mode we applied a band pass filter on the Ψ_4 decomposition and fitted the resulting time series with a sinusoidal function. This approach can be seen in figure 5.6.

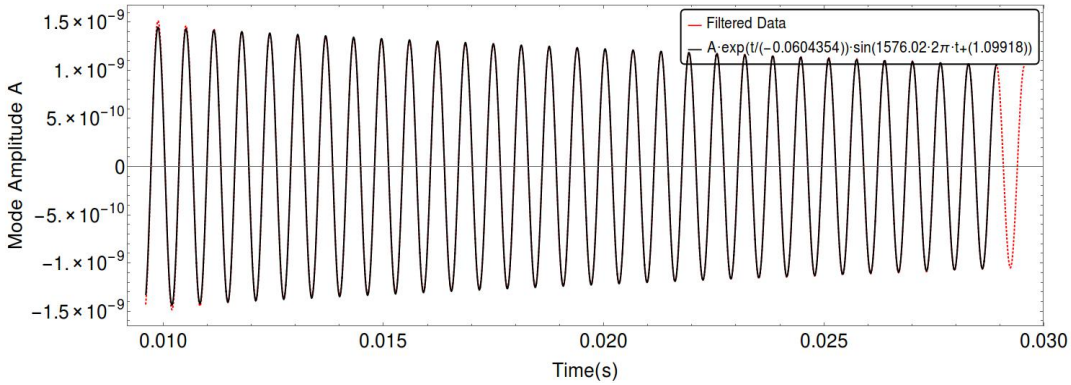

Figure 5.6: Fitting of the filtered $s = 2, l = 2, m = 2$ decomposition of the Ψ_4 quantity seen in figure 5.5.

The damping time obtained with this approach is equal to $\tau = 0.0604$ seconds which is at least four times smaller than the correct value obtained using the quadrupole formula. Given that the non rotating case is the simplest that can be studied it becomes apparent that this approach is not reliable when it comes to the code that we use. The main problem is most probably the artificial numerical viscosity used by our code which is there to secure the stability of our simulations. The exact same conclusion is reached when we study the damping times directly from the time evolution of the hydrodynamical quantities extracted from the interior of the star. On a more fundamental level, even if there was no numerical viscosity present, it would be very difficult to get accurate results using this approach due to the fact that the evolution time of our simulations is in-between 15 and 30 milliseconds while the damping times of the modes that interest us can get several orders of magnitude higher than that.

5.2 Calculation of damping times for rotating neutron stars

Moving forward to the study of damping times for the case of rotating neutron star configurations we have to discuss first the differences between observing a rotating system from the perspective of an inertial frame and a frame co-moving with the star. The main components included in the quadrupole formula used for the calculation of the damping time of some specific mode, are the frequency and the eigenfunction components that correspond to this mode. Both of these parts are different depending on the frame of reference that is utilized. An example of this fact can be seen in figure (5.6). In these cases we study the behaviour of the slowly rotating BU1 equilibrium model, and more specifically the time evolution of pressure extracted for points from the same region of the star, in the inertial and the co-moving frame correspondingly. What becomes apparent is that the frequencies of the observed modes are not the same. What happens in this case is that the $l = |m| = 2$ f- and p-modes change order of appearance. More specifically the frequencies of these modes that are characterized by $m > 0$ increase by $m\Omega$ while for the cases of $m < 0$ we see an decrease equal to $m\Omega$. For example the BU1 model evolved in the Cowling approximation presents an $l = 2, m = 2$ f-mode at $f_{Inert} = 1352.41$ Hz and an $l = 2, m = -2$ mode at $f_{Inert} = 2299.1$ Hz which in the co-moving frame assume the values $f_{Co} = 2098.09$ Hz and $f_{Co} = 1553.43$ Hz correspondingly. When it comes to the extraction of the eigenfucntions of the modes of interest from the two different frames, an example can be seen in figure (5.7). In this case the model under study is the slowly rotating BU2 equilibrium model and the evolution took place again under the Cowling approximation. The eigenfucntions under study correspond to the $l = 2, m = -2$ f-mode with frequencies $f_{Inert} = 2367.75$ Hz and $f_{Co} = 1355.93$. These two examples make apparent that we can't expect to get the same results for the damping times from the inertial and the co-moving frame.

A final issue that we need to take in account is the calculation of the spherical harmonics present in equation (5.3), and more specifically the calculation of the azimuthal angle θ and

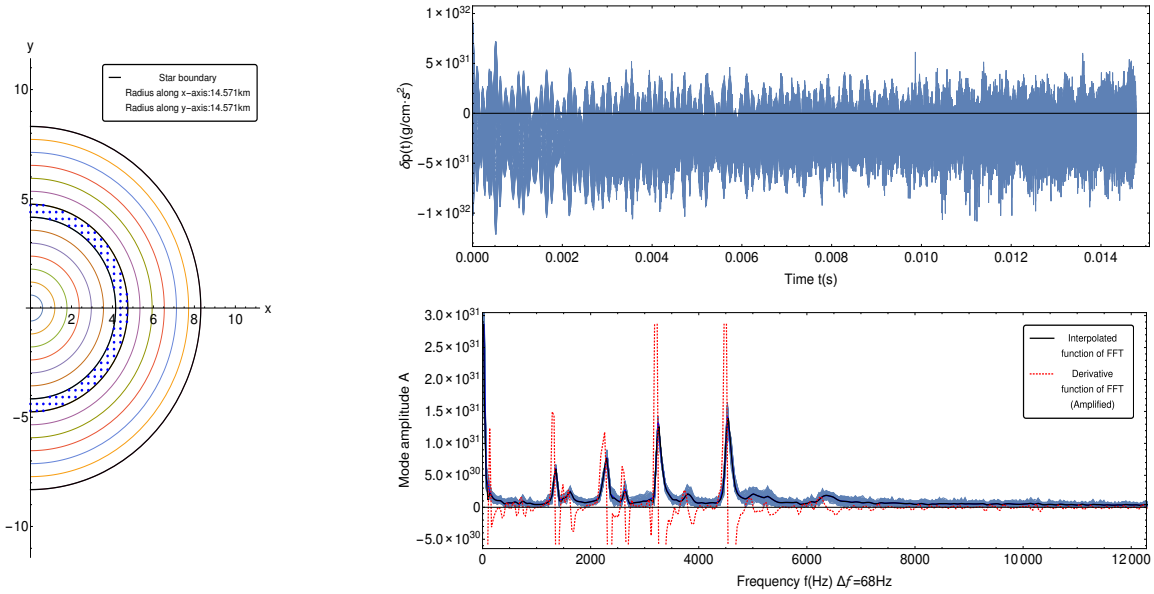

(a) Inertial frame of reference.

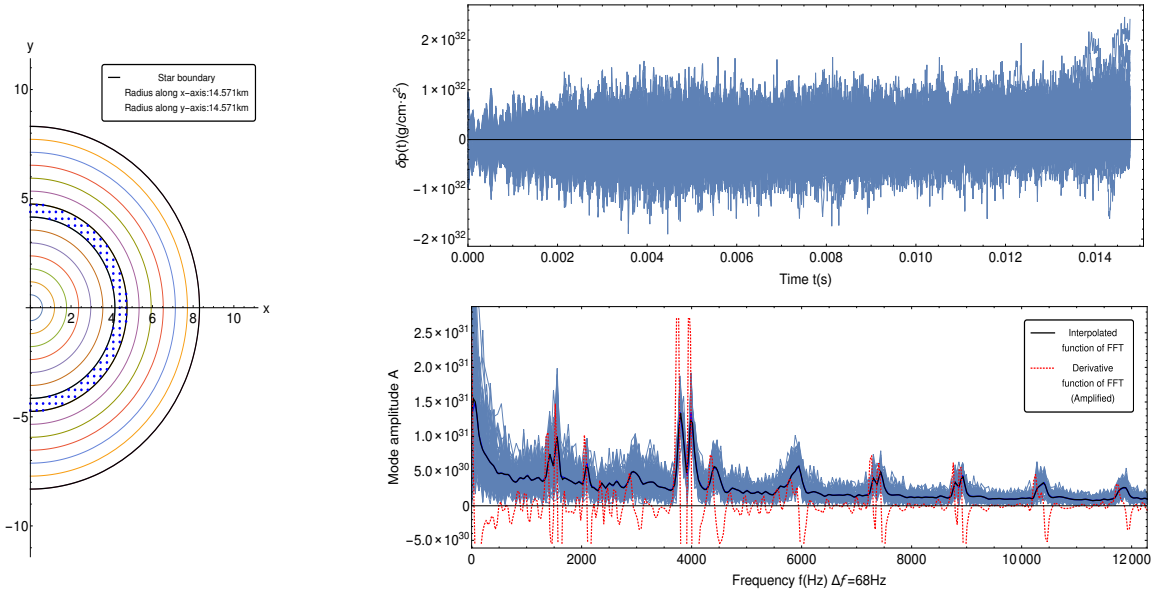

(b) Co-moving frame of reference.

Figure 5.7: Time evolution of pressure perturbation on the xy-plane for the BU1 equilibrium model. The evolution took place under the Cowling approximation with an $l = 2$, $m = 2$ non axisymmetric non radial initial perturbation on the rest mass density.

the polar angle ϕ present in:

$$Y_2^2(\theta, \phi) = \frac{1}{4}\sqrt{\frac{15}{2\pi}} e^{2i\phi} sin^2\theta \tag{5.9}$$

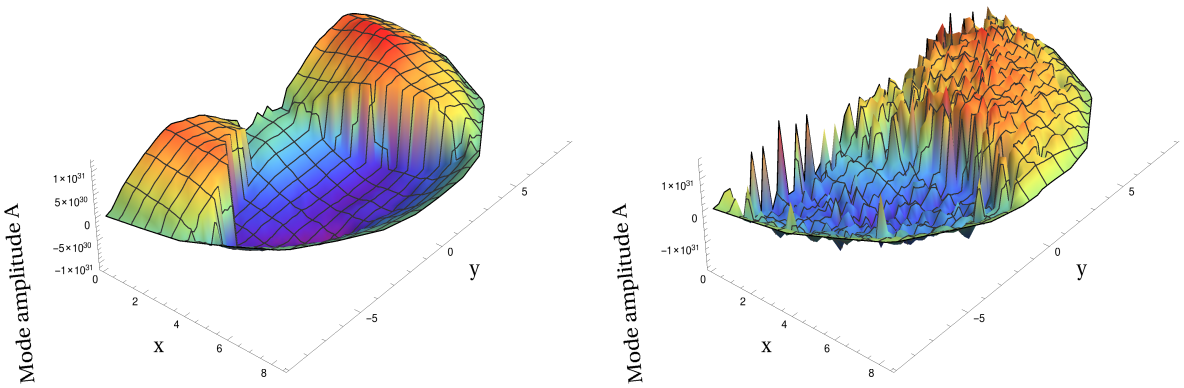

(a) Inertial frame of reference. (b) Co-moving frame of reference.

Figure 5.8: Pressure eigenfunctions of the $l = 2, m = -2$ mode of oscillation that appears during the study of the BU2 equilibrium model. The evolution took place under the Cowling approximation with an $l = 2$, $m = 2$ non axisymmetric non radial initial perturbation.

We consider an arbitrary point inside the star as seen in figure (5.9).

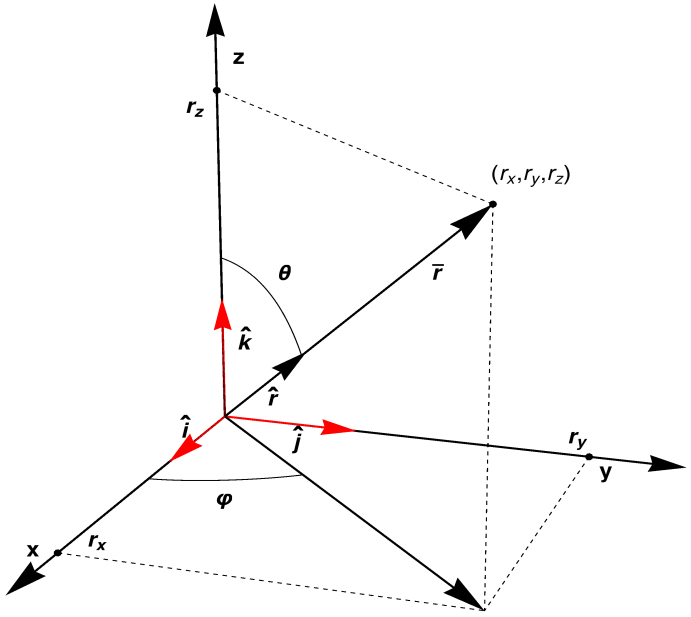

Figure 5.9: Euclidean polar and Cartesian coordinates of an arbitrary point inside a star.

In the case of the non rotating models we used the Euclidean definitions:

$$\phi = tan^{-1}(\frac{r_y}{r_x}) \tag{5.10}$$

and

$$\theta = cos^{-1}(\frac{r_z}{\sqrt{r_x^2 + r_y^2 + r_z^2}}) \tag{5.11}$$

Given that angles are ratios of distances, this works appropriately in the spherically symmetric non rotating cases, but when we move to a rotating case this spherical symmetry brakes down to axis-symmetry around the axis of rotation. The same affect is also observed for the components of the spatial metric tensor γ_{ij}. This means that although for the case of the polar angle we can continue using the Euclidean approach, for the case of the azimuthal angle we need to use the general case of an angle between two vectors u and w in a curved space given by:

$$\theta = cos^{-1}(\frac{\gamma(u,w)}{|u||w|}) \tag{5.12}$$

where $\gamma(u,w) = \gamma_{ij}u^i w^j$ and $|u| = \sqrt{\gamma(u,u)} = \sqrt{\gamma_{ij}u^i u^j}$. For our calculation we used as u the unit vector $\hat{r}$ of the vector $\bar{r}$ corresponding to the arbitrary point under study and as w we used the unit vector $\bar{k}$. Applying the quadrupole formula for the case of the $l = 2, m = 2$ mode of oscillation of the BU1 model we get the value $\tau_{Co} = 0.4073735$ seconds in the co-moving frame. The equivalent value for the BU1 models when the study is done in full general relativity is $\tau_{Co} = 1.31823$ seconds. The corresponding values for the BU2 case are $\tau_{Co} = 2.37583$ seconds for the Cowling case and $\tau_{Co} = 3.9545$ seconds for the full general relativistic case. These results show that moving from the Cowling approximation to full general relativity we get an increase in the damping times of the f-modes of oscillation by around two to three times. This result in combination with the fact that the f-modes appear in lower frequencies in the full general relativistic cases is a rather exciting finding. It shows that not only the CFS instability is expected to appear earlier in a row of models of ever increasing angular velocity but also that the mode of oscillation responsible for

the resulting radiation will be easier to identify through our gravitational wave detectors. These results, although exciting, should be taken with a grain of salt. The concern comes mainly from what we can observe in figure (5.8) which is a lack of smoothness visible in the eigenfunction corresponding to the co-moving frame. As mentioned before our code extracts all the time series from the perspective of the inertial frame. This means that to get the appropriate time series from the perspective of the co-moving fame, we need for every iteration t_i to interpolate all the hydrodynamical quantities of interest and then shift them by an angle $\phi = \Omega t_i$ back to their original position in the Cartesian grid. Depending on the interpolation method used, this procedure is bound to produce numerical inaccuracies. Our experience with the implementation of the quadrupole formula applied for the case of 3D-Cartesian grid says that it is rather sensitive to these kind of inaccuracies. Another issue that should raise concern in this case is weather the azimuthal angle θ is correctly calculated. For our case we use as the value γ_{ij} at the center of the star which in reality gives the Euclidean θ. Maybe a better approach would be to use the proper distances in (5.10) and (5.11) instead of the Euclidean ones.

Unfortunately this result came very late in our research. This means that the study of the f-mode damping times for the fastest rotating neutron stars of the BU-series that would eventually lead to the desired gravitational wave asteroseismology relations will have to wait for a future extension of this project. Same obviously is true for the damping times of the rest of the observed modes. For the time being we will limit ourselves to the frequencies of the f- and p-modes observed. These results are presented in tables (5.1) and (5.2). The same results are also presented in figure (5.10), where we have plotted the frequencies observed for every model as a function of the corresponding $T/|W|$ value for this specific model. In this case T refers to the rotational energy and W to gravitational binding energy of the model under study.

Table 5.1: Frequencies of the $l = |m| = 2$ non radial non axisymmetric f - modes of oscillation of the BU models.

Model - Approximation	${}^2f_2$ (Hz)	${}^2f_{-2}$ (Hz)
BU0 - Cowling	1893.71	1893.71
BU0 - Full GR	1589.7	1589.7
BU1 - Cowling	1352.41	2299.1
BU1 - Full GR	1048.34	1691.41
BU2 - Cowling	1082.4	2367.75
BU2 - Full GR	777.897	2069.88
BU3 - Cowling	811.586	2434.76
BU3 - Full GR	575.041	2131.03
BU4 - Cowling	743.979	2434.84
BU4 - Full GR	371.99	2164.3
BU5 - Cowling	432.734	2488.22
BU5 - Full GR	202.935	2178.17
BU6 - Cowling	270.571	2435.14
BU6 - Full GR	67.6429	2198.39
BU7 - Cowling	196.089	2434.21
BU7 - Full GR	-142.913	2181.83

Table 5.2: Frequencies of the $l = |m| = 2$ non radial non axisymmetric p - modes of oscillation of the BU models.

Model - Approximation	${}^2p_2$ (Hz)	${}^2p_{-2}$ (Hz)
BU0 - Cowling	4118.81	4118.81
BU0 - Full GR	3686.76	3686.76
BU1 - Cowling	3245.79	4530.59
BU1 - Full GR	2877.86	4159.54
BU2 - Cowling	2821.01	4654.32
BU2 - Full GR	2445.3	4261.52
BU3 - Cowling	2441.52	4666.62
BU3 - Full GR	2100.59	4295.89
BU4 - Cowling	2279.28	4666.78
BU4 - Full GR	1788.93	4294.79
BU5 - Cowling	1812.07	4577.51
BU5 - Full GR	1522.01	4261.63
BU6 - Cowling	1535.49	4464.43
BU6 - Full GR	1285.21	4207.39
BU7 - Cowling	1386.14	4415.38
BU7 - Full GR	1166.75	4171.14

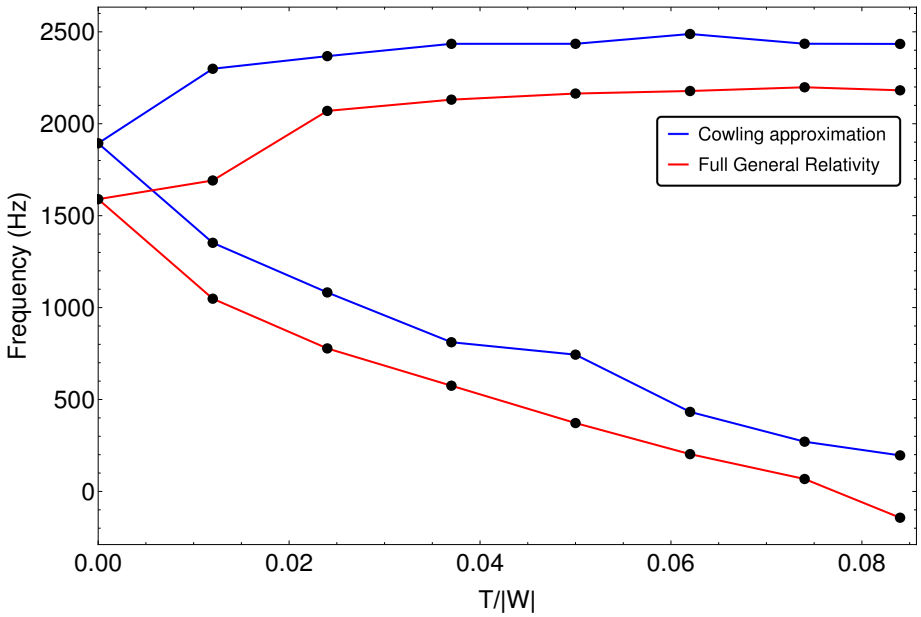

(a) f-mode frequencies.

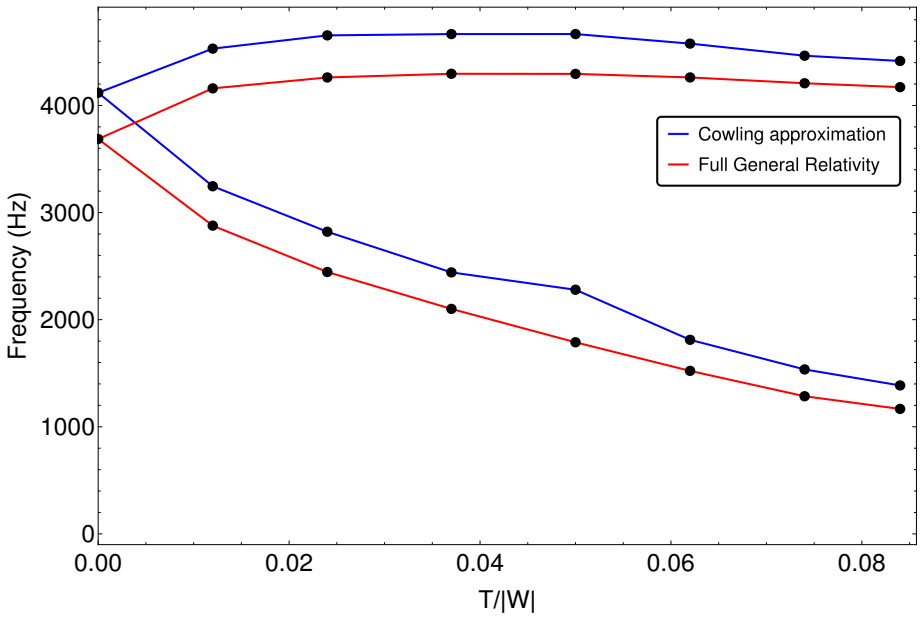

(b) p-mode frequencies.

Figure 5.10: Frequencies of $l = |m| = 2$ f- and p-modes for the models of the BU sequence.

5.3 Study of the CFS instability for super-massive neutron stars

There exist astrophysical scenarios such that could lead to the creation of rapidly rotating super-massive neutron stars, a term which refers to neutron stars the baryon mass

of which is higher than two solar masses. Such a configuration could be the result of the merger of a binary neutron star system. A neutron star with such high mass can not exist for non rotating cases simply because the gravitational force would overcome the counter balancing force from the degenerate neutrons. Rapid rotation though results in the appearance of centrifugal forces which also work against gravity and thus allow for higher masses. What is very interesting about these models is that the existence of such high rotational frequencies guaranties the appearance of the CFS instability. Thus such models are considered to be really serious candidates for gravitational waves sources. For the time being we have studied two such high mass configurations, the characteristics of which can be seen in the table bellow.

Table 5.3: Equilibrium properties of the super massive models as described by a polytropic EOS $p = K\rho_0^{\Gamma}$ where $\Gamma = 3.444$, $K = 400000$. The entries in the table are ρ_c the central rest mass density in units $c = G = M_0 = 1$, M the gravitational rest mass, r_e the equatorial radius in solar masses, r_p/r_e the ratio of the equatorial to the polar radius, v_{rot} the rotational frequency in Hertz.

Models	$\rho_c \times 10^3$	$M(M_\odot)$	$r_e(M_\odot)$	r_p/r_e	$v_{rot}(Hz)$
SMM1	2.6842	2.559498	7.94976	0.728036	1685.15
SMM2	2.3807	2.566838	8.362617	0.700129	1624.35

We studied these models both under the Cowling approximation and in full General Relativity. The results for the $l = |m| = 2$ f-modes can be seen in table 5.4. As we can see, in every case the frequencies of the counter rotating of the f-mode appear to be negative, which signifies that indeed such models should be considered as possibly serious sources of gravitational radiation.

Table 5.4: Frequencies of the $l = |m| = 2$ non radial non axisymmetric f - modes of oscillation of the super massive models introduced in table 5.3.

Model - Approximation	${}^2f_2$ (Hz)	${}^2f_{-2}$ (Hz)
SMM1 - Cowling	-800	4599
SMM1 - Full GR	-1171	4396
SMM2 - Cowling	-747	4394
SMM2 - Full GR	-1065	4093

5.4 Gravitational wave signal from oscillating neutron stars

As we mentioned in section 5.1.3, one rather interesting and also instructive way to study the characteristics of an oscillating neutron star is through the study of the gravitational waveforms extracted by the corresponding simulations, represented by the $\Psi_4 = \ddot{h}_+ - i\ddot{h}_\times$ quantity. This quantity contains information not only for the fluid modes of oscillation of the models under study but also for the so called space-time w-modes that appear in such systems.

To get an insight on the behaviour of Ψ_4 for the case of an oscillating neutron star it would be helpful to follow the logic of [15] and briefly study the characteristics of the toy model depicted in figure (5.11). This toy model consists of two strings, one finite with

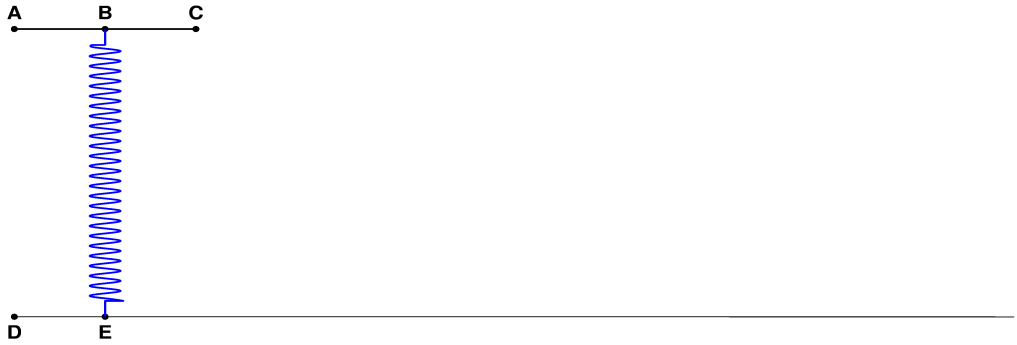

Figure 5.11: A coupled system that consists of a finite string of length $2l$ and a semi-infinite string, coupled by a spring with spring constant k.

fastened ends which plays the role of the source of oscillation (just like a localized neutron star) and one semi-infinite string which will get perturbed by the oscillations of the first string (just like the space-time outside of a neutron star) and finally a massless spring of spring constant k which couples the two mediums to each other. Considering the case of an outgoing wave condition on the semi-infinite string, with $\omega = \sigma + i/\tau$ being the complex frequency of the vibration and c the wave speed, the eigenfrequency equation of this system

turns out to be:

$$z(e^{-z} + e^{z}) = K(e^{-z} - e^{z})(2 + e^{-2z}) \tag{5.13}$$

where $K = kl/(2T)$ with T being the tension of the strings. Solving this equation for small K gives two different normal modes, ones with weak damping and ones with strong damping.

In the weak damping case the vibration of the system is mainly concentrated in the finite string while the semi-finite string vibrates with a small amplitude motion. This behaviour resembles the behaviour of Ψ_4 due to the existence of the fluid modes inside the star. On the other hand the vibrational pattern of the strongly damped normal modes is completely different. The energy of the vibration of these modes is mainly concentrated in the semi-infinite string and is carried away very rapidly. This modes serve to damp out any initial excitation of the star and would not exist if the two strings were not coupled. This behaviour resembles that of Ψ_4 due to the existence of the space-time w-modes of oscillation.

5.4.1 Fluid modes of oscillation

Although we already saw an example of the affect of the fluid modes inside a neutron star on the surrounding space-time for the case of the non-rotating $BU0$ model in figure 5.5, it is interesting to also study the Ψ_4 quantity for the case of a rotating neutron star. An example like this can be seen in figure 5.12 for the case of the rotating $BU2$ model.

What becomes immediately apparent is that although all the frequencies observed during the study of the hydrodynamical quantities of the $BU2$ model are also present in the gravitational wave signal, the amplitude of oscillation of the non radial non axisymmetric modes characterized by a negative m is at least an order of magnitude smaller than that of the modes characterized by a positive m. This is true independent of whether we study the $l = 2, m = -2$ or the $l = 2, m = 2$ decomposition of the Ψ_4 signal. Nevertheless though, the information of all the non radial non axisymmetric fluid modes is still present in the gravitational wave signal.

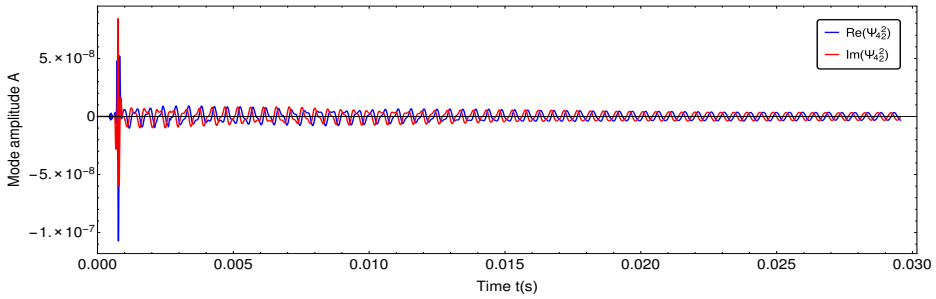

(a) Gravitational wave signal, $l = 2, m = 2$ decomposition.

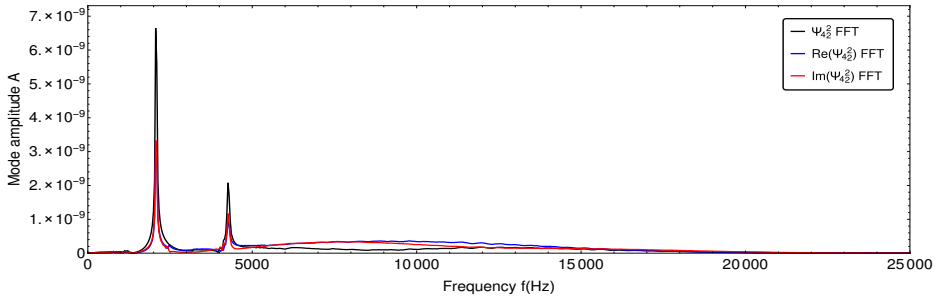

(b) Corresponding fast Fourier transform.

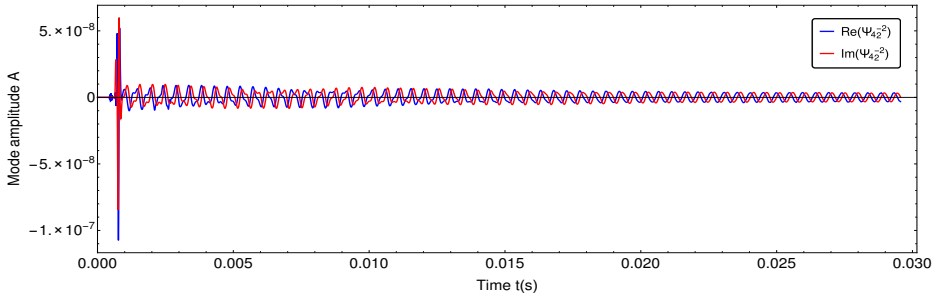

(c) Gravitational wave signal, $l = 2, m = -2$ decomposition.

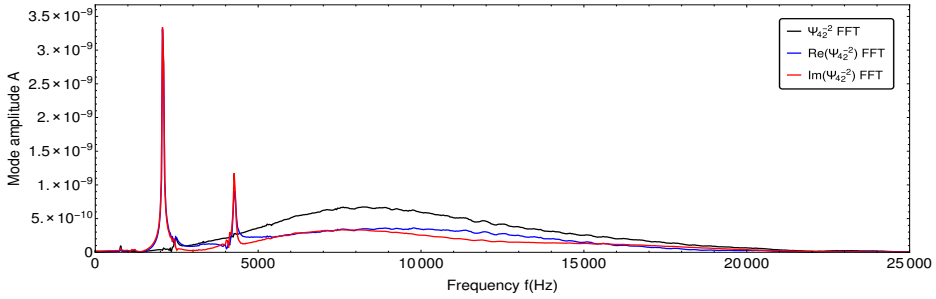

(d) Corresponding fast Fourier transform.

Figure 5.12: Decomposition into the $l = 2, |m| = 2$ spin-weighted spherical harmonics with spin weight $s = 2$ of the Ψ_4 quantity extracted from a distance of roughly 130 $M_\odot$ from the center of the star. The star under study is the $BU2$ model. The evolution took place in full general relativity with an $l = 2$, $m = 2$ non axisymmetric non radial initial perturbation on the rest mass density.

5.4.2 Space-time modes of oscillation

We can now turn our attention to the part of Ψ_4 decomposition which, at least amplitude wise, seem to dominate gravitational wave signal. Figure 5.13 shows again the spin weighted $l = 2, m = 2$ decomposition of the Ψ_4 of the $BU2$ but this time we have also included the analysis of the same signal without the oscillation due to the space-time w-mode. As we can see in the corresponding FFTs, this large amplitude oscillation is characterized by a frequency of around 8000 to 12000 Hz. Figure 5.14 presents a close up of this mode of oscillation.

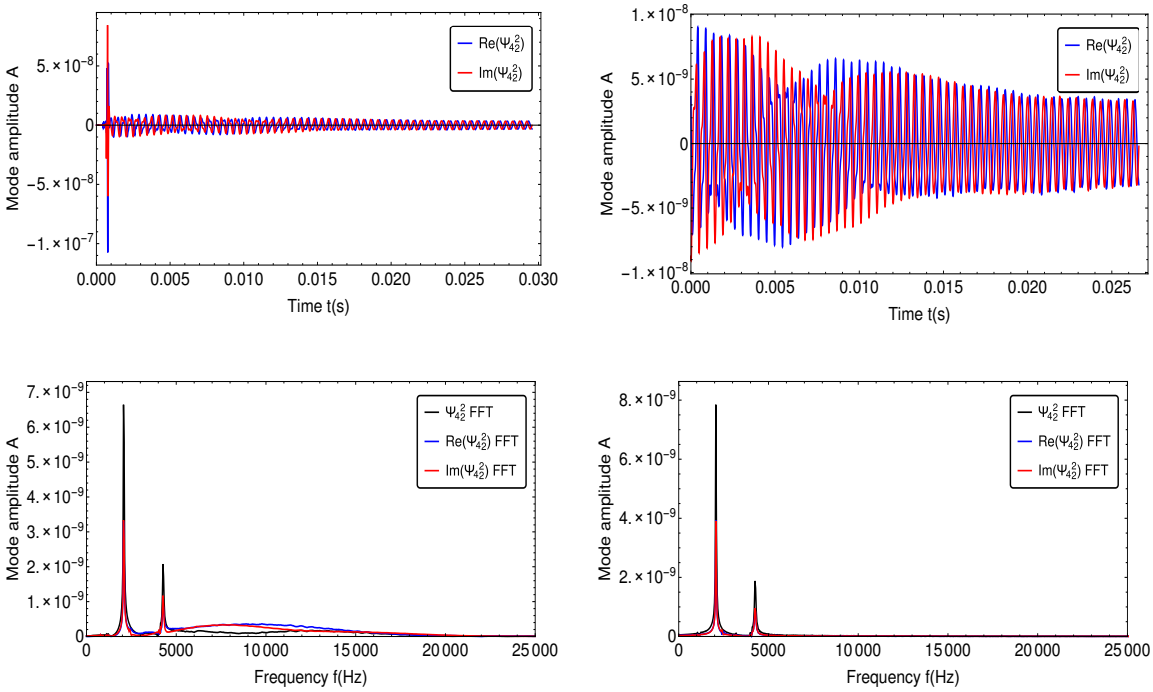

Figure 5.13: Decomposition into the $l = 2, m = 2$ spin-weighted spherical harmonics with spin weight $s = 2$ of the Ψ_4 quantity extracted from a distance of roughly 130 $M_\odot$ from the center of the star. The star under study is the $BU2$ model.

What is interesting about figure 5.14 is that we can see two distinct and independent oscillatory patterns instead of just a dominant one. The one on the right is definitely a space-time w-mode while the one on the left could be a different type of w-mode or simply what we call junk radiation. We will discuss this issue later.

As part of this project we extracted the gravitational wave signal for all the models of

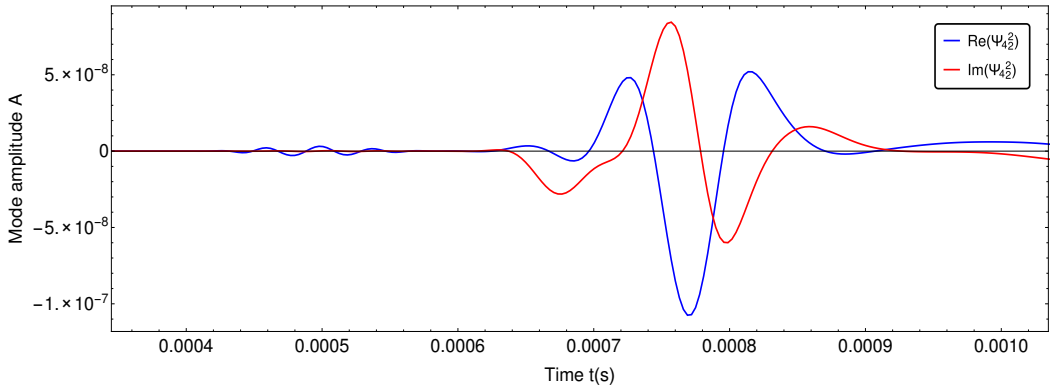

Figure 5.14: W-mode oscillation observed in the $l = 2, m = 2$ decomposition of Ψ_4. The star under study is the $BU2$ model.

the BU sequence and studied the frequencies and damping times of the w-modes present in the $l = |m| = 2$ decomposition of the Ψ_4 quantity. The frequencies were calculated in post processing through the corresponding FFTs while the damping times were calculated straight for the gravitational wave signal. More specifically regarding the damping times we located the maximum values of the quantity $ln(|\Psi_4|)$ and fitted a straight line through them. This approach is correct under the assumption that the oscillatory pattern under study is characterized by a single frequency and a single damping time. The results of this analysis can be seen in tables 5.5 and 5.6.

Table 5.5: Frequencies and damping times of the w-mode observed in the real and imaginary parts of the $l = 2$, $m = 2$ decomposition of Ψ_4 extracted for the models of the BU sequence.

	$\ddot{h}_+$	$\ddot{h}_\times$
Model	f (Hz) - τ (ms)	f (Hz) - τ (ms)
BU0	10268 - 0.0314139	-
BU1	10095 - 0.0413859	7813 - 0.0413859
BU2	9783 - 0.0273556	7605 - 0.0605838
BU3	8608 - 0.022839	7398 - 0.0630374
BU4	7606 - 0.0657457	7675 - 0.0648122
BU5	7329 - 0.072675	7191 - 0.0666559
BU6	6470 - 0.083195	6984 - 0.0689653
BU7	6181 - 0.0888185	6666 - 0.0696052

As a last part for this project we studied the relation between the type and amplitude

Table 5.6: Frequencies and damping times of the w-mode observed in the real and imaginary parts of the $l = 2$, $m = -2$ decomposition of Ψ_4 extracted for the models of the BU sequence.

	$\ddot{h}_+$	$\ddot{h}_\times$
Model	f (Hz) - τ (ms)	f (Hz) - τ (ms)
BU0	10268 - 0.0302892	-
BU1	10095 - 0.0413859	7813 - 0.0413859
BU2	9783 - 0.0273556	7605 - 0.0605838
BU3	8608 - 0.022839	7398 - 0.063037
BU4	7710 - 0.0657457	7053 - 0.0648122
BU5	7329 - 0.072675	7191 - 0.0666559
BU6	6499 - 0.083195	6983 - 0.0689653
BU7	6181 - 0.0888185	6666 - 0.0696052

of the initial perturbation that we impose on the rest mass density of our models and the resulting wave-forms. For all the simulations discussed up to this point the amplitude of the initial perturbation was equal to 10^{-3} the rest mass density at the center of the equilibrium model under study. For the purpose of this project we studied the equilibrium non rotating $BU0$ model and the moderately rotating $BU4$ model for two different types of initial perturbations, an $l = 2, m = 0$ non radial axisymmetric and an $l = 2, m = 2$ non radial non axisymmetric, and three different values for the corresponding perturbation amplitude, 10^{-2}, 10^{-3} and 10^{-4} times the central rest mass density. Finally for every case we extracted only the Ψ_4 decomposition corresponding to the initial perturbation. So for a non radial axismymetric initial perturbation we studied the $l = 2, m = 0$ Ψ_4 decomposition while for the non radial non axisymmetric cases we studied the $l = 2, m = \pm 2$ Ψ_4 decomposition. Figure 5.15 shows an example of how increasing the amplitude of the initial non radial axisymmetric perturbation on the non rotating $BU0$ model affects the corresponding $l = 2, m = 0$ Ψ_4 decomposition.

What becomes immediately apparent for all the cases that we studied is that changing the initial amplitude of the perturbation, at least within such limits that it is a small perturbation and not a strong disruption that could potentially tear apart the star, does not change the frequency or the damping time of the w-mode. What does change though is the am-

plitude of the oscillation corresponding to the w-mode of interest. Worthy of mentioning is also the fact that the same exact behaviour is observed for the small oscillatory pattern observed prior to the w-mode under study. Although this is not proof enough that this is a different type of a space-time w-mode we can't at this point simply discard it as junk radiation.

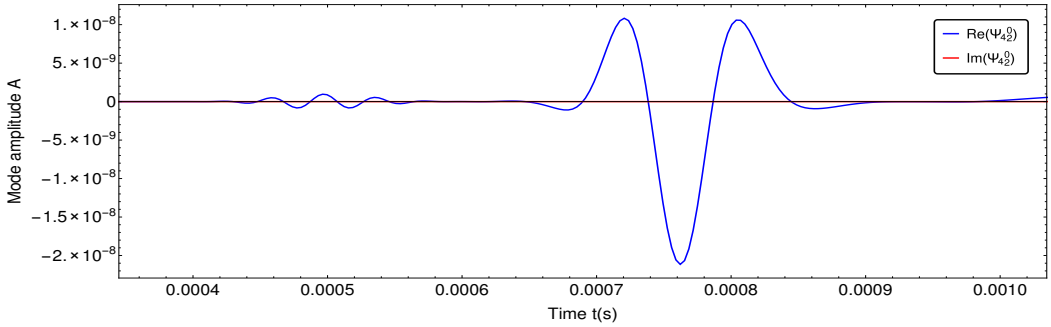

(a) Perturbation amplitude: $A = 10^{-4}\rho_c$.

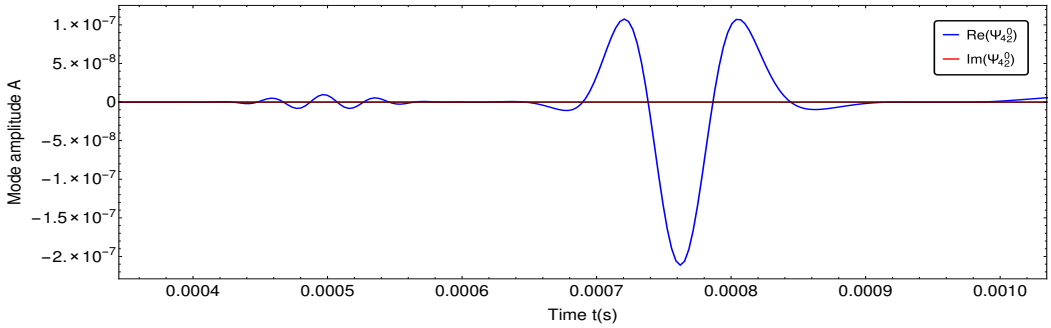

(b) Perturbation amplitude: $A = 10^{-3}\rho_c$.

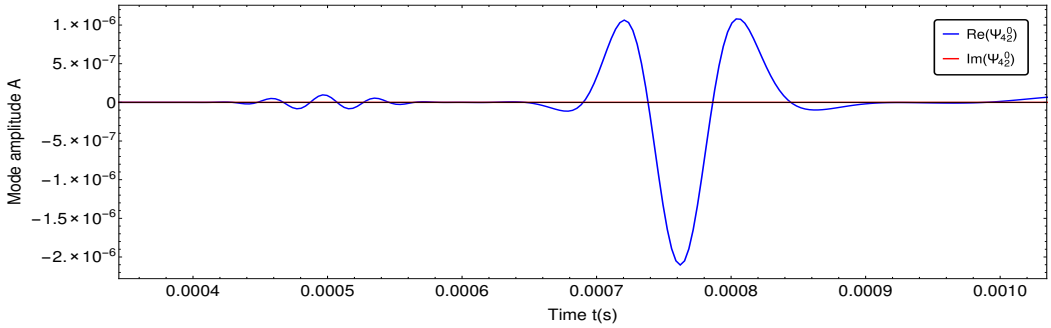

(c) Perturbation amplitude: $A = 10^{-2}\rho_c$.

Figure 5.15: Decomposition into the $l = 2, m = 0$ spin-weighted spherical harmonics with spin weight $s = 2$ of the Ψ_4 quantity extracted from a distance of roughly 130 $M_\odot$ from the center of the star. The star under study is the $BU0$ model.

5.5 Future work

Regarding future work the steps that need to be taken are pretty straight forward at this point. First of all we need to complete the task of calculating the damping times for the counter and co-rotating f- and p-modes originating from the non axisymmetric perturbations on the models presented above. This task would require to take care of all the issues regarding the quadropole formula and its implementation on a three-dimensional Cartesian grid and then move on to reproduce accurately all the existing results in the literature regarding sequences of polytropic neutron star models. Up to now similar studies have been done only in the Cowling approximation using two-dimensional codes as can be seen in [5,6]. After this task is complete then we need to extend the quadropole formula to include the contribution of the space-time perturbations, move on to study the same polytropic models in full general relativity and finally create the desired empirical equations that will allow us to do asteroseismology on rotating neutron stars.

From this point on, given that our ultimate goal is to study models that are as close to actual neutron stars as possible, we would need to extend the above projects to include more realistic aspects of neutron star physics. This would require to leave behind the polytropic equations of state and move on to more realistic equations of state that take in account the micro-physics inside the neutron stars. Finally we need to also include in our models the existence of strong magnetic fields present in real neutron stars.

Appendices

APPENDIX A

GEOMETRICAL UNITS OF MEASUREMENT

Within the field of Numerical General Relativity it is common to use the so called geometrical units of measurement. This approach enables us to express both space and time intervals in terms of a mass scale, most commonly the Solar Mass $M_{\odot}$. The logic behind this choice has to do with the fundamental concept that space and time are not two separate entities just like in Classical Mechanics, but a common entity that we call space-time and the geometrical characteristics of which are decided by the mass distribution inside it. Under this approach it makes sense that instead of measuring space distances with units different from the ones that we use to measure time distances, we use the same units to measure any kind of distance inside the space-time structure. Following the same logic, given the coupling of mass with space-time, it makes sense to use the same units to measure masses and distances in space-time. Setting $G = c = 1$ we get:

$$\begin{cases} G = 6.67384 \times 10^{-8} cm^3 \cdot g^{-1} \cdot s^{-2} = 1 \\ c = 2.99792458 \times 10^{11} cm \cdot s^{-1} = 1 \\ M_{\odot} = 1.9891 \times 10^{33} g \end{cases} \Rightarrow \begin{cases} 1M_{\odot} = 4.92686 \times 10^{-6} s \\ 1M_{\odot} = 1.47704 \times 10^{3} m \end{cases} \tag{A.1}$$

Using geometrical units in a General Relativistic numerical code is very convenient. In this context to convert the basic hydrodynamical quantities from geometrical units to cgs units we use the following conversion factors:

$$\begin{aligned} C_{pressure} &= \frac{c^8}{G^3 \cdot M_{\odot}^2} \\ C_{density} &= \frac{c^6}{G^3 \cdot M_{\odot}^2} \end{aligned} \tag{A.2}$$

BIBLIOGRAPHY

[1] Abbott, B. P., Abbott, R., Abbott, T. D., Abernathy, M. R., Acernese, F., Ackley, K., Adams, C., Adams, T., Addesso, P., Adhikari, R. X., and et al., Observation of Gravitational Waves from a Binary Black Hole Merger, Physical Review Letters, vol. 116, no. 6, p. 061102, 2016.

[2] Eugene Balbinski, Steven Detweiler, Lee Lindblom, Bernard F. Schutz, The accuracy of the quadrupole approximation for the gravitational radiation from pulsating stars, Mon. Not. R. astr. Soc. (1985 213, 553 - 561)

[3] James R. Ipser, Lee Lindblom, The oscillations of rapidly rotating Newtonian stellar models, The Astrophysical Journal, 355:226-240, 1990 May 20

[4] James R. Ipser, Lee Lindblom, The oscillations of rapidly rotating Newtonian stellar models II. Dissipative effects, The Astrophysical Journal, 373:213-221, 1992 May 20

[5] Erich Gaertig, Kostas D. Kokkotas, Gravitational wave asteroseismology with fast rotating neutron stars, Physical Review D 83, 064031 (2011)

[6] Daniela D. Doneva, Erich Gaertig, Kostas D. Kokkotas, Christian Kruger, Gravitational wave asteroseismology of fast rotating neutron stars with realistic equations of state, Physical Review D 88, 044052 (2013)

[7] C. Aerts, J. Christensen-Dalsgaard, D.W. Kurtz, Asteroseismology, Springer, (2010)

[8] Jose A. Font, Harald Dimmelmeier, Anshu Guptan, Nikolaos Stergioulas, Axisymmetric modes of rotating relativistic stars in the Cowling approximation, Mon. Not. R. Astron. Soc. 325, 1463-1470 (2001)

[9] Harald Dimmelmeier, Nikolaos Stergioulas, Jose A.Font, Non-linear axisymmetric pulsations of rotating relativistic stars in the conformal flatness approximation, Mon. Not. R. Astron. Soc. 368, 1609-1630 (2006)

[10] Eric Gaertig, Kostas D. Kokkotas, Oscillations of rapidly rotating relativistic stars, Physical review D 78, 064063 (2008)

[11] Burkhard Zink, Oleg Korobkin, Erik Schnetter, Nikolaos Stergioulas, Frequency band of the Chandrasekhar-Friedman-Schutz instability, Physical review D 81, 084055 (2010)

[12] Frank Loffler, Joshua Faber, Eloisa Bentivegna, Tanja Bode, Peter Diener, Ronald Haas, Ian Hinder, Bruno C. Mundim, Christian D. Ott, Erik Schnetter, Gabrielle Allen, Manuela Campanelli, Pablo Laguna, The Einstein Toolkit: A Community Computational Infrastructure for Relativistic Astrophysics, Class. Quantum Grav., vol. 29, no. 11, p. 115001, 2012

[13] Francesc Banyuls, Jose A. Font, Jose M. Ibanez, Jose M. Marti, Juan A. Miralles, Numerical 3 + 1 General Relativistic Hydrodynamics: A Local Characteristic Approach, The Astrophysical Journal, 476:221-231, 1997 February 10

[14] Nikolaos Stergioulas, John L. Friedman, Comparing models of rapidly rotating relativistic stars constructed by two numerical methods, The Astrophysical Journal, 444:306-311, 1995 May 1

[15] Kostas D. Kokkotas, Bernard F. Schutz, Normal Modes of a Model Radiating System, General Relativity and Gravitation, Vol. 18, No. 9, 1986

[16] Kostas D. Kokkotas, B. F. Schutz, W-modes: a new family of normal modes of pulsating relativistic stars, Mon. Not. R. astr. Soc. (1992) 255, 119-128

[17] Gabrielle Allen, Nils Andersson, Kostas D. Kokkotas, Bernard F. Schutz, Gravitational waves from pulsating stars: Evolving the perturbation equations for a relativistic stars, Physical review D, Volume 58, 124012

[18] N. Stergioulas, Living Rev. Relativity 6, 3 (2003), https://ww.livingreviews.org/lrr-2003-3

[19] Nils Anderson, Gravitational waves from instabilities in relativistic stars, Classical and Quantum Gravity, vol. 290 no. 7, 2003

[20] Kostas D. Kokkotas, Gravitational Wave Physics, Article for the Encyclopedia of Physical Science and Technology, 3rd Edition, Volume 7 Academic Press (2002)

[21] T.Baumgarte and S. Shapiro, Numerical Relativity: Solving Einstein's Equations on the Computer, Cambridge University Press, 2010

[22] GW170817 B.P. Abbott et al. Observation observation of Gravitational Waves from a Binary Neutron Star Inspiral, Phys. Rev. Lett. 119, 161101

[23] https://numrel.org/astavropoulos3/projects/

VITA

Stavropoulos Athanasios was born in Thessaloniki, Greece on May 1st, 1986. He received an undergraduate physics degree in 2009 and a masters degree in computational physics in 2011 from the Aristotle University of Thessaloniki. In 2012 he moved to Atlanta where to attend the physics graduate program at the Georgia Institute of Technology. After a year of master studies he started working towards a PhD partly as a member of the Computational Astrophysics group in the Center for Relativistic Astrophysics at Georgia Tech, under the supervision of Professor Pablo Laguna and partly as a member of the Theoretical Astrophysics Group of Tuebingen University in Germany, under the supervision of Professor Kokkotas Kostantinos.